JETP Letters, Vol. 75, No. 6, 2002, pp. 253–256. Translated from Pis'ma v Zhurnal Éksperimental'noĭ i Teoreticheskoĭ Fiziki, Vol. 75, No. 6, 2002, pp. 301–305.

Relationship between the Spectral Densities of Einstein Coefficients for Absorption and Stimulated Emission: Physical Consequences

A. M. Shalagin

Institute of Automatics and Electrometry, Siberian Division, Russian Academy of Sciences, Universitetskiĭ pr. 1, Novosibirsk, 630090 Russia

e-mail: shalagin@iae.nsk.su

Received January 28, 2002

Abstract—The spectral densities of Einstein coefficients for absorption and stimulated emission in a two-level quantum system are not equal to each other beyond the absorption (emission) line if the homogeneous broadening caused by interaction with a thermostat is much larger than the natural width. In this study, a relationship between these coefficients is derived on the basis of general thermodynamic requirements. This relationship is associated with new effects such as population inversion upon the nonresonant absorption of continuous radiation and radiation amplification without population inversion. © *2002 MAIK "Nauka/Interperiodica".*

PACS numbers: 42.50.Ct

The presently available sources of laser radiation are so intense that they can induce nonlinear processes in quantum systems under nonresonant conditions. If the quantum system is a gas of particles colliding with each other and with the particles of a buffer gas, the nonlinear processes are usually described by the familiar quantum master equations (see, e.g., [1–4]). One of the consequences of this description is the popular notion that the cw laser radiation equalizes the level populations for a two-level quantum system as the radiation intensity increases. This notion, customary for researchers specialized in laser physics, ceases to be valid under nonresonant conditions and frequent collisions [5]. Following [5], we will discuss this statement for a two-level atom in a buffer gas. Then, this statement will be generalized to an arbitrary two-level quantum system in a thermostat.

Let us consider a simple model of a two-level atom with the ground state n and excited state m. The gas of these atoms interacts with radiation and particles of a buffer gas. We suppose that collisions themselves do not induce transitions between levels. For a large impact line broadening (compared to the natural and Doppler broadenings), the balance equation for the population of level m has the simple form

$$\frac{dN_m}{dt} + A_{mn}N_m = I[b_{nm}(\Omega)N_n - b_{mn}(\Omega)N_m], \quad \Omega \equiv \omega - \omega_{mn}, \quad N_n + N_m = N, \tag{1}$$

where N_n and N_m are the populations of the corresponding levels, N is the concentration of absorbing particles, A_{mn} is the radiative relaxation constant of level m (the first Einstein coefficient for the m–n transition), I and ω are the radiation intensity and frequency, respectively, ω_{mn} is the transition frequency, and $b_{nm}(\Omega)$ and $b_{mn}(\Omega)$ are the spectral densities of Einstein coefficients B_{nm} and B_{mn} for absorption and stimulated emission, respectively. Therefore, by definition,

$$B_{nm} = \int b_{nm}(\omega)d\omega, \quad B_{mn} = \int b_{mn}(\omega)d\omega. \tag{2}$$

The quantities $Ib_{nm}(\Omega)$ and $Ib_{mn}(\Omega)$ entering Eq. (1) are the numbers of photon absorption and stimulated emission events per unit time, respectively. In the theory based on the familiar master equations [1–4], the following relationship holds:

$$Ib_{nm}(\Omega) = Ib_{mn}(\Omega) = \frac{2|G|^2\Gamma}{\Gamma^2 + \Omega^2}, \quad G \equiv \frac{Ed_{mn}}{2\hbar}, \tag{3}$$

where Γ is the impact halfwidth of the absorption line, E is the radiation electric-field amplitude, d_{mn} is the transition dipole moment matrix element, and G is the Rabi frequency. If Eq. (3) is valid, the population difference $N_n - N_m$ is factored on the right-hand side of Eq. (1). In this case, an increase in the radiation intensity equalizes the populations for any Ω value.

The quantum master equations mentioned above were derived under the assumption that radiative processes occur when atoms move freely and are negligible when atoms collide with each other. The situation cardinally changes for large impact broadening ($\Gamma \gg A_{mn}$) and for $|\Omega| \gg \Gamma$. It was shown in [6, 7] that the radiative pro-

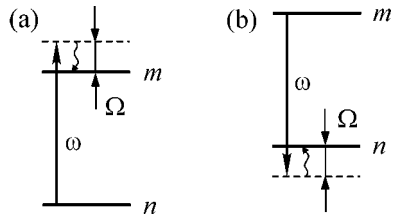

The scheme of transitions in optical collisions: (a) transition with the absorption of a radiation quantum and (b) transition with the stimulated emission of a quantum.

cesses under these conditions primarily occur during collisions (so-called optical collisions). The optical transition at an even farther (quasi-static) wing of the absorption line takes a small fraction of the collision duration (see, e.g., [6, 8]). This circumstance leads to substantial physical sequences.

Both in the framework of the standard quantum master equations [1–4] and in the theory of optical collisions [6, 7], it was demonstrated that the phase-breaking collisions localize a particle in an energy level. In this respect, they are not completely elastic (for more detail, see [6]). Let us consider the case where $|\Omega| \gg \Gamma \gg A_{mn}$. Since the photon absorption and stimulated emission take place during a short-term (relative to the free path time) collision of an absorbing atom with a buffer particle, the energy conservation law in the common formulation—the energy before interaction is equal to the energy after interaction—can be applied to the corresponding process (optical collisions according to [6]). Let an atom originally be in the lower level n and transfer to the level m as a result of a collision accompanied by the absorption of a photon with the energy $\hbar\omega$ (Fig. 1a). When $\Omega > 0$ (this case is presented in Fig. 1a), there is an energy excess $\hbar\Omega$, which is obviously spent to increase the kinetic energy of outgoing particles. In stimulated emission (Fig. 1b), an atom is originally in the level m and, after the collision accompanied by emission of a photon with the energy $\hbar\Omega$, undergoes a transition to level n. When $\Omega > 0$, this process requires extra energy $\hbar\Omega$, which can only be taken from the kinetic energy of particles before collision. For this reason, only particles with sufficiently high kinetic energy can be involved in this process. Therefore, the absorption is more probable than the stimulated emission if $\Omega > 0$. Moreover, general thermodynamic requirements imply that, if the transition from one state (m) to another (n) requires a certain thermostat energy ($\hbar\Omega$), the frequency of $m \longrightarrow n$ transitions is lower than the frequency of reverse $n \longrightarrow m$ transitions by the Boltzmann factor $\exp[-\hbar\Omega/k_{\rm B}T]$, independently of the specific interaction mechanism in a collision (k_B is the Boltzmann constant and T is temperature). This leads to the relationship

$$b_{nm}(\Omega) = b_{mn}(\Omega)\exp[\hbar\Omega/k_{\rm B}T], \qquad (4)$$

which is valid for any sign of Ω. Substitution of Eq. (4) into Eq. (1) results in the equation

$$\frac{dN_m}{dt} + A_{mn}N_m = Ib_{nm}(\Omega)\left[N_n - N_m\exp\left(-\frac{\hbar\Omega}{k_{\rm B}T}\right)\right]. \qquad (5)$$

Relationship (4) and Eq. (5) indicate that the absorption is not equivalent to the stimulated emission. This nonequivalence is due to the statistical properties of the thermostat. The nonequivalence of absorption and emission has been established for quite some time for the quasi-static wing of a spectral line [9]. Moreover, Eq. (4) follows from the results obtained in [9]. Zemtsov and Starostin [10] (see also [11]) obtained the spectral density of absorption coefficient in the form coinciding with the right-hand side of Eq. (5) (up to a factor that is immaterial for the problem in question). However, certain effective (auxiliary) populations were used in [10, 11] instead of N_n and N_m and the derivation of the corresponding relationship was rather complicated. Below, an exceedingly simple derivation of Eq. (4) is based on the general thermodynamic requirements and is applicable not only to the particles of a gas but also to any two-level quantum system interacting with an arbitrary thermostat. From particular examples (the one discussed above and that analyzed in [9]) and from the general derivation below, it follows that the quantities N_n and N_m appearing in Eq. (5) are true, and not effective, populations.

We consider radiation with a broad spectrum (effective width $\Delta\omega$). If $|G|^2 \ll (\Delta\omega)^2 + \Gamma^2 + \Omega^2$, variation in the population of level m is described by the equation

$$dN_m/dt + A_{mn}N_m = \int u(\omega)[b_{nm}(\omega-\omega_{mn})N_n - b_{mn}(\omega-\omega_{mn})N_m]d\omega, \qquad (6)$$

instead of Eq. (1). Here, $u(\omega)$ is the radiation spectral density. For an extremely narrow absorption line, the quantity $u(\omega)$ is factored outside the integral sign in Eq. (6) at the point $\omega = \omega_{mn}$, and one arrives at the following relationship under stationary conditions:

$$A_{mn}N_m = u(\omega_{mn})[B_{nm}N_n - B_{mn}N_m], \qquad (7)$$

which is taken in all manuals (see, e.g., [12]) as a basis for the "Einstein" derivation of both the Planck distribution and the relationship

$$A_{mn} = \frac{\hbar\omega_{mn}^3}{\pi^2c^3}B_{mn}; \quad B_{nm} = B_{mn}, \qquad (8)$$

between the Einstein coefficients A_{mn}, B_{nm}, and B_{mn}. In this study, level degeneracy is ignored. Therefore, the statistical weight of each level is unity. The corresponding generalization is evident and presents no difficulties.

Below, we rely on the physical argumentation used in the standard derivation of Eqs. (8), but we begin with the more general Eq. (6) instead of Eq. (7). In this case, we suppose that the Planck distribution is a well-established fact. In this case, at the thermal equilibrium of medium and radiation, the levels of a quantum system must be populated according to the Boltzmann distribution and the radiation spectrum should correspond to the Planck distribution. In this case, Eq. (6) provides the relationship

$$A_{mn} = \int \frac{\hbar\omega^3}{\pi^2 c^3} b_{mn}(\Omega)\left[\frac{b_{nm}(\Omega)}{b_{mn}(\Omega)}\exp\left(\frac{\hbar\omega_{mn}}{k_B T}\right) - 1\right] \times \left[\exp\left(\frac{\hbar\omega}{k_B T}\right) - 1\right]^{-1} d\omega, \quad (9)$$

which should be satisfied for any transition frequency and any medium temperature. At the same time, the first Einstein coefficient A_{mn} characterizes the m–n transition and must be independent of the thermostat characteristics and its temperature. In order for this condition to be satisfied, the expressions in the square brackets in the integrand must be equal to each other. This requirement leads to relationship (4) between the spectral densities $b_{nm}(\Omega)$ and $b_{mn}(\Omega)$. If this relationship is valid, Eq. (9) reduces to

$$A_{mn} = \int \frac{\hbar\omega^3}{\pi^2 c^3} b_{mn}(\Omega) d\Omega. \quad (10)$$

If the spectral line width of stimulated emission is much less than the frequency of the m–n transition, Eq. (10) evidently reduces to the first of Eqs. (8). As follows from Eqs. (4) and (2), in order for the second of Eqs. (8) to be valid, the effective width of the absorption (emission) line must be much less than the mean thermal energy of the thermostat.

Relationship (4) does not involve the radiation characteristics. The quantities $b_{mn}(\Omega)$ and $b_{nm}(\Omega)$ depend on the characteristics of the quantum system and the thermostat. For this reason, relationship (4) between these quantities is valid not only when the radiation spectrum is thermal but also when the quantum system is exposed to radiation with any spectral composition. This conclusion is supported by the methods of deriving Eq. (4) in particular cases.

Now, we discuss the possible physical consequences of Eq. (5). Under stationary conditions, this equation leads to

$$\frac{N_m}{N_n} = \frac{Ib_{nm}(\Omega)}{A_{mn} + Ib_{nm}(\Omega)\exp[-\hbar\Omega/k_B T]}. \quad (11)$$

If the radiation intensity is so high that

$$Ib_{nm}(\Omega) > \frac{A_{mn}}{1 - \exp[-\hbar\Omega/k_B T]}, \quad (12)$$

it follows from Eq. (11) that $N_m > N_n$; i.e., the populations are inverted. This is a fundamentally new point, which implies the possibility of lasing at the resonance frequency ω_{mn} of the m–n transition. The observation of this phenomenon was reported in [5]. The maximum inversion is reached when $Ib_{nm}(\Omega) \gg A_{mn}\exp[\hbar\Omega/k_B T]$ and is equal to ($\Omega > 0$)

$$N_m/N_n = \exp[\hbar\Omega/k_B T]. \quad (13)$$

Let us estimate the parameters of laser radiation and the gas medium for which condition (12) for population inversion is satisfied. For $\Omega \gg \Gamma$(wing of the absorption line), one has the formula [6]

$$Ib_{nm}(\Omega) = 2|G|^2\Gamma_{oc}/\Omega^2, \quad (14)$$

where Γ_{oc} is the phase relaxation rate in optical collisions [6]. The quantity Γ_{oc}, as well as the impact halfwidth Γ, is proportional to the buffer gas pressure, but can be much larger than Γ since the actual absorption in the line wing can be larger than the value given by Eq. (3). Formula (14) indicates that the quantity $Ib_{nm}(\Omega)$ increases proportionally to the radiation intensity and to the buffer gas pressure. Let us consider the electronic transitions in atoms with a characteristic value $A_{mn} \sim$ 10 MHz and a characteristic broadening of ~20 MHz/torr by the particles of the buffer gas. We take the frequency detuning $\Omega = 50$ cm^{-1} (this value virtually corresponds to the quasi-static wing of absorption line). To obtain the upper estimate for radiation intensity, we take the Γ_{oc} value equal to $\Gamma \approx 10^4$ MHz at the atmospheric pressure of buffer gas. Under these conditions, the threshold (12) is reached at $|G| \approx 3$ cm^{-1}, which corresponds to the radiation intensity $I \approx 10$ MW/cm^2. In reality, the threshold intensity must be much lower (by an order of magnitude or more) when it is taken into account that Γ_{oc} exceeds Γ. Nevertheless, the required radiation intensity is still high but easily reached using pulsed lasers. As follows from Eq. (5), in order for the results obtained for cw radiation to be applicable, the condition

$$A_{mn} + Ib_{nm}(\Omega)[1 + \exp(-\hbar\Omega/k_B T)] \gg 1/\Delta t \quad (15)$$

must be satisfied, where Δt is the radiation pulse duration. Many pulsed lasers have a pulse duration $\Delta t \approx$ 5–10 ns, for which Eq. (15) is valid under the above conditions. Thus, the conditions for population inversion can be satisfied with presently available radiation sources.

Another qualitatively new physical effect is lasing without population inversion. If the populations of levels m and n are close to each other for some reason but N_m is still less than N_n, the lasing regime is realized for radiation at the "red" wing of the spectral line (S.A. Babin was the first to point out this possibility). Indeed, the absorption (gain) coefficient α_μ of probe

radiation in the line wing is related to the right-hand side of Eq. (5) as

$$\alpha_\mu = \frac{1}{4\pi}\lambda_\mu^2 \frac{A_{mn}\Gamma_{oc}(\Omega_\mu)}{\Omega_\mu^2} \times [N_n - N_m \exp(-\hbar\Omega_\mu/k_B T)], \quad (16)$$

where the characteristics of probe radiation are labeled by the subscript μ (λ_μ is the wavelength). If populations are equal to each other ($N_n = N_m = N/2$, where N is the total concentration of particles interacting with the field) and the frequency detuning Ω_μ is negative, one has $\alpha_\mu < 0$; i.e., there is lasing without population inversion. For positive detuning, one has $\alpha_\mu > 0$, which is also surprising for equal populations. This effect can be conventionally called extra absorption.

The use of intense laser radiation in resonance with the m–n transition is the most efficient method of equalizing populations. In this case, the effect will be observed by comparing the intensities of the probe radiation passing through a medium in the absence and presence of intense radiation: the probe radiation is absorbed and enhanced in the former and latter cases, respectively. Let α_μ^0 be the absorption coefficient in the absence of strong radiation and all particles be on the lower level n. In this case, the ratio α_μ/α_μ^0 is expressed by the simple formula

$$\frac{\alpha_\mu}{\alpha_\mu^0} = \frac{1}{2}[1 - \exp(-\hbar\Omega_\mu/k_B T)]. \quad (17)$$

As is seen, the gain can be comparable with the maximum possible absorption coefficient for the same frequency detuning. Since the absorption in the spectral line wings is detected quite reliably, lasing without population inversion can also be easily detected, because the intense radiation can make the medium transparent at a sufficiently high concentration of absorbing particles (for atoms, up to 10^{15} cm^{-3} and higher). A similar conclusion is evidently valid for the detection of extra absorption.

We derive relationship (4) from general thermodynamic requirements. For each particular physical case, this relationship can be justified by a specific physical mechanism and the limits of applicability of this relationship can be determined simultaneously. For example, the above consideration demonstrates that optical collisions realize this mechanism for gas particles. Relationship (4) generally applies when dephasing processes caused by interaction with a thermostat in a quantum system are much faster than the radiative relaxation. Since the inequality of the spectral densities of Einstein coefficients is substantial only at the far wings of spectral line, previous solutions to the problems of laser physics, nonlinear optics, and nonlinear spectroscopy should not be revised or refined even if Eq. (4) is valid. These problems always referred to the near-resonance spectral region narrower than $k_B T/\hbar$. However, new effects can arise, as was demonstrated above, in the problems (including nonlinear) concerned with high-frequency detuning values. I hope that the two above-discussed new physical effects associated with Eq. (4) are not the only consequences of this relationship.

I am grateful to S.G. Rautian, E.V. Podivilov, and S.A. Babin for stimulating discussions and to participants of the seminars at the Institute of General Physics, Russian Academy of Sciences, and the Institute of Spectroscopy, Russian Academy of Sciences, for valuable discussions. This work was supported by the Russian Foundation for Basic Research (project no. 01-02-17433), by the Ministry of Industry, Science, and Technology of the Russian Federation (program "Physics of Quantum and Wave Processes"), and by the program "Integration."

REFERENCES

1. R. F. Snider, J. Chem. Phys. **32**, 1051 (1960).
2. V. A. Alekseev, T. L. Andreeva, and I. I. Sobel'man, Zh. Éksp. Teor. Fiz. **62**, 614 (1972) [Sov. Phys. JETP **35**, 325 (1972)].
3. V. S. Letokhov and V. P. Chebotajev, *Nonlinear Laser Spectroscopy* (Springer-Verlag, Berlin, 1977).
4. S. G. Rautian and A. M. Shalagin, *Kinetic Problems of Nonlinear Spectroscopy* (North-Holland, Amsterdam, 1991).
5. R. V. Markov, A. I. Plekhanov, and A. M. Shalagin, Zh. Éksp. Teor. Fiz. **120**, 1185 (2001) [JETP **93**, 1028 (2001)].
6. S. I. Yakovlenko, Usp. Fiz. Nauk **136**, 593 (1982) [Sov. Phys. Usp. **25**, 216 (1982)].
7. D. S. Bakaev, Yu. A. Vdovin, V. M. Ermachenko, and S. I. Yakovlenko, Zh. Éksp. Teor. Fiz. **83**, 1297 (1982) [Sov. Phys. JETP **56**, 743 (1982)].
8. I. I. Sobelman, L. A. Vainshtein, and E. A. Yukov, *Excitation of Atoms and Broadening of Spectral Lines* (Nauka, Moscow, 1979; Springer-Verlag, Berlin, 1981).
9. R. E. M. Hedges, D. L. Drummond, and A. Gallagher, Phys. Rev. A **6**, 1519 (1972).
10. Yu. K. Zemtsov and A. N. Starostin, Zh. Éksp. Teor. Fiz. **103**, 345 (1993) [JETP **76**, 186 (1993)].
11. Yu. K. Zemtsov, A. Yu. Sechin, A. N. Starostin, *et al.*, Zh. Éksp. Teor. Fiz. **114**, 135 (1998) [JETP **87**, 76 (1998)].
12. G. S. Landsberg, *Optics* (Nauka, Moscow, 1976).

Translated by R. Tyapaev

JETP Letters, Vol. 75, No. 6, 2002, pp. 257–258. Translated from Pis'ma v Zhurnal Éksperimental'noĭ i Teoreticheskoĭ Fiziki, Vol. 75, No. 6, 2002, pp. 306–308.

Interaction of Plasma Jets and Droplets in the Cathode Region of a Vacuum Arc

G. A. Mesyats and S. A. Barengol'ts*

Institute of Electrophysics, Ural Division, Russian Academy of Sciences, ul. Komsomol'skaya 34, Yekaterinburg, 620016 Russia

Natural Science Research Center, Institute of General Physics, Russian Academy of Sciences, ul. Vavilova 38, Moscow, 117942 Russia

**e-mail: sb@nsc.gpi.ru*

Received January 28, 2002

Abstract—The interaction of liquid-metal droplets with plasma jets in the cathode region of a vacuum arc is considered in the context of an ecton model. It is shown that heating of a droplet in the cathode spot region can initiate the droplet transition to the plasma state. © *2002 MAIK "Nauka/Interperiodica".*

PACS numbers: 52.40.Hf, 52.80.Mg

In the study [1] of cathode plasma parameters by high-speed laser diagnostics, dense plasma formations were observed at distances of several microns from the cathode surface. The plasma concentration in these bunches was close to the concentration in cathode spots and was as high as 10^{20} cm^{-3}. We suppose that the appearance of plasma formations near the cathode is caused by the interaction of plasma jets and droplets emitted by the cathode spot of a vacuum arc. Let us consider this effect in more detail.

It is known that the cathode spot of a vacuum arc emits plasma jets at a velocity of ~10^6 cm/s and liquid-metal droplets at a velocity of ~10^4 cm/s [2, 3]. The plasma jets are formed due to a high energy concentration in the cathode microvolumes as a result of Joule heating by a high-density current. The high energy concentration leads to explosive cathode destruction accompanied by explosive electron emission. The splashing out of a liquid metal in the form of droplets and jets from the cathode spot is initiated by a reactive force appearing upon the expansion of fast plasma jets. The droplet sizes depend on the arc current. For currents close to the threshold arc current i_{thr} of some materials such as copper, gold, and palladium, the droplet-size distribution has a maximum at 0.1–0.2 μm, and the number of droplets emitted from the cathode per flowing unit charge is equal to ~10^7 C^{-1} [4]. As the current increases, the droplets grow in size; for instance, the droplet size may achieve 10 microns at $i \gg i_{thr}$. Almost 90% of the droplet mass emerges at a velocity of ~10^3–10^4 cm/s at an angle of <20° to the cathode surface [2, 3].

The cathode spot has an intrinsic structure, which is manifested by the formation of individual spot cells with a lifetime of ~10^{-8} s [2]. Because of this, the functioning of the cathode spot is accompanied by the cyclic emission of plasma jets and liquid-metal droplets. In addition, the cathode spot itself is in permanent chaotic motion. Due to a large difference in the expansion velocities of plasma and droplets, a situation may occur where the cathode plasma jet hits a droplet. This phenomenon is reminiscent of a hunter shooting at a flying bird and, therefore, we call it the "hunting effect."

Let us consider a noncharged droplet in a quasi-neutral plasma stream emitted by the cathode spot. The density P_i of energy flux to the droplet from the plasma jet ions in unit time can be written as

$$P_i = \frac{j_i(\bar{E}_i + \bar{U}_i - Z\varphi)}{eZ}, \quad (1)$$

where j_i is the ion current density; Z and $\bar{E}_i$ are, respectively, the ion mean charge and energy; φ is the electron work function; $\bar{U}_i = \sum_i f_i U_i$ is the mean ionization potential; and f_i is the fraction of ions with charge i.

When interacting with a droplet, electrons transfer kinetic energy to it and an energy equal to the electron work function

$$P_c = \frac{j_i(2kT_e + \varphi)}{e}, \quad (2)$$

where T_e is the electron temperature.

The investigation of ion flow from vacuum arc plasma has shown that the ion current toward the anode is proportional to the arc current I with a coefficient $\alpha \approx 0.1$ [5]. Correspondingly, for the ion current density one can write

$$j_i = \alpha I/S, \quad (3)$$

0021-3640/02/7506-0257$22.00

where S is the plasma jet cross-section in the site where it interacts with the droplet.

Taking into account Eqs. (1)–(3), the expression for the energy w acquired from the plasma jet by a droplet with radius R_d has the form

$$w = \frac{3\alpha I(\bar{E}_i + \bar{U}_i + 2ZkT_e)}{4SZR_d\rho e}, \quad (4)$$

where ρ is the density of the cathode material. Notice that, according to Eq. (4), the specific energy is inversely proportional to the droplet radius.

Let us analyze the plasma jet parameters in Eq. (4) using the ecton model of the vacuum arc cathode spot [2]. According to the ecton model, the cathode spot consists of the individual cells emitting a portion of electrons–ecton. The current from the spot cell is approximately twice the arcing threshold current. As the arc current increases, the spot cells are grouped in an immediate vicinity of each other, because this is energetically more favorable for reproducing ecton processes. In this case, the plasma parameters are formed as a result of the functioning of an individual spot cell upon the explosive destruction of the cathode site under the action of a high-density current. Modeling of the ecton processes has demonstrated that the ionization processes are concentrated within a narrow region on the order of a micron near the cathode, and, after this, the ionization composition of arc plasma remains virtually unchanged [6]. Under the action of the electron pressure gradient, the ions acquire a velocity on the order of 10^6 cm/s in their directed motion even at a distance of several microns. Taking this into account, one may estimate the ion-flow parameters $\bar{E}_i$ and $\bar{U}_i$ in Eq. (1) using their values measured away from the cathode. We take Cu as the cathode material, because it was studied most thoroughly in the context of cathode processes and arc plasma properties. The mean ion kinetic energy and the mean ionization potential for Cu are, respectively, 56 and 20.4 eV [7, 8]. The electron temperature near the cathode equals ~3–4 eV [6]. Accordingly, the energy transfer [the expression in brackets in Eq. (4)] from the ions and electrons to the droplet is equal to ≈90 eV for a copper cathode.

The droplet fraction of cathode erosion plays an important role in the arc discharge self-sustaining process [2]. A thin waist forms at the instant of droplet detachment. The plasma ion current, which is closed to the droplet, flows through the waist. Since the ratio of the droplet surface area to the waist cross-section may be large, the current density in the waist may be high enough for its explosion and the appearance of an ecton. The characteristic time of an ecton process is ~20–30 ns [2]. With a velocity of 10^4 cm/s, the droplet moves from the cathode surface at a distance smaller than 2–3 μm. If, after the detachment, the droplet with a diameter of 0.1–0.2 μm is in the region of a plasma jet formed during the ecton functioning, then, according to Eq. (4), the value $w > 10^4$ J/g is achieved during 20–30 ns for an ecton current of 3.2 A even in the case of spherically symmetric plasma expansion; i.e., $S = 2\pi r^2$, where r is the distance from the cathode. Such a specific energy corresponds to a droplet temperature higher than 2 eV and, as was shown in the study of conductor electric explosion and initiation of explosive electron emission [2], is sufficiently high for the transition from a condensed to a plasma state.

We have demonstrated above that dense plasma can form during the functioning of an individual spot cell. The current buildup leads to an increase in the number of ectons and to droplet enlargement. Large plasma bunches may appear at a certain distance from the cathode surface when the spot moves to a new site, if the droplet formed during the functioning of the preceding cathode spot falls within the area of spot action. This process is quite possible because the spot velocity at the cathode surface (~10^4 cm/s) is comparable with the droplet flight velocity.

Let us consider droplet interaction with a collectivized plasma jet formed by an ensemble of simultaneously functioning ectons. To estimate the ion current density, we use the data from [9], according to which the cathode spot diameter at a current of 100 A is 10 μm. In this case, for a droplet with radius R_d = 0.5 μm at a distance of 5 μm from the cathode surface and a plasma jet with an expansion angle of 60° [10], the specific energy is higher than 10^4 J/g at t = 30 ns.

Thus, analysis based on the ecton model has shown that dense plasma bunches can form near the cathode as a result of the interaction of plasma jets and droplets emitted by the cathode spot of a vacuum arc.

REFERENCES

1. A. V. Batrakov, B. J. Jüttner, S. A. Popov, *et al.*, Pis'ma Zh. Éksp. Teor. Fiz. **75**, 84 (2002) [JETP Lett. **75**, 76 (2002)].
2. G. A. Mesyats, *Ectons in Vacuum Discharge: Breakdown, Spark, Arc* (Nauka, Moscow, 2000).
3. *Handbook of Vacuum Arc Science and Technology*, Ed. by R. L. Boxman, P. J. Martin, and D. M. Sanders (Noyes Publ., Park Ridge, 1995).
4. T. Utsumi and J. H. English, J. Appl. Phys. **46**, 126 (1975).
5. C. W. Kimblin, J. Appl. Phys. **44**, 3074 (1973).
6. S. A. Barengol'ts, G. A. Mesyats, and D. L. Shmelev, Zh. Éksp. Teor. Fiz. **120**, 1227 (2001) [JETP **93**, 1065 (2001)].
7. G. Yu. Yushkov, E. M. Oks, A. Anders, and I. G. Brown, J. Appl. Phys. **88**, 5618 (2000).
8. I. G. Brown, Rev. Sci. Instrum. **65**, 3061 (1994).
9. J. E. Daalder, IEEE Trans. Power Appar. Syst. **PAS-93**, 1747 (1974).
10. M. P. Reece, Proc. IEEE **110**, 793 (1963).

Translated by V. Sakun

JETP Letters, Vol. 75, No. 6, 2002, pp. 259–263. Translated from Pis'ma v Zhurnal Éksperimental'noĭ i Teoreticheskoĭ Fiziki, Vol. 75, No. 6, 2002, pp. 309–313.

Resonance Line Shape in a Magnetically Diluted System of an Arbitrary Dimensionality

F. S. Dzheparov* and I. V. Kaganov

Institute of Theoretical and Experimental Physics,
ul. Bol'shaya Cheremushkinskaya 25, Moscow, 117259 Russia
** e-mail: dzheparov@itep.ru*

Received January 31, 2002

Abstract—The third ($\propto C^2$) term in the concentration expansion of free induction decay is calculated for a magnetically diluted system of an arbitrary integer dimensionality $d \le 3$ and for different values of parameter a characterizing the relative intensity of flip–flop processes. The concentration expansion was used to generalize, in a natural way, the Anderson–Weiss–Kubo theory that was originally developed to describe magnetic resonance in ordered systems in terms of the second and fourth moments. The results are compared with recent absorption measurements in quasi-two-dimensional media. The possibility of describing the exchange narrowing is discussed. © *2002 MAIK "Nauka/Interperiodica".*

PACS numbers: 76.20.+q, 76.30.-v

1. The line shape and the Fourier-transform-related free induction decay (FID) belong to the most important observable phenomena in physics of magnetic resonance. In the study of nuclear spin systems forming a crystal lattice, it is highly important to know the first, and especially the second and the fourth, moments of the normalized line shape. The first three terms of the FID expansion in powers of squared time carry the same information [1]. In the theory of the line shape of disordered (magnetically diluted) electron spin systems, the first ($\propto C$ and $\propto C^2$) terms in the expansion in powers of the concentration C of paramagnetic centers plays the same role [2]. In spite of the important role of these quantities, the third ($\propto C^2$) term in the concentration expansion is yet to be calculated. Knowledge of the first terms of this expansion is particularly topical in connection with the new experiments on measuring the EPR spectra of paramagnetic impurities distributed at the solid surface [3, 4]. In this work, we focused on the third term in the concentration expansion of FID for a magnetically diluted system and considered the conclusions for the simplest FID model of a dipolar system introduced earlier in [5, 6] and, for other purposes, in [7]. The calculations were carried out for samples with an arbitrary integer dimensionality $d \le 3$ and in a wide range of parameter a, which specifies the ratio of the isotropic part to the so-called z–z part of the dipole–dipole interaction.

2. Let the paramagnetic centers (PCs) be randomly distributed in a d-dimensional crystal lattice with the unit-cell volume Ω. The free induction decay is given by

$$G(t) = \langle\langle S^+(t)S^-\rangle_0\rangle_c / \langle\langle S^+S^-\rangle_0\rangle_c, \qquad (1)$$

where

$$S^\pm = \sum_r n_r S_r^\pm, \quad S_r^\pm = S_r^x \pm iS_r^y,$$

$$S^+(t) = e^{iH_d t} S^+ e^{-iH_d t},$$

n_r is the occupation number $\{n_r = (0)1$ if the lattice site r is (not) occupied by spin S_r [2]$\}$, $\langle\ldots\rangle_0 = \mathrm{Tr}(\ldots)/\mathrm{Tr}1$ (high-temperature Gibbs average), $\langle\ldots\rangle_c$ stands for the averaging over the spatial spin distributions (i.e., over the occupation numbers n_r), and H_d is the secular part of the dipole–dipole interaction; it has the form

$$H_d = \frac{3}{4}\sum_{rq} n_r n_q A(\mathbf{r}, \mathbf{q})\left(S_r^z S_q^z - \frac{a}{3}\mathbf{S}_r\mathbf{S}_q\right). \qquad (2)$$

Here, $A(\mathbf{r}, \mathbf{q}) = \hbar\gamma^2(1 - 3\cos^2\vartheta_{rq})/|\mathbf{r} - \mathbf{q}|^3$, γ is the gyromagnetic ratio, and ϑ_{rq} is the angle between $\mathbf{r} - \mathbf{q}$ and the external static field $\mathbf{H}_0$. In the Anderson model, the parameter $a = 0$, and $a = 1$ for the purely dipole–dipole interactions. For other a values, Hamiltonian (2) corresponds to a system with the anisotropic axisymmetric g factor. In what follows, $S = 1/2$ for all PCs.

Let us expand FID in powers of n_x and perform configurational averaging on the assumption that the occupation numbers are independent for different sites [2]. To the terms $\propto O(C_d^3)$, one has

$$G(t) = 1 + C_d\int d^d r_1 (2K_{01}(t) - 1) + \frac{C_d^2}{2}\int d^d r_1 d^d r_2 (2K_{012}(t) - 2K_{01}(t) - 2K_{02}(t) + 1), \qquad (3)$$

0021-3640/02/7506-0259$22.00 © 2002 MAIK "Nauka/Interperiodica"

where C_d is the d-dimensional PC density (concentration), and

$$K_{01}(t) = \langle e^{iH_{01}t}S_0^+e^{-iH_{01}t}(S_0^- + S_1^-)\rangle_0,$$

$$K_{012}(t) = \langle e^{iH_{012}t}S_0^+e^{-iH_{012}t}(S_0^- + S_1^- + S_2^-)\rangle_0.$$

Here, according to Eq. (2),

$$H_{ij} = \frac{1}{2}A_{ij}(3S_i^zS_j^z - a\mathbf{S}_i\mathbf{S}_j),$$
$$H_{012} = H_{01} + H_{02} + H_{12}, \quad (4)$$

with $A_{ij} = A(\mathbf{r}_i, \mathbf{r}_j)$. The interaction $A_{ij} \propto |\mathbf{r}_i - \mathbf{r}_j|^{-3}$. For this reason, one can change integration variables $\mathbf{r}_i \longrightarrow t^{1/3}\mathbf{r}_i$ to exclude time from the integrands and establish that the mth term in Eq. (3) is proportional to $(C_dt^{d/3})^m$. That is, Eq. (3) is expanded in terms of the dimensionless parameter $(D_dt)^{d/3} = C_d\int d^dr_1(1 - 2K_{01}(t))$ [8] and, hence, can be represented as

$$G(t) = 1 - (D_dt)^{d/3} + \frac{1}{2}\xi_d(a)(D_dt)^{2d/3} + O((D_dt)^d). \quad (5)$$

The primary goal of our further analysis is to calculate the function $\xi_d(a)$.

It was shown in [2] that

$$K_{01}(t) = \langle \exp(iH_{01}^zt)S_0^+\exp(-iH_{01}^zt)S_0^-\rangle_0 = \frac{1}{2}\cos\left(\frac{3}{4}A_{01}t\right). \quad (6)$$

An important point is that both $K_{01}(t)$ and D_d are independent of a. This property generalizes the theorem [1] claiming that the second moment is independent of the isotropic interaction.

3. To calculate $K_{012}(t)$, we diagonalized the three-body potential H_{012}. Due to the axial symmetry, the entire space of three-spin states with dimensionality $N_3 = (2S + 1)^3 = 8$ can be classified naturally by the eigenvalues M of the operator $S^z = S_0^z + S_1^z + S_2^z$, with the energies $E^{(M)}$ being independent of the sign of M. This follows, for example, from the fact that H_{012} is invariant about the rotation $R = \exp(i\pi S^y)$ by an angle of π about the Y axis in the spin space. The eigenvalues and eigenvectors of the operator H_{012} for $M = \pm 3/2$ are straightforward:

$$|3/2\rangle = |\uparrow\rangle|\uparrow\rangle|\uparrow\rangle, \quad |-3/2\rangle = |\downarrow\rangle|\downarrow\rangle|\downarrow\rangle,$$
$$E^{(\pm 3/2)} = \frac{1}{4}(A_{01} + A_{02} + A_{12}). \quad (7)$$

The subspaces with $M = \pm 1/2$ are three-dimensional and formed, e.g., for $M = 1/2$, by the linear combinations of vectors $|\psi_\alpha\rangle = S_\alpha^-|3/2\rangle$ ($\alpha = 0, 1, 2$); the Hamiltonian matrix $Q_{\alpha\beta} = \langle\psi_\alpha|H_{012}|\psi_\beta\rangle$ is real and symmetric if the Pauli matrices are taken in the standard form, and its eigenvectors $|\alpha\rangle$ satisfying equation

$$Q|\alpha\rangle = E_\alpha^{(1/2)}|\alpha\rangle$$

can be chosen to be real. In the $M = -1/2$ subspace, the $|\phi_\alpha\rangle = R|\psi_\alpha\rangle$ basis is suitable. In this case, $\langle\phi_\alpha|H_{012}|\phi_\beta\rangle = \langle\psi_\alpha|H_{012}|\psi_\beta\rangle$. Now, considering that $G(t)$ is a real function and introducing the matrices $J_{\alpha\beta}^i = \langle\phi_\alpha|S_i^-|\psi_\beta\rangle$ and $J = \sum_{i=0}^2 J^i$ and the vector $|\psi\rangle = \sum_{\beta=0}^2|\psi_\beta\rangle$, one arrives at the representation

$$\mathrm{Re}K_{012}(t) = \frac{1}{4}\left(\sum_{\alpha=0}^2 W_\alpha(\cos(\mu_\alpha t) - 1) + \sum_{\alpha=0}^1\sum_{\beta=\alpha+1}^2 Z_{\alpha\beta}(\cos(\nu_{\alpha\beta}t) - 1)\right) + \frac{1}{2} = \sum_{j=1}^6\gamma_j(\cos(\lambda_jt) - 1) + \frac{1}{2}, \quad (8)$$

where $W_\alpha = \langle\psi|\alpha\rangle\langle\alpha|\psi_0\rangle$, $Z_{\alpha\beta} = J_{\alpha\beta}J_{\alpha\beta}^0$, $\mu_\alpha = E_\alpha^{(1/2)} - E^{(3/2)}$, and $\nu_{\alpha\beta} = E_\alpha^{(1/2)} - E_\beta^{(1/2)}$. The last relationship in Eq. (8) defines the parameters γ_j and λ_j, which will be used below.

The matrices $Q_{\alpha\beta}$ were diagonalized numerically. In doing so, the characteristic equation for the eigenvalues $E_\alpha^{(1/2)}$ was solved using the Cardano formula.

To reduce the domain of numerical integrations in Eq. (3), spherical coordinates were used [e.g., $\mathbf{r_j} = r_j(\sin\theta_j\cos\phi_j, \sin\theta_j\sin\phi_j, \cos\theta_j)$ for $d = 3$], whereupon the change of variables $r_1 = R\cos\alpha$, $r_2 = R\sin\alpha$ was applied. As a result, only the cosine arguments remain R-dependent in the integrand of the C_d^2 term in Eq. (3); in particular,

$$\mathrm{Re}K_{012}(t) = \sum_{j=1}^6\gamma_j(\cos(\lambda_j^0t/R^3) - 1) + \frac{1}{2}, \quad (9)$$

where $\lambda_j^0 = \lambda_j(R = 1)$. Hereafter, the upper zero index is omitted. Thereafter, the integral over R was calculated analytically and the remaining integrals were calculated numerically.

In the case of $d = 3$, one has the well-known Anderson result for D_3: $D_3 = \frac{2\pi^2}{3\sqrt{3}} C_3\gamma^2\hbar$, and

$$\xi_3 = \frac{9}{16\pi^3}\int_0^{\pi} d\phi d\theta_1 d\theta_2 \sin\theta_1 \sin\theta_2 \times \int_0^{\pi/2} d\alpha \sin^2 2\alpha \left(2\sum_{j=1}^{6} \gamma_j \lambda_j^2 \ln|\lambda_j| - \frac{9}{8}A_{01}^2 \ln\left|\frac{3}{4}A_{01}\right| - \frac{9}{8}A_{02}^2 \ln\left|\frac{3}{4}A_{02}\right| \right). \quad (10)$$

Let us now consider the lower dimensionalities $d = 2$ and 1. In this case, Eq. (5) depends on the orientation of magnetic field $\mathbf{H}_0$ in the sample. We restrict ourselves to the experimental situation where all field directions are equally probable and perform averaging in Eq. (5) over these directions. The result is

$$\bar{G}(t) = 1 - (\bar{D}_d t)^{d/3} + \frac{\bar{\xi}_d(a)}{2}(\bar{D}_d t)^{2d/3} + O((\bar{D}_d t)^d). \quad (11)$$

To analyze the case of surface spin distribution, we introduce the angle β between the projection $\mathbf{H}_p$ of field $\mathbf{H}_0$ onto the plane and the field $\mathbf{H}_0$ itself and the angle θ between the two-dimensional vector $\mathbf{r}$ and $\mathbf{H}_0$. Clearly, $\cos\theta = \cos\beta\cos\phi$, where ϕ is the polar angle measured from $\mathbf{H}_p$ to $\mathbf{r}$. It is also taken into account that $\cos\theta_{r_1 r_2} = (r_1\cos\theta_1 - r_2\cos\theta_2)/r_{12}$ and $r_{12}^2 = r_1^2 + r_2^2 - 2r_1 r_2\cos(\phi_2 - \phi_1)$. Then, by analogy with the case of $d = 3$, one has $\bar{D}_2 = \beta_2\gamma^2\hbar C_2^{3/2}$, where [3]

$$\beta_2 = 4.647 = \frac{3}{32} \times \left(\Gamma\left(\frac{1}{3}\right) \int_0^{\pi/2} d\sin\beta \int_0^{2\pi} d\phi \left|1 - 3\cos^2\beta\cos^2\phi\right|^{2/3} \right)^{3/2}, \quad (12)$$

and $\bar{\xi}_2$ has the form

$$\bar{\xi}_2 = \frac{3\Gamma(2/3)}{16\beta_2^{4/3}} \int_0^{\pi/2} d\sin\beta \int_0^{2\pi} d\phi_1 d\phi_2 \int_0^{\pi/2} d\alpha \sin 2\alpha \times \left[\left|\frac{3}{4}A_{01}\right|^{4/3} + \left|\frac{3}{4}A_{02}\right|^{4/3} - \sum_{j=1}^{6} \gamma_j |\lambda_j|^{4/3} \right]. \quad (13)$$

If $d = 1$, i.e., if the spins are arranged on a line forming an angle θ with the field $\mathbf{H}_0$, then $A_{ij} = (1 - 3\cos^2\theta)/r_{ij}^3$, $\bar{D}_1 = \beta_1\gamma^2\hbar C_1^3$, and

$$\beta_1 = 6\pi^3 \left(\int_0^{\pi/2} \frac{d\theta}{\Gamma\left(\frac{1}{3}\right)} \sin\theta \left|1 - 3\cos^2\theta\right|^{1/3} \right)^3 = 6.348,$$

$$\bar{\xi}_1 = \frac{\pi}{2\sqrt{3}\beta_1^{2/3}\Gamma(2/3)} \int_0^{\pi/2} d\theta \sin\theta \int_0^{2\pi} d\alpha \times \left[\left|\frac{3}{4}A_{01}\right|^{2/3} + \left|\frac{3}{4}A_{02}\right|^{2/3} - \sum_{j=1}^{6} \gamma_j |\lambda_j|^{2/3} \right]. \quad (14)$$

Numerical calculations yield the following values:

a:	0.2	0.4	0.6	0.8	1.0	1.2	1.4	1.6
ξ_3:	1.01	1.03	1.05	1.08	1.11	1.13	1.15	1.18
$\bar{\xi}_2$:	1.07	1.11	1.15	1.19	1.22	1.25	1.27	1.29
$\bar{\xi}_1$:	1.16	1.20	1.25	1.28	1.32	1.35	1.37	1.40

(15)

The $\xi_d(a = 0)$ values can conveniently be evaluated using the obvious fact that the Anderson model is exactly solvable for all d and that for a fixed orientation of external field [9]

$$G_A(t) = G(t, a = 0) = \exp(-(D_d t)^{d/3}), \quad (D_d t)^{d/3} = C_d \int d^d r_1 (1 - \cos(3A_{01}t/4)). \quad (16)$$

It follows that $\bar{\xi}_d(a = 0) = \overline{(D_d^{d/3})^2}/(\bar{D}_d^{d/3})^2$, where the overline denotes averaging over the $\mathbf{H}_0$ directions and

$$\xi_3(0) = 1, \quad \bar{\xi}_2(0) = 1.027, \quad \bar{\xi}_1(0) = 1.062. \quad (17)$$

4. The above results can be used directly for determining the parameter a from the experimentally measured resonance line wing for $d < 3$. Indeed, after writing expansion (11) in the form $\bar{G}(t) = \sum_{m \geq 0} q_m (\bar{D}_q t)^{dm/3}$ and passing to the frequency representation, one obtains

$$g_d(\omega) = \int_0^{\infty} \frac{dt}{\pi} e^{-\varepsilon t} \cos(\omega t) G(t) = -\frac{1}{\pi\omega} \sum_{m \geq 1} q_m \Gamma\left(1 + \frac{dm}{3}\right) \left(\frac{\bar{D}_d}{\omega}\right)^{dm/3} \sin(\pi dm/6), \quad (18)$$

where $\varepsilon \longrightarrow +0$. The terms with even $dm/3$ make no contribution to the asymptotic behavior of expansion (18) in powers of $1/\omega$. For this reason, one has for the line wing

$$g_3(\omega) = \frac{1}{\pi\omega}\left(\frac{D_3}{\omega}\right)^1 \left(1 + O\left(\left(\frac{D_3}{\omega}\right)^2\right)\right), \quad (19)$$

$$g_2(\omega) = \frac{1}{\pi\omega}\left(\Gamma\left(\frac{5}{3}\right)\sin\left(\frac{\pi}{3}\right)\left(\frac{\bar{D}_d}{\omega}\right)^{2/3}\right.$$

$$\left. - \frac{\bar{\xi}_2}{2}\Gamma\left(\frac{7}{3}\right)\sin\left(\frac{2\pi}{3}\right)\left(\frac{\bar{D}_d}{\omega}\right)^{4/3} + O\left(\left(\frac{\bar{D}_d}{\omega}\right)^{8/3}\right)\right),$$

$$g_1(\omega) = \frac{1}{\pi\omega}\left(\Gamma\left(\frac{4}{3}\right)\sin\left(\frac{\pi}{6}\right)\left(\frac{\bar{D}_d}{\omega}\right)^{1/3}\right.$$

$$\left. - \frac{\bar{\xi}_1}{2}\Gamma\left(\frac{5}{3}\right)\sin\left(\frac{\pi}{3}\right)\left(\frac{\bar{D}_d}{\omega}\right)^{2/3} + O\left(\frac{\bar{D}_d}{\omega}\right)\right).$$

Evidently, the expression for $d = 3$ is independent of ξ_d, and the case of $d = 2$ is most suitable for measuring $\bar{\xi}_d(a)$, because the gap between the first two ($\propto\omega^{-5/3}$ and $\propto\omega^{-7/3}$) and the third ($\propto\omega^{-11/3}$) asymptotic terms is large in this case.

The first ($\propto\omega^{-5/3}$) term in the expansion of $g_2(\omega \longrightarrow \infty)$ was already considered in [10].

5. At present, the methods of obtaining satisfactory approximations for the FID $G(t)$ and for the line shape $g_d(\omega)$ for arbitrary t and ω were developed using the method of memory function [2] or the cumulant and cluster expansions [5, 6]. We will restrict ourselves to the discussion of one of the simplest approaches [7, 5, 6] that introduces the most essential properties of the disordered systems into the Anderson–Weiss–Kubo (AWK) theory [11, 12], which was originally developed for the description of motional line narrowing. This approach is based on the fact that, if the FID is calculated approximately using the exactly soluble Anderson model and the Gaussian approximation with $\tilde{M}_2 = \frac{9}{16}\sum_r n_r A(r)$ for the second moment in a fixed configuration and the result is then averaged over the disorder, one arrives at the functionally correct result

$$G(t, a = 0) = \langle \exp(-\tilde{M}_2 t^2/2)\rangle_c = \exp(-(B_d t)^{d/3}),$$

which differs from the exact solution only by the replacement $D_d \longrightarrow B_d = bD_d$, where $b \approx 1$. If the temporal fluctuations are also introduced in the theory and the local field $w_l(t)$ is considered as a normal random process, i.e.,

$$\langle \omega_l(t)\omega_l(t_1)\rangle = M_2 f(|t - t_1|),$$

then one additionally obtains the qualitatively correct asymptotic expression $\ln G(\bar{D}_d t \gg 1) \propto -(\bar{D}_d t)^{d/6}$. On the whole, the theory gives the following representation for the FID:

$$G(t) = \exp\left(-\left(2B_d^2\int_0^t d\tau(t-\tau)F(B_d\tau)\right)^{d/6}\right). \quad (20)$$

When deriving this formula, it is assumed that the second moment $\tilde{M}_2$ accounts for the most essential spatial fluctuations, so that it suffices to take the function $F(B_d\tau)$ reflecting the temporal fluctuations of local fields as $F(B_d\tau) = f(|\tau|) = \langle f(|\tau|)\rangle_c$.

Recall that the AWK FID in the ordered system has the following form:

$$G_0(t) = \exp\left(-M_2\int_0^t d\tau(t-\tau)F_0(\tau)\right). \quad (21)$$

This formula satisfactorily describes the line shape even with the simplest function $F_0(t) = \exp(-(kt)^2/2)$, provided that the parameter k is derived from the second (M_2) and fourth (M_4) moments.

The function $F(x) = \exp(-q_d x)^{d/3})$ is the simplest for a disordered system. With this function, the structure of expansion (5) is retained, the line shape is nonnegative, and the parameters B_d and q_d can be determined from the first two terms of the concentration expansion, i.e., from D_d and ξ_d. We will implement this program using Eq. (5) for $d = 3$ and Eq. (11) for $d = 2$. Evidently, in this case $B_3 = D_3$ and $B_2 = \bar{D}_2$, and simple mathematics gives

$$q_3 = 3(\xi_3 - 1), \quad q_2 = ((10/3)(\bar{\xi}_2 - 1))^{3/2}. \quad (22)$$

The case when $d = 1$ requires a more thorough analysis, so we do not consider it here. The challenge is that some of the random orientations in a one-dimensional system are close to the magic direction $\theta = \arccos(1/\sqrt{3})$. The evolution for these orientations is abnormally slow, giving $g_1(\omega \longrightarrow 0) \propto \ln(1/\omega)$.

In closing this section, we present the calculated position $\Delta(a)$ of the right extremum in the absorption signal of a $d = 2$ system

$$g'(\omega) = \partial g(\omega)/\partial\omega$$

for different values of q_2 [by definition, $g''(\Delta) = 0$]:

$1/q_2$:	1	2	4	8	16	32
$\Delta/\bar{D}_2$:	0.011	0.026	0.070	0.114	0.143	0.162

6. When applied to the standard dipolar interaction ($a = 1$), Eqs. (22) and (15) give $q_3 = 0.33$ and $q_2 = 0.63$. Fitting to the experimental data [3] in the region where the sample was considered to two-dimensional gives $q_2 = q_2^{\exp} \approx 0.05$, which differs significantly from both $q_2 = 0$ and $q_2 = 0.63$. Such a small value of the parameter modeling local field fluctuations was obtained in [3] within a somewhat different mathematical FID model. However, no theoretical predictions existed for this parameter at that time. The elucidation of the nature of

these deviations from the purely dipolar evolution calls for further investigation.

7. In conclusion, let us discuss the motional narrowing on the qualitative level. In the simplest version, it would suffice to consider the limit $G(t, a \longrightarrow \infty)$ modeling the long-range RKKY interaction.

The exchange narrowing was traditionally described using mathematical model (21). Inasmuch as M_2 is independent of a and $M_4 \propto a^2$, $G(t, a \gg 1) = G_0(t) = \exp(-w_0 t)$, where $w_0 \sim \sqrt{M_2}/a$. The quantity M_2 in this expression is averaged over the impurity configurations; to our knowledge, in the principle works this was assumed by default. The authors of [7] made allowance for the spatial and temporal local-field fluctuations in a three-dimensional system using a model represented, in our notation, by Eq. (20) with $F(x) = \exp(-ca^2x^2/2)$ and $c \sim 1$. Clearly, this gives

$$G(t, a \gg 1) = G_1(t) = \exp(-(w_1 t)^{d/6}),$$

where $w_1 \sim D_d/a$. This formula also predicts motional narrowing, but the explicit form of the FID and the resonance line shape are cardinally different. Experimentally, however, the purely Lorentzian lines are observed over a wide range of parameters, in accordance with the more simple FID $G_0(t)$, which, in particular, was verified in [3] in the exchange-narrowing region.

In our opinion, the reason as to why the motionally narrowed lines are practically Lorentzian is as follows. The FID corresponds to the evolution of a system with the initial state

$$\rho = \exp(-\beta S_x)/\mathrm{Tr}\exp(-\beta S_x), \qquad (23)$$

where S_x is the operator of the x component of the total angular momentum of the system. At large a and $t > \tau_c \propto 1/a$, the system is in quasi-equilibrium, which is equilibrium for the exchange part H^{ex} of the total interaction. The state (23) is precisely the state of this type, because H^{ex} commutes with the operator of total spin: $[H^{ex}, \mathbf{S}] = 0$. Because of this, the exchange narrowing can be correctly described by the standard projection technique [13] with the density matrix [23] [with $\beta = \beta(t)$] taken as its dominant part, which, after standard calculations, again leads to the Lorentz-shaped exchange-narrowed resonance line. The conceptual significance of quasi-equilibrium (23) was earlier pointed out in [14], but the methods used in that work for calculating the time T_2 are now out of date, so that the methods used in our work will, likely, give rise to somewhat different parametric dependences. We intend to consider this issue in a separate work. Note also that the picture becomes much more complicated for the exponential dependence of the exchange interaction on the distance between spins: due to the chaotic spatial PC distribution, quasi-equilibrium (23) will apply only to those spins which form sufficiently large exchange-coupled clusters.

We thank V.A. Atsarkin and V.V. Demidov for helpful discussions. This work was supported by the Russian Foundation for Basic Research, project nos. 99-02-17440 and 00-15-96656.

REFERENCES

1. A. Abragam and M. Goldman, *Nuclear Magnetism: Order and Disorder* (Clarendon, Oxford, 1982; Mir, Moscow, 1984).
2. F. S. Dzheparov, A. A. Lundin, and T. N. Khazanovich, Zh. Éksp. Teor. Fiz. **92**, 554 (1987) [Sov. Phys. JETP **65**, 314 (1987)].
3. V. A. Atsarkin, G. A. Vasneva, V. V. Demidov, *et al.*, Pis'ma Zh. Éksp. Teor. Fiz. **72**, 530 (2000) [JETP Lett. **72**, 369 (2000)].
4. V. A. Atsarkin, V. V. Demidov, G. A. Vasneva, *et al.*, J. Magn. Reson. **149**, 85 (2001).
5. F. S. Dzheparov and E. K. Khenner, Zh. Éksp. Teor. Fiz. **104**, 3667 (1993) [JETP **77**, 753 (1993)].
6. F. S. Dzheparov, I. V. Kaganov, and E. K. Khenner, Zh. Éksp. Teor. Fiz. **112**, 596 (1997) [JETP **85**, 325 (1997)].
7. E. S. Grinberg, B. I. Kochelaev, and G. G. Khaliullin, Fiz. Tverd. Tela (Leningrad) **23**, 397 (1981) [Sov. Phys. Solid State **23**, 224 (1981)].
8. F. S. Dzheparov, V. S. Smelov, and V. E. Shestopal, Pis'ma Zh. Éksp. Teor. Fiz. **32**, 51 (1980) [JETP Lett. **32**, 47 (1980)].
9. E. B. Fel'dman and S. Lacelle, J. Chem. Phys. **104**, 2000 (1996).
10. A. A. Lundin, in *Modern Methods of NMR and ESR in Chemistry of Solid State* (Chernogolovka, 1990), p. 137.
11. P. W. Anderson and P. R. Weiss, Rev. Mod. Phys. **25**, 269 (1953).
12. R. Kubo, J. Phys. Soc. Jpn. **17**, 1100 (1962).
13. K. Kawasaki and J. D. Gunton, Phys. Lett. A **40A**, 35 (1972).
14. N. S. Bendiashvili, L. L. Buishvili, and M. D. Zviadadze, Fiz. Tverd. Tela (Leningrad) **10**, 1224 (1968) [Sov. Phys. Solid State **10**, 971 (1968)].

Translated by V. Sakun

JETP Letters, Vol. 75, No. 6, 2002, pp. 264–267. Translated from Pis'ma v Zhurnal Éksperimental'noĭ i Teoreticheskoĭ Fiziki, Vol. 75, No. 6, 2002, pp. 314–317.

Optical Phonons in Ge Quantum Dots Obtained on Si(111)

A. B. Talochkin and S. A. Teys

Institute of Semiconductor Physics, Siberian Division, Russian Academy of Sciences, Novosibirsk, 630090 Russia
e-mail: tal@thermo.isp.nsc.ru

Received February 6, 2002

Abstract—The Raman light scattering from optical phonons of Ge quantum dots grown by molecular beam epitaxy on a Si(111) surface is studied. A series of Raman lines related to the quantization of phonon spectrum is observed. It is shown that phonon frequencies are adequately described in terms of the elastic properties and the dispersion of the optical phonons of bulk Ge. The strain experienced by the Ge quantum dots is estimated. © *2002 MAIK "Nauka/Interperiodica".*

PACS numbers: 78.67.Hc; 63.22+m

Semiconductor quantum dots (QD) are obtained by molecular beam epitaxy (MBE) in strained InAs/GaAs, Ge/Si, and other similar structures. As a rule, the self-consistent growth of QD occurs on a surface with the (100) orientation for which the QD are pyramidal. The pyramid height-to-base ratio is 1 : 3 for InAs QD in GaAs and 1 : 10 for Ge QD in Si. This form of QD and the difference in the lattice constants of the QD and matrix materials lead to a nonuniform strain distribution in the QD. For InAs QD in GaAs, the strain distribution was calculated in [1], and for Ge QD in Si, in [2, 3]. The strained state of Ge QD in Si was studied experimentally in [4, 5]. The nonuniform strain distribution makes the analysis of the electron spectra and other QD parameters more complicated. Therefore, the studies of unstrained QD [6] or QD with uniform strain distributions are of particular interest. In some publications (e.g., [7, 8]), it was noted that the epitaxial growth of Ge on the (111) surface of Si differs essentially from the growth on the (100) surface. The Ge islands obtained on Si(111) have the form of truncated pyramids whose upper and lower faces are close in size. In this case, the strained state of the Ge QD in the Si matrix should be close to that under a uniform hydrostatic pressure. In this paper, we report on the study of the dimensions and shape of the Ge QD obtained on Si(111) in the case of submonolayer coatings. In the spectra of the Raman light scattering from the optical phonons of the Ge QD, we observed a series of lines related to the quantization of the optical phonon spectrum of the QD in the growth direction; we also determined the strain value for the QD.

The growth of Ge QD on Si substrates with the (111) orientation was conducted in the ultrahigh vacuum chamber of an Omicron scanning tunneling microscope (STM), which allowed us to study *in situ* the shape and dimensions of Ge islands, as well as monitor the state of both Si and Ge surfaces. The Si plates were first subjected to a standard chemical treatment. Then, the plates were placed in the vacuum chamber where their surfaces were additionally cleaned by heating to T = 1250°C (by a direct current) with subsequent gradual cooling to 400°C. The deposition of Ge on Si(111)7×7 was performed at the substrate temperature T_s = 350–500°C, at a rate within 0.03–0.0003 nm/min. At the temperatures of Ge growth, the Si surface had a 7×7 superstructure. This surface reconstruction essentially differs from the 2×1 superstructure characteristic of the Si(100) surface. The formation of the Si(100)2×1 cell is associated with the displacement of the atoms of the surface layer in the growth plane and with the formation of the so-called dimers (with π bonds) [8]. The Si(111)7×7 superstructure is characterized by the rearrangement of atoms in three surface layers [9]. The 7×7 cell consists of two mirror-symmetric triangular subcells with π-bonded dimer chains formed along their boundaries. In one half of the 7×7 cell, the atoms of the surface layer are rotated through 180° in the (111) plane relative to their position in the bulk of the crystal (a stacking fault). In the corners of the rhombic 7×7 cell, deep vacancy-type stacking faults are formed as a result of the absence of four atoms in the regular crystal structures of the second and third layers. These reconstruction features determine the difference in the formation of Ge QD on the Si(100) and Si(111) surfaces.

In the regular MBE regimes with relatively high rates of Ge deposition (0.3–3 nm/min), the layer growth of the film is observed up to a critical thickness of ~6 m.l. = $3a_0$ (where a_0 is the Ge lattice constant in the [111] direction and m.l. denotes the monatomic layer whose thickness is 1.3 Å), after which three-dimensional Ge islands begin to form. At lower Ge deposition rates, the growth of pyramidal islands with a flat top and a height of 6 m.l. is observed. In the course of the growth process, the dimensions of these islands in the (111) plane increase, whereas their height remains constant, and, finally, the islands form a continuous layer. Figure 1a shows the STM image of a 210×210 nm sur-

face area with $a \sim 0.7$-m.l.-thick Ge coating. (The image was obtained with a tunneling current of 0.05 nA.) The island density is $\sim 2 \times 10^{10}$ cm^{-2}, and the height of the majority (80%) of the islands is 6 m.l. The proportions of islands with the heights 4 m.l. (denoted by number *2* in Fig. 1a) and 2 m.l. (number *1* in Fig. 1a) are insignificant: 18 and 2%, respectively. The average size of the islands in the (111) plane is ~ 40 nm (the triangle base). This value far exceeds the maximal island height, which is equal to 1 nm. Figure 1b shows an isolated island whose height is equal to 6 m.l.

Note that the presence of the surface reconstruction in the form of the 7×7 structure on the initial growth surface of Si produces an organizing effect on the Ge atoms deposited on this surface. This is confirmed by the following facts: (i) at the beginning, the Ge atoms are accumulated in halves of the unit cells of the 7×7 structure; (ii) the size of the islands in the (111) plane is a multiple of the size of the 7×7 unit cell, because the surface structure of the substrate is reproduced at the surface of a Ge island; and (iii) the edges of the triangular Ge islands end at the cell boundaries of the Si surface structures.

The spectra of the Raman scattering from the optical phonons of the fabricated structures were excited by an Ar laser line with $\lambda = 488$ nm and recorded by a DFS-52 spectrometer. To avoid oxidation of Ge, the structures were removed from the growth chamber and placed in a cryostat with liquid nitrogen. The Raman spectrum measurements performed in atmosphere at $T = 300$ K showed that the complete oxidation of Ge occurred within ~ 20 min. Since the sample was transferred from the vacuum chamber to the cryostat in nitrogen vapor within ~ 30 s, the oxidation that occurred during this procedure could be ignored. Figure 2 presents the spectrum of the Raman scattering from the optical phonons of a Ge/Si(111) sample whose STM image is shown in Fig. 1. The spectrum exhibits a series of phonon lines denoted in Fig. 2 as TO_1, TO_2, LO_1, LO_2, and LO_3. The position of the bulk phonon of Ge at $T = 77$ K (305 cm^{-1}) is indicated by the vertical arrow. The bulk phonons observed in the Raman spectra of Ge at $\mathbf{k} = 0$ are threefold degenerate (LO + 2TO). In our case, the degeneracy is eliminated owing to the presence of stress, because the QD are strained due to the difference in the lattice constants of Si and Ge ($\Delta a = 4\%$). In addition, the phonon spectrum is quantized in the [111] direction because of the relatively small height of the QD. These two factors determine the optical phonon frequencies observed in the experiment.

Let us consider the strain in the Ge QD obtained on Si(111) and the effect of this strain on the phonon spectrum. The Ge islands are strained (compressed) in the growth plane. Since the size of the QD in the plane is much greater than the QD height, the effect of lateral faces can be ignored and the strain can be considered as uniform. We denote the components of the strain tensor in the growth plane as $\varepsilon_{xx} = \varepsilon_{yy} = \varepsilon$. In the growth direction *z*, Ge experiences tension. The component ε_{zz} is determined from the boundary condition $\sigma_{zz} = 0$, where σ_{zz} is the stress tensor component. By transforming the strain tensor to the (100) system and applying the Hooke law, we determine the components of the stress

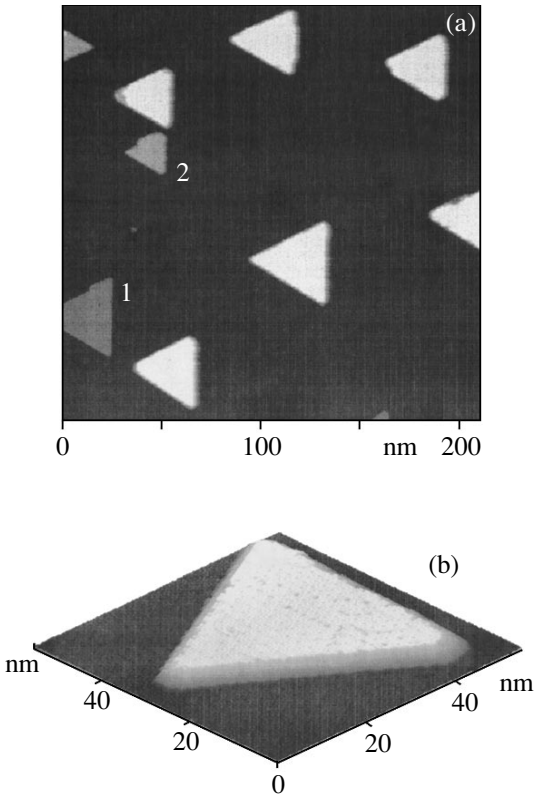

Fig. 1. STM image of a Si(111) 7×7 surface with Ge islands: (a) Ge islands obtained at a temperature of 400°C, a Ge coating thickness of ~ 0.7 m.l., and a deposition rate of 0.0005 nm/min; (b) an isolated Ge island whose height is equal to 6 m.l.

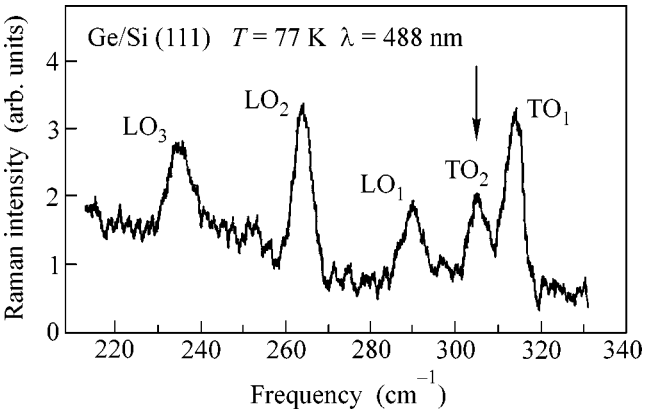

Fig. 2. Spectrum of Raman scattering from the optical phonons of Ge QD obtained on a Si(111) surface. The spectrum is recorded at $T = 77$ K with the excitation wavelength $\lambda = 488$ nm.

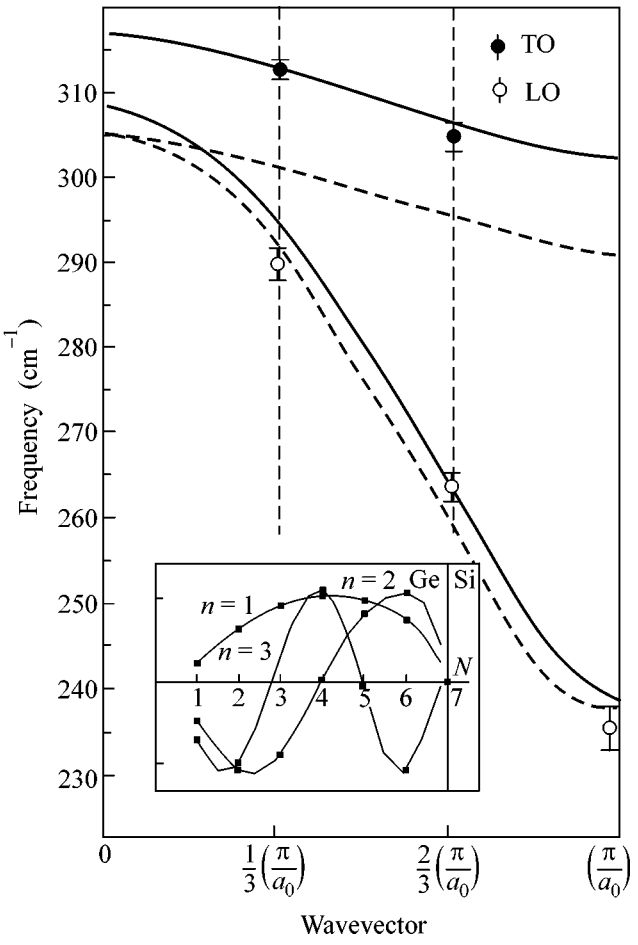

Fig. 3. Dispersion curves calculated in [12] for the optical phonons of Ge in the [111] direction (the dashed lines) and the dispersion curves obtained with allowance for the strain in Ge (the solid lines). The circles indicate the optical phonon frequencies measured in the Ge quantum dots. The inset shows the atomic oscillation amplitudes calculated in the framework of a one-dimensional chain model.

tensor in this system. After an inverse transformation with the use of the boundary condition, we arrive at the expression $\varepsilon_{zz} = -2\exp C_{44}(C_{11} + 2C_{12} - C_{44})/(C_{11} + 2C_{12} - C_{44}) = 0.92\varepsilon$, where C_{11}, C_{12}, and C_{44} are the components of the elastic compliance tensor of Ge. The components of the stress tensor in the growth plane are $\sigma = \sigma_{xx} = \sigma_{yy} = 3C_{44}\varepsilon(C_{11} + 2C_{12})/(C_{11} + 2C_{12} - C_{44})$. These stresses split the state of the optical phonon with $\mathbf{k} = 0$ into the singlet (LO) and doublet (TO) states. The expressions for the dependences of the frequencies of these phonons on the biaxial stress in the plane perpendicular to [111] were obtained in [10]:

$$\Omega_L = \omega_0 + \Delta\Omega_h - (1/3)\Delta\Omega, \quad (1)$$

$$\Omega_T = \omega_0 + \Delta\Omega_h + (2/3)\Delta\Omega, \quad (2)$$

where ω_0 is the frequency of the optical phonons in Ge; $\Delta\Omega_h = 2\sigma(S_{11} + 2S_{12})(\mathbf{p} + 2\mathbf{q})/6\omega$ is the hydrostatic component of the frequency shift; $\Delta\Omega = \Omega_T - \Omega_L = \sigma S_{44}\mathbf{r}/2\omega_0$ is the magnitude of the LO–TO splitting; S_{11}, S_{12}, and S_{44} are the components of the elasticity tensor; and $\mathbf{p}$, $\mathbf{q}$, and $\mathbf{r}$ are the anharmonic coefficients of Ge, which were experimentally determined in [11]: $\mathbf{p} = -1.47\omega_0^2$, $\mathbf{q} = -1.93\omega_0^2$, and $\mathbf{r} = -1.08\omega_0^2$. After the substitution of all aforementioned parameters into Eqs. (1) and (2), the latter are reduced to the form $\Delta\Omega_T = \Omega_T - \omega_0 = -1.306\varepsilon\omega_0$ and $\Delta\Omega_L = \Omega_L - \omega_0 = -1.322\varepsilon\omega_0$. Below, we will use the strain ε as the adjustable parameter.

The height of the Ge QD is $h = 3a_0$, which leads to a considerable modification of the phonon spectrum. The spectrum of phonons with the wave vectors $\mathbf{k}$ along the [111] direction is quantized according to the condition of the formation of a standing wave: $k_n = (\pi/h)n$, where n is an integer. Thus, we can see that three oscillation modes of TO and LO phonons ($n = 1, 2, 3$) exist in the Brillouin zone. The inset in Fig. 3 shows the calculated oscillation amplitudes of atoms (N) for three longitudinal optical modes ($n = 1, 2, 3$). The calculations were performed for the model of a one-dimensional chain of six atoms. It was assumed that the oscillation amplitude becomes zero at $N = 7$ (i.e., at the Si boundary) and the first atom has a dangling bond (the free surface). The value of the force constant of the Ge–Si bond formed at the heteroboundary was determined from the frequency of the Ge–Si oscillations (400 cm^{-1}) and proved to be 40% greater than the corresponding value for the Ge–Ge bonds. The calculations showed that the mode frequencies are virtually the same as those obtained for a chain with only Ge–Ge bonds and with fixed ends; i.e., the decrease in the oscillation frequency because of the dangling bonds at the surface is compensated by its increase due to the more rigid Ge–Si bond. This means that the frequencies of the quantized phonon modes must correspond to the spatial dispersion of phonons in Ge.

Figure 3 presents the dispersion of phonons in Ge in the first Brillouin zone for the [111] direction. The circles show the experimental values of the phonon frequencies corresponding to the wave vectors k_n with $n = 1, 2, 3$. The dashed lines show the dispersion curves calculated in [12] for the optical phonons in Ge for the [111] direction. The solid lines show the dependences obtained by shifting the theoretical curves [12] according to Eqs. (1) and (2). For the TO and LO phonons, these shifts are $\Delta\Omega_T$ and $\Delta\Omega_L$, respectively. The value of the strain ε was determined from the condition of the best agreement with the experimental frequency values. As a result, we obtained $\Delta\Omega_T = 11.5$ cm^{-1} and $\Delta\Omega_L = 2.8$ cm^{-1}, and the strain value determined from the aforementioned condition was found to be $\varepsilon = -0.029 \pm 0.003$. From Fig. 3, one can see that the experimental values agree well with the dispersion curves, which allows us to explain the nature of the phonon modes observed in the Ge QD. The slight deviations of the LO phonon frequency (Fig. 3) from the dispersion curve

are related to the fact that the theoretical curves [12] were adjusted to the experimental data obtained by neutron scattering. For these data, the error was within ~2%, and the aforementioned deviations do not exceed this value.

Note that the strain value determined above ($\varepsilon = -0.029 \pm 0.003$) somewhat differs from the value –0.04, which characterizes the pseudomorphous growth of Ge on Si and is observed for Ge QD obtained on Si(100) [5]. We attribute this difference to the reconstruction of the (111) surface of the Ge islands. The boundaries of the 7×7 cells are associated with the rearrangement of atoms in the three atomic layers nearest to the surface, and these boundaries have a looser packing of atoms, as compared to the bulk structure inside the cells [9]. This fact may lead to a stronger deformation of these regions and to a partial release of stress in the cells, so that the average strain is retained at a level of –0.04. Then, we find that the strain value at the cell boundaries can reach –0.11.

Thus, in this paper, we studied the spectrum of the optical phonons in Ge QD obtained on a Si(111) surface. In the spectra of Raman scattering from optical phonons, we observed a series of lines related to the quantization of the phonon spectrum along the growth direction. It was shown that the phonon mode frequencies are adequately described in terms of the elastic properties and the dispersion of optical phonons of bulk Ge. We also determined the strain in the Ge QD.

This work was supported by the Russian Foundation for Basic Research (project nos. 02-02-17800 and 01-02-16844) and the program of the Ministry of Science, Technology, and Production "Physics of Solid-State Structures" (project no. 2000-3N).

REFERENCES

1. M. Grundman, O. Stier, and D. Bimberg, Phys. Rev. B **52**, 11969 (1995).
2. Y. Kikuchi, H. Sugii, and K. Shintani, J. Appl. Phys. **89**, 1191 (2001).
3. A. V. Nenashev and A. V. Dvurechenskiĭ, Zh. Éksp. Teor. Fiz. **118**, 570 (2000) [JETP **91**, 497 (2000)].
4. N. V. Vostokov, S. A. Gusev, I. V. Dolgov, *et al.*, Fiz. Tekh. Poluprovodn. (St. Petersburg) **34**, 8 (2000) [Semiconductors **34**, 6 (2000)].
5. A. B. Talochkin, V. A. Markov, A. I. Nikiforov, and S. A. Teys, Pis'ma Zh. Éksp. Teor. Fiz. **70**, 279 (1999) [JETP Lett. **70**, 288 (1999)].
6. A. B. Talochkin, S. P. Suprun, A. V. Efanov, *et al.*, Pis'ma Zh. Éksp. Teor. Fiz. **73**, 337 (2001) [JETP Lett. **73**, 297 (2001)].
7. U. Kohler, O. Jusko, G. Pietsch, *et al.*, Surf. Sci. **248**, 321 (1991).
8. B. Voigtlaender, Surf. Sci. Rep. **43**, 127 (2001).
9. K. Takayanagi, Y. Tanishiro, S. Takahashi, and M. Takahashi, Surf. Sci. **164**, 367 (1985).
10. I. I. Novak, V. V. Baptizmanskiĭ, and L. V. Zhoga, Opt. Spektrosk. **43**, 252 (1977) [Opt. Spectrosc. **43**, 145 (1977)].
11. F. Cerdeira, C. J. Buchenauer, F. H. Pollak, and M. Cardona, Phys. Rev. B **5**, 580 (1972).
12. W. Weber, Phys. Rev. B **15**, 4789 (1977).

Translated by E. Golyamina

JETP Letters, Vol. 75, No. 6, 2002, pp. 268–272. Translated from Pis'ma v Zhurnal Éksperimental'noĭ i Teoreticheskoĭ Fiziki, Vol. 75, No. 6, 2002, pp. 318–322.

Observation of Remanent States of Small Magnetic Particles: Micromagnetic Simulation and Experiment

A. M. Alekseev[1], V. A. Bykov[1], A. F. Popkov[1, *], N. I. Polushkin[2], and V. I. Korneev[3]

[1]*State Research Center of Russian Federation–State Research Institute for Problems in Physics, NT MDT, Moscow, 103460 Russia*

[2]*Institute of Microstructure Physics, Russian Academy of Science, Nizhni Novgorod, 603950 Russia*

[3]*Moscow Institute of Electronic Engineering (Technological University), Moscow, 103482 Russia*

**e-mail: popkov@nonlin.msk.ru*

Received February 10, 2002

Abstract—Micromagnetic properties of submicron ferromagnetic elements ellipsoidal in shape are studied theoretically and experimentally. By numerically solving the equations of magnetodynamics, it is found that different remanent magnetization states can be obtained, depending on the manner of magnetization reversal in such elements: one-vortex states, two-vortex states, and vortex-free states with skew-symmetric spin pinning. The magnetization configurations predicted in the calculations have been observed experimentally using magnetic force microscopy in regular lattices of microstructures formed in thin-film samples of Fe–Cr alloys under irradiation by interfering laser beams. © *2002 MAIK "Nauka/Interperiodica".*

PACS numbers: 75.60.Ej; 75.60.Jk; 75.70Ak

1. It is known that nonuniform vortex magnetization configurations arise in small (ferro)magnetic particles with a low magnetic crystalline anisotropy and sizes exceeding the absolute single-domain threshold (~0.05 μ) [1, 2]. The distribution of magnetic moments observed in the remanent state depends essentially on the magnetization prehistory and on the particle shape and size. Recently, new, primarily lithographic technologies have evolved for obtaining thin-film elements with planar sizes down to several tens of nanometers and regular lattices with a given geometry [3, 4]. Progress in the field of nanotechnology has stimulated the study of micromagnetism in small particles based on thin-film magnetic elements (see, for example, [5–8]). These works are devoted to both the occurrence of vortex configurations primarily in elements rectangular in shape and states of a new type, the so-called *C* and *S* configurations, that are characterized by edge spin pinning due to the magnetostatic effect of element edges. The edge pinning effect is manifested in the multimode character of magnetization reversal, which can be the reason for the giant instability of switching fields associated with the thermally activated change of the magnetization reversal near the saturation state [8]. The use of elements with a nonrectangular, in particular, ellipsoidal shape, in which the formation of alternative magnetization configurations associated with spin pinning in the vicinity of narrow poles of the magnetized element is not highly probable, is one of the ways for suppressing this instability. It is these elements that are formed, for example, under the irradiation of a finely dispersed superparamagnetic Fe–Cr medium by interfering laser beams [9]. A regular lattice of ferromagnetic elements is formed at interference maxima as a result of the modification of magnetic properties. The technology of obtaining such a structured medium was described previously in [9]. The goal of this work was (1) to simulate possible remanent magnetization states in submicron elements with an ellipsoidal shape and (2) to compare the results of simulation with experimental data for magnetic lattices obtained in studying thin-film Fe–Cr alloys using a magnetic force microscope (MFM).

2. Magnetization of ellipsoidal particles. The magnetization reversal processes in flat microparticles were analyzed theoretically by numerically integrating the Landau–Lifshitz equations with free boundary conditions. The scheme of numerical integration and examples of modeling rectangular particles were described previously in our works [7, 8, 10]. It was possible to vary the element sizes and the magnetic anisotropy parameters in the calculations. In this work, we will report the results of modeling an elliptic flat element $0.6 \times 0.3 \times 0.015$ μ in size with zero magnetic anisotropy. The magnetic parameters adopted in the calculation, namely, the saturation magnetization $M = 1300$ G and the exchange constant $A = 10^{-6}$ erg/cm^3, corresponded to experimental data for Fe–Cr films.

Modeling the process of magnetization along the long element axis (easy direction of magnetization) showed that the main magnetic hysteresis loop has a rectangular shape for a particle of a specified size and that a uniformly magnetized particle is switched in the field $H_{c1} = 300$ Oe. The magnitude of this field grows as the film thickness and the element aspect ratio increase.

The remanent state corresponds to the complete magnetic polarization of the particle in the easy direction (Fig. 1a).

Magnetization in the transverse direction is of a more complicated character. In this work, we studied the variation of the state of initial magnetization along the long element axis shown in Fig. 1a upon applying a magnetic field along the short axis (hard direction of magnetization). As the magnetic field increases, a smooth rotation of spins occurs at the center of the particle and a skew-symmetric state with spins pinned at the element boundaries is formed (Fig. 1b). The region of nonuniform magnetization variation in the vicinity of pinned regions is narrowed down as the field increases. The calculations demonstrate that the curve of transverse magnetization has a reversible character up to the critical field H_{c2} = 950 Oe and that the initially polarized state is restored as the magnetic field drops to zero. When the critical field H_{c2} is exceeded, the particle transforms into a state saturated in the transverse direction and the initial polarization is not restored. The effect of spin pinning at element boundaries leads to a delay in the transition to the saturated state as compared to the uniform spin rotation model by Stoner and Wohlfarth [11], which takes into account only the effect of film demagnetizing factors. The critical depinning field H_{c2} grows with increasing film thickness more strongly than the critical magnetization reversal field in the transverse direction H_{c1}. The latter depends very strongly on the aspect ratio and sharply increases with decreasing element width.

As the magnetic field decreases from the saturation state of a transversely magnetized particle, a tendency is observed toward a turn of the magnetization at the center of the element, and, as the field becomes zero, a remanent skew-symmetric state is formed that is characterized by the partial magnetic depolarization of the particle along the easy direction (Fig. 1c). As the sign of the magnetic field changes, this state is stable up to the critical field H_{c3} = 50 Oe, above which a transition to the two-vortex state takes place. The center of the particle undergoes backward magnetization reversal, and the effect of edge magnetostatic spin pinning leads to the formation of two oppositely wound magnetic vortices in the vicinity of element poles. When the field returns to zero, this state transforms into a demagnetized remanent state characterized by two magnetic vortices located at the corners of a diamond-shaped domain at the center of the element with magnetization directed across the element (Fig. 1d). If an element resides in a remanent two-vortex state, then, as the magnetic field increases in the transverse direction, the vortices are gradually expelled from the element and it transforms into a state saturated in the transverse direction at fields exceeding the critical saturation field in the transverse direction H_{c4} = 1650 Oe. Before the transition into a state saturated in the transverse direction (in fields $H < H_{c4}$), given field noise fluctuations or field nonuniformity, the element transforms into a close-in-energy, more stable, asymmetric one-vortex state, which transforms into a symmetric demagnetized state with a vortex at the center of the element as the field returns to zero (Fig. 1e). Some of the states described above and shown in Fig. 1 were observed experimentally in MFM images.

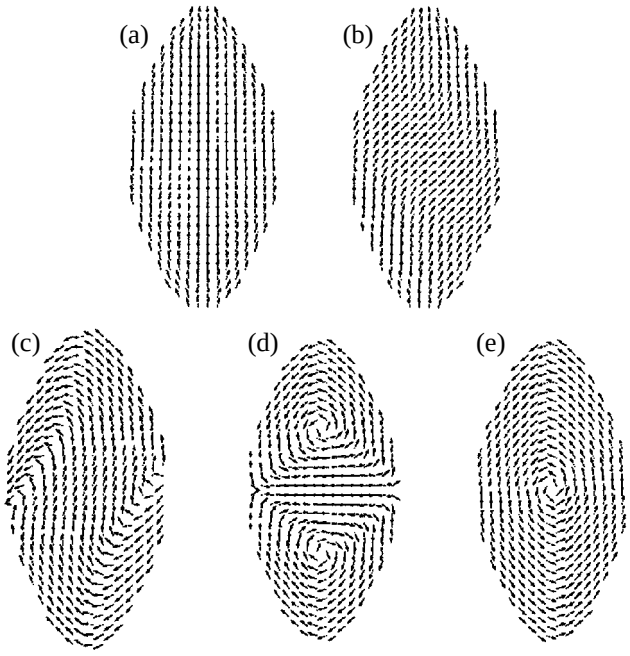

Fig. 1. Calculated magnetic configurations of a Fe–Cr ellipsoidal particle ($0.6 \times 0.3 \times 0.15$ μ) arising in the process of its magnetization in the traverse direction: (a) initial remanent state magnetically polarized along the easy direction, (b) spin pinning state under weak magnetization in the traverse direction for $H < H_{c2}$, (c) remanent state with skew-symmetric spin pinning, (d) two-vortex remanent state, and (e) one-vortex remanent state.

3. Observation of remanent states using MFM. In order to compare the model distributions with the results of visualizing images using an MFM, we calculated these images corresponding to micromagnetic configurations. The simulation was carried out under the assumption that the interaction of the magnetically hard point tip of the force microscope probe with the distributed magnetic subsystem of the flat ultrathin element has a magnetic dipole character. A point magnetic dipole located at height x above the plane of the element creates a magnetic field in its plane

$$\mathbf{H} = \frac{V}{4\pi}\left(\frac{\mathbf{M}_1}{r^3} - \frac{3(\mathbf{M}_1 \cdot \mathbf{r})\mathbf{r}}{r^5}\right), \quad (1)$$

where $\mathbf{M}_1$ is the magnetization of the MFM probe, V is the volume of the magnetic tip, and $r = [(x - x')^2 + (y - y')^2 + z^2]^{1/2}$ is the distance from the tip (above the sighting point (x, y)) to an arbitrary point (x', y') in the plane of the sample $z = 0$. The Zeeman energy of interaction

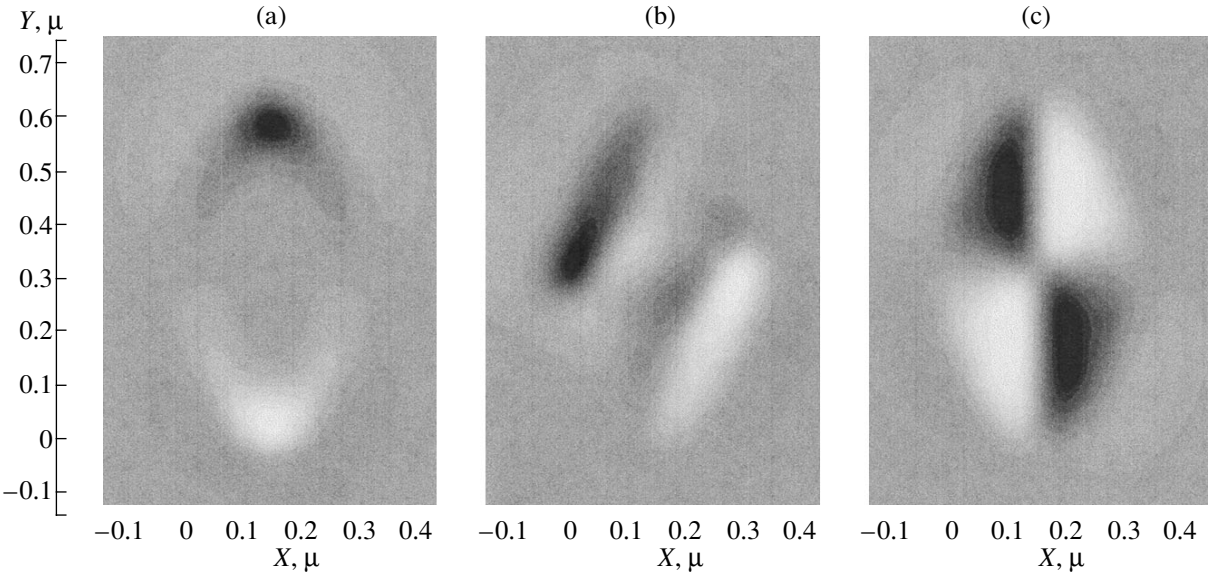

Fig. 2. Calculated MFM images of remanent configurations shown in Fig. 1: (a) magnetically polarized particle, (b) skew-symmetric state with edge spin pinning, an (c) one-vortex demagnetized state.

with a thin magnetic layer of thickness t having the magnetic configuration $\mathbf{M}_2(x', y')$ is given by the convolution $E(x, y) = t\mu_0 \int \mathbf{M}_2(x', y') \cdot \mathbf{H}(x - x'. y - y')dx'dy'$, where integration is carried out over the plane of the sample. The signal of an MFM using resonance oscillations of a cantilever is proportional to the second variation of the Zeeman energy of interaction of the magnetic probe with the field of the sample [12]. Therefore, one can write

$$\Delta\Omega \sim \partial_z^2 E(x, y, z) = t\mu_0 \int_S \mathbf{M}_2(x', y') \cdot \partial_z^2 \mathbf{H}(x - x', y - t')dx'dy', \quad (2)$$

where S is the area of integration.

MFM images obtained in this way at $z = 0.1$ μm are given in Fig. 2 for (a) a uniformly polarized element, (b) a vortex-free state with skew-symmetric spin pinning, and (c) a one-vortex state that correspond to the magnetization configurations depicted in Figs. 1a, 1c, and 1e.

Experimental MFM measurements were performed using a Solver P47 scanning probe microscope (NT MDT, Moscow). Topographies obtained experimentally for ferromagnetic structures formed in a (super)paramagnetic Fe–Cr layer by interfering laser beams and the corresponding MFM images are shown in Fig. 3. Topographic images (a, c, e) demonstrate surface modifications with an elliptic shape. These modifications correspond to pronounced MFM contrast (b, d, f). A uniformly polarized remanent state obtained by saturating an element along the easy axis in a field of 500 Oe is shown in Fig. 3b. A vortex-free state with skew-symmetric spin pinning was obtained experimentally by the magnetization reversal of elements along their short axis in a field of 1000 Oe (Fig. 3d). It is also interesting to mention the possibility of obtaining a one-vortex remanent state (Fig. 3f) upon magnetization reversal in the transverse direction in a field of 750 Oe. Thus, the experimental data are in good agreement with the results of micromagnetic modeling.

4. Thus, micromagnetic modeling showed that a particle magnetized along the easy axis, having undergone transverse magnetization, retains the remanent state determined by the effect of skew-symmetric boundary spin pinning up to the critical field above which the irreversible transition to the saturation state takes place. This field essentially exceeds the switching field in the longitudinal direction. Both critical fields decrease with decreasing film thickness.

After saturation in the transverse direction, the particle does not return to the complete polarization state. In this case, two types of remanent states are possible. One of them is characterized by a spin distribution with skew-symmetric pinning at the element boundaries, and the other one corresponds to the complete demagnetization of the particle and contains either two magnetic vortices at the boundaries of the diamond-shaped magnetostatic domain inside the particle or one vortex at its center. This last-mentioned effect is in agreement with the calculations reported in [1] for a flat rectangular Permalloy particle with a large aspect ratio. It was shown in [1] that a long rectangular particle after saturation in the transverse direction is subdivided into a number of oppositely wound magnetic vortices. The application of a magnetic field leads to the gradual displacement of vortices to the element boundaries and to their disappearance at the transition to the saturated

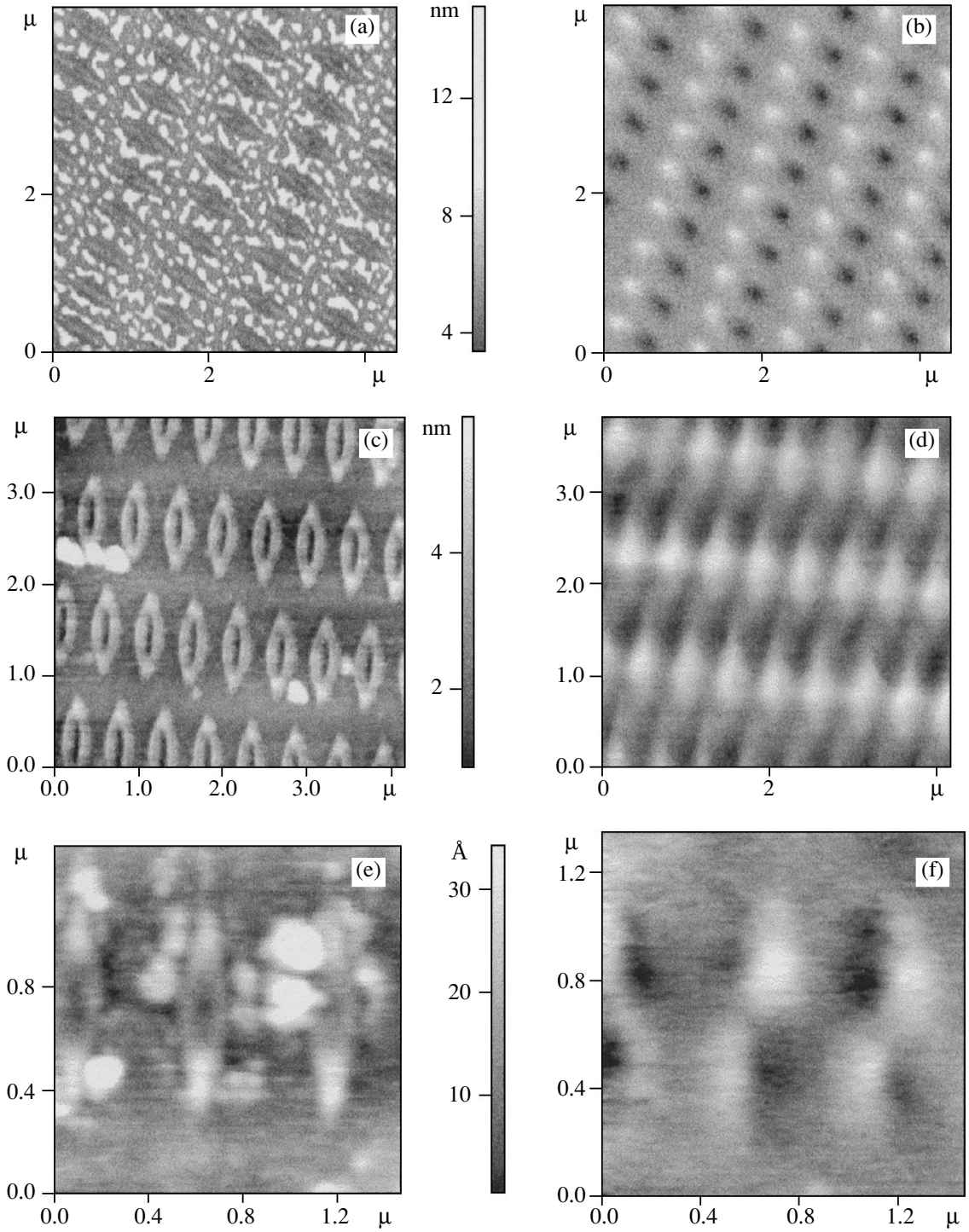

Fig. 3. Atomic force–magnetic force images of modified regions of Fe–Cr films obtained by interference laser sintering; (a), (c), and (e): topography of regions annealed at the irradiation intensity $J = 0.3$ W/cm^2; (b), (d), and (f): corresponding images of particles. The height of image pickup in the resonance mode $z = 0.05$ μ.

state. The effect of restoring the initial state depends on the direction of the magnetization field. As the particle sizes decrease, the effect of edge spin pinning will be suppressed by exchange interaction and the behavior of the particle will approach the single-domain behavior. The character of magnetization reversal in this case will approach that predicted by the Stoner–Wohlfarth model.

The main features of magnetization reversal obtained by micromagnetic simulation are in agreement with the results of MFM observations. Thus, stability was observed with respect to the action of the

transverse magnetic field of smaller particles, and completely demagnetized particles appeared upon reverse transverse magnetization after threshold saturation in the transverse direction. However, the theoretical model ignored the particular features of samples taken for the experimental investigations of magnetization reversal processes and remanent states, namely, the effect of the superparamagnetic phase in the film surrounding ferromagnetic particles and the formation of crystalline microinclusions under high intensity of laser annealing. The superparamagnetic medium can serve as a magnetic conductor for the magnetic flux created by polarized magnetic particles, which may lead to an additional magnetostatic interaction of particles changing their switching fields. Taking into account the last-mentioned mechanism of the effect of the nanoparticle lattice on magnetization calls for further investigation.

This work was supported by the Russian Foundation for Basic Research, project nos. 02-02-16704 and 01-02-16445; the International Science and Technology Center, project no. 1522; and INTAS, project no. 99-01839.

REFERENCES

1. D. R. Fredkin, T. R. Koehler, J. F. Smyth, and S. Schultz, J. Appl. Phys. **69**, 5276 (1991).
2. R. Hertel and H. Kronmuller, Phys. Rev. B **60**, 7366 (1999).
3. S. Y. Chou, Proc. IEEE **85**, 652 (1997).
4. T. A. Savas, M. Farhoud, and H. I. Smith, J. Appl. Phys. **85**, 6160 (1999).
5. J.-G. Zhu and H. N. Bertram, IEEE Trans. Magn. **27**, 3553 (1991).
6. J.-L. Berchier, K. Solt, and T. Zajk, J. Appl. Phys. **55**, 487 (1984).
7. A. F. Popkov, L. L. Savchenko, N. V. Vorotnikova, *et al.*, Appl. Phys. Lett. **77**, 277 (2000).
8. A. F. Popkov, L. L. Savchenko, and N. V. Vorotnikova, Pis'ma Zh. Éksp. Teor. Fiz. **69**, 555 (1999) [JETP Lett. **69**, 596 (1999)].
9. A. M. Alekseev, Yu. K. Verevkin, N. V. Vostokov, *et al.*, Pis'ma Zh. Éksp. Teor. Fiz. **73**, 214 (2001) [JETP Lett. **73**, 192 (2001)].
10. A. F. Popkov, N. V. Vorotnikova, and A. Yu. Polozov, Mat. Model. **11**, 54 (1999).
11. E. C. Stoner and E. P. Wohlfarth, Philos. Trans. R. Soc. London, Ser. A **240**, 599 (1948).
12. P. Guethner, H. Mamin, and D. Rugar, in *Scanning Tunneling Microscopy II*, Ed. by R. Wiesendander and H.-J. Gunherodt (Springer-Verlag, Berlin, 1992), p. 151.

Translated by A. Bagatur'yants

JETP Letters, Vol. 75, No. 6, 2002, pp. 273–277. From Pis'ma v Zhurnal Éksperimental'noĭ i Teoreticheskoĭ Fiziki, Vol. 75, No. 6, 2002, pp. 323–327.

Low-Temperature Effective Electromagnetism in Superfluid ^{3}He-A[1]

J. Dziarmaga

Los Alamos National Laboratory, Theory Division T-6, Los Alamos, New Mexico 87545 USA
Instytut Fizyki Uniwersytetu Jagiellońskiego, 30-059 Kraków, Poland

Received February 18, 2002

Abstract—A general low-temperature effective action for the order parameter in the superfluid phase A of helium 3 is derived. In a symmetric case, when the Fermi velocity equals the transverse velocity of low energy fermionic quasiparticles, the action is the standard relativistic electromagnetic action. © *2002 MAIK "Nauka/Interperiodica".*

PACS numbers: 67.57.-z; 11.15.-q, 11.90.+t

1. INTRODUCTION

Quantum mechanics is not compatible with general relativity. There are well-known problems with definition of a time operator, the cosmological constant problem, the divergencies in the relativistic quantum field theory, and the black hole paradoxes [1]. In recent years, as a result of interaction between the condensed matter and the high-energy physics communities, a new program is emerging that may solve all these fundamental problems at once [2–5]. The key idea is that both general relativity and the Standard Model [2–5] are low-energy effective field theories of an underlying condensed matter system.

By its very definition, this program invalidates the time operator problem. The fundamental theory is a condensed matter system described by a "nonrelativistic" N-body Schrödinger equation in an abstract configuration space. The time operator problem is an artifact of the effective low-energy relativistic theory. When the missing definition of a time operator leads to paradoxes in the effective theory, their resolution can be found at the level of the fundamental condensed matter system.

The cosmological constant or Casimir energy, when calculated within the effective relativistic quantum field theory, is divergent. It is customary to cut off this divergence at the Planck scale. Even with the cutoff, the cosmological constant is still, by many orders of magnitude, inconsistent with observations. A fundamental condensed matter theory should, at the very least, provide a correct prescription as to how to make the cutoff in the effective relativistic theory [3]. An example in [3] demonstrates that, in a condensed matter system, it is even possible to have a nonzero Casimir force but at the same time as an exactly vanishing cosmological constant.

The divergences in the perturbative relativistic quantum field theory are yet another artifact of the effective low-energy theory. The underlying N-body Schrödinger equation does not suffer from any divergencies.

Violation of relativity at high energies or strong fields, where the "nonrelativistic" nature of the fundamental theory shows up, allows the high-energy particles to communicate over a black hole event horizon, and in this way it solves the paradoxes related to the horizon [4].

The idea that relativistic fields are low-energy excitations of a condensed matter system is older than the relativistic field theory. Maxwell derived his famous equations as a hydrodynamic description of a hypothetical ether. Later on, the Michelson–Morley experiment proved that there is no detectable motion of the Earth with respect to the ether. The fundamental condensed matter system is an ether but in a modern guise. There is an essential difference with respect to the traditional ether: now everything, i.e., both light and fermionic matter (including the famous Michelson and Morley's experimental setup), is effective low-energy bosonic and fermionic relativistic excitations. The low-energy relativistic excitations cannot detect their motion with respect to the modern ether and there are no fundamental relativistic fields, otherwise we would have to deal again with the time operator and the cosmological constant problem. The condition that the low-energy excitations must include relativistic fermionic quasiparticles strongly suggests that the underlying condensed matter system must contain fundamental "nonrelativistic" fermions.

Analogies between the black hole horizon and sonic horizons in a number of condensed matter systems were explored in [6]. Analogies between *fermionic* helium 3 and the standard model, as well as general relativity, were explored in depth in [2]. See [7] for yet

[1] This article was submitted by the author in English.

another example of a fermionic system with effective gauge and gravity fields. Of particular interest in the present context is two phases of the superfluid helium 3: the A phase and the planar phase [2]. In a conventional superconductor and in the *B* phase of helium 3 there is an energy gap Δ_0 between the Landau quasiparticles below the Fermi surface, where $p = p_F$, and those above the Fermi surface. In the A phase and the planar phase, this gap has two nodes at the so-called Fermi points on the Fermi surface. The order parameter includes a unit vector $\hat{\mathbf{l}}$ related to the orbital angular momentum of the atoms. The two Fermi points are located at $\mathbf{p} = \pm p_F\hat{\mathbf{l}}$. Close to the Fermi point, say, $\mathbf{p} = p_F\hat{\mathbf{l}}$, the energy $e_{\mathbf{p}}$ of the fermionic Landau quasiparticles can be approximated by

$$e_{\mathbf{p}}^2 + g^{ab}(p_a - p_F l_a)(p_b - p_F l_b) \approx 0, \tag{1}$$

where the indices a, b run over 1, 2, 3 (or x, y, z). This spectrum is relativistic; there are low-energy effective Dirac fermions in this system.

In general, the metric tensor depends on $\hat{\mathbf{l}}$,

$$g^{00} = 1, \quad -g^{ab} = c_F^2 l^a l^b + c_\perp^2(\delta^{ab} - l^a l^b), \tag{2}$$

where c_F is an effective Fermi velocity and $c_\perp = \Delta_0/p_F$ is a transverse velocity of the fermionic quasiparticles near a Fermi point. However, in a *symmetric* case, when

$$c_\perp = c_F, \tag{3}$$

the metric tensor becomes independent of $\hat{\mathbf{l}}$,

$$g^{\mu\nu} = \mathrm{diag}\{1, -c_F^2, -c_F^2, -c_F^2\}. \tag{4}$$

As noted in [2], the p_F in Eq. (1) can be interpreted as an electromagnetic vector potential and integration over the relativistic fermions should give an effective electromagnetic action for these gauge fields. This integration over an equilibrium low-temperature ensemble of fermions is the subject of the next section. This derivation shows how an effective relativistic electrodynamics emerges from an underlying fermionic condensed matter system.

The derivation in the next section generalizes the classic helium 3 results for $c_F \gg c_\perp$ obtained by Cross in [8]. The symmetric case $c_F = c_\perp$ is far from the real helium 3. However, it should be possible to construct an abstract symmetrized helium 3 with interactions tuned so as to have a stable phase A and $c_F = c_\perp$ at the same time. The fundamental condensed matter system does not need to be constrained by the generic properties of interactions in the electronic or atomic condensed matter systems. The aim of this paper is to better substantiate the idea [2] that the *relativistic* electrodynamics can be an effective low-energy theory in a "*nonrelativistic*" fermionic condensed matter system.

2. THE EFFECTIVE ELECTROMAGNETISM

2.1. Bogolubov–Nambu Space

To describe helium 3, it is convenient to combine spin-up and spin-down fermions into a Bogolubov–Nambu spinor

$$\chi(\mathbf{x}) = \begin{pmatrix} \psi_\uparrow(\mathbf{x}) \\ \psi_\downarrow(\mathbf{x}) \\ \psi_\downarrow^\dagger(\mathbf{x}) \\ -\psi_\uparrow^\dagger(\mathbf{x}) \end{pmatrix}. \tag{5}$$

It is understood here that $\mathbf{p} = -i\nabla$ and the nabla is applied to the $\chi(\mathbf{x})$ on the right. A mean-field Hamiltonian that describes interaction of the fermionic atoms with the order parameters in the phase A of ^{3}He is given by

$$H = \frac{1}{2}\int d^3x \chi^\dagger(\mathbf{x}) \begin{pmatrix} +\epsilon_{\mathbf{p}} & \Delta_0^* \sigma \dfrac{p_\perp^*}{p_F} \\ \Delta_0 \sigma \dfrac{p_\perp}{p_F} & -\epsilon_{\mathbf{p}} \end{pmatrix} \chi(\mathbf{x}). \tag{6}$$

Here, $\Delta_0(\mathbf{x})$ is the energy gap and p_F is the Fermi momentum. $\epsilon(\mathbf{p})$ is the quasiparticle energy, which can be approximated close to the Fermi surface by

$$\begin{aligned} \epsilon_{\mathbf{p}} &\approx \frac{p^2}{2m_*} - \frac{p_F^2}{2m_*} \\ &= \frac{(p + p_F)(p - p_F)}{2m_*} \approx c_F(p - p_F), \end{aligned} \tag{7}$$

where $c_F = p_F/m_*$ is the Fermi velocity and m_* is the effective mass of Landau quasiparticles close to the Fermi surface.

$$\sigma(\mathbf{x}) \equiv d^\mu(\mathbf{x})\sigma_\mu, \tag{8}$$

with $d^\mu d^\mu = 1$ being a 2×2 spin matrix.

$$p_\perp(\mathbf{x}) \equiv \frac{1}{2}\{e_1^a(\mathbf{x}) + ie_2^a(\mathbf{x}), p^a\}, \tag{9}$$

where summation runs over $a = 1, 2, 3$, and $\hat{\mathbf{e}}_1$ and $\hat{\mathbf{e}}_2$ satisfy

$$\begin{aligned} &\hat{\mathbf{e}}_1\hat{\mathbf{e}}_1 = 1, \quad \hat{\mathbf{e}}_2\hat{\mathbf{e}}_2 = 1, \\ &\hat{\mathbf{e}}_1\hat{\mathbf{e}}_2 = 0, \quad \hat{\mathbf{l}} = \hat{\mathbf{e}}_1 \times \hat{\mathbf{e}}_2. \end{aligned} \tag{10}$$

2.2. Background Order Parameter

We will derive the effective action for small fluctuations of the order parameter around the equilibrium order parameter

$$\Delta_0(\mathbf{x}) = \Delta_0 \in \mathcal{R}, \quad \sigma(\mathbf{x}) = \sigma_3, \tag{11}$$

$$\hat{\mathbf{e}}_1(\mathbf{x}) = \hat{\mathbf{e}}_x, \quad \hat{\mathbf{e}}_2(\mathbf{x}) = \hat{\mathbf{e}}_y, \quad \hat{\mathbf{l}}(\mathbf{x}) = \hat{\mathbf{e}}_x \times \hat{\mathbf{e}}_y = \hat{\mathbf{e}}_z, \tag{12}$$

$$p_\perp = p_x + ip_y. \tag{13}$$

With this background, the Hamiltonian (6) becomes

$$H_0 = \frac{1}{2}\int d^3x \chi^\dagger(\mathbf{x}) \begin{pmatrix} +\epsilon_\mathbf{p} & \Delta_0\sigma_3\dfrac{p_\perp^*}{p_F} \\ \Delta_0\sigma_3\dfrac{p_\perp}{p_F} & -\epsilon_\mathbf{p} \end{pmatrix} \chi(\mathbf{x}). \tag{14}$$

2.3. Bogolubov Transformation

The Hamiltonian (14) is diagonalized by a Bogolubov transformation

$$\psi_\uparrow(\mathbf{p}) = u_\mathbf{p}\gamma_\uparrow(\mathbf{p}) + v_\mathbf{p}\gamma_\downarrow^\dagger(-\mathbf{p}), \tag{15}$$

$$\psi_\downarrow(\mathbf{p}) = u_\mathbf{p}\gamma_\downarrow(\mathbf{p}) + v_\mathbf{p}\gamma_\uparrow^\dagger(-\mathbf{p}), \tag{16}$$

where the Bogolubov coefficients $u_\mathbf{p}$ and $v_\mathbf{p}$ satisfy

$$|u_\mathbf{p}|^2 = \frac{1}{2}\left(1 + \frac{\epsilon_\mathbf{p}}{e_\mathbf{p}}\right), \quad |v_\mathbf{p}|^2 = \frac{1}{2}\left(1 - \frac{\epsilon_\mathbf{p}}{e_\mathbf{p}}\right), \tag{17}$$

$$2u_\mathbf{p}v_\mathbf{p} = \frac{c_\perp p_\perp}{e_\mathbf{p}}, \quad e_\mathbf{p} = (\epsilon_\mathbf{p}^2 + c_\perp^2|p_\perp|^2)^{1/2}. \tag{18}$$

Here, we define $c_\perp \equiv \Delta_0/p_F$. The diagonalized Hamiltonian (14) is

$$H_0 = \int d^3p e_\mathbf{p}[\gamma_\uparrow^\dagger(\mathbf{p})\gamma_\uparrow(\mathbf{p}) + \gamma_\downarrow^\dagger(\mathbf{p})\gamma_\downarrow(\mathbf{p})]. \tag{19}$$

Close to the Fermi point at $\mathbf{p} = \pm p_F\hat{\mathbf{l}}$ the squared energy of the quasiparticles can be approximated by Eq. (1) [compare with Eqs. (7) and (18)], and g^{ab} is the spatial part of a metric tensor

$$g^{\mu\nu} = \mathrm{diag}\{1, -c_\perp^2, -c_\perp^2, -c_F^2\}. \tag{20}$$

2.4. Small Fluctuations of $\hat{\mathbf{l}}$

We add small perturbations to the background field (11), (12)

$$\hat{\mathbf{e}}_1(\mathbf{x}) = \hat{\mathbf{e}}_x + \mathbf{n}_1(\mathbf{x}), \quad \hat{\mathbf{e}}_2(\mathbf{x}) = \hat{\mathbf{e}}_y + \mathbf{n}_2(\mathbf{x}) \tag{21}$$

and define a small complex vector field

$$z_a(\mathbf{x}) \equiv n_1^a(\mathbf{x}) + in_2^a(\mathbf{x}). \tag{22}$$

The Hamiltonian (6) becomes $H = H_0 + H_1 + \mathbb{O}(z^2)$, where

$$H_1 = \int d^3p[z_a^*(\mathbf{p})F_\mathbf{p}^a + \mathrm{h.c.}] \tag{23}$$

is an interaction Hamiltonian linear in z_a. Here, we use the Fourier transform

$$z_a(\mathbf{p}) = \int \frac{d^3x}{(2\pi)^3} e^{-i\mathbf{x}\mathbf{p}} z_a(\mathbf{x}) \tag{24}$$

and the operator

$$\begin{aligned} F_\mathbf{p}^a[\gamma] \equiv -\Delta_0 \int d^3k \frac{k^a}{p_F} \\ \times \Big[u_{\frac{\mathbf{p}}{2}+\mathbf{k}} u_{\frac{\mathbf{p}}{2}-\mathbf{k}} \gamma_\downarrow\Big(\frac{\mathbf{p}}{2}+\mathbf{k}\Big)\gamma_\uparrow\Big(\frac{\mathbf{p}}{2}-\mathbf{k}\Big) \\ + v_{\frac{\mathbf{p}}{2}+\mathbf{k}} v_{\frac{\mathbf{p}}{2}-\mathbf{k}} \gamma_\uparrow^\dagger\Big(-\frac{\mathbf{p}}{2}+\mathbf{k}\Big)\gamma_\uparrow\Big(-\frac{\mathbf{p}}{2}+\mathbf{k}\Big) \\ + u_{\frac{\mathbf{p}}{2}+\mathbf{k}} v_{\frac{\mathbf{p}}{2}-\mathbf{k}} \gamma_\downarrow\Big(\frac{\mathbf{p}}{2}+\mathbf{k}\Big)\gamma_\downarrow^\dagger\Big(-\frac{\mathbf{p}}{2}+\mathbf{k}\Big) \\ + u_{\frac{\mathbf{p}}{2}-\mathbf{k}} v_{\frac{\mathbf{p}}{2}+\mathbf{k}} \gamma_\uparrow^\dagger\Big(-\frac{\mathbf{p}}{2}-\mathbf{k}\Big)\gamma_\uparrow\Big(\frac{\mathbf{p}}{2}-\mathbf{k}\Big) \Big]. \end{aligned} \tag{25}$$

2.5. Second-Order Effective Action

A real (unitary) part of the second-order effective action is

$$\begin{aligned} S^{(2)}[z] \\ = \mathrm{Re}\frac{i}{2}\int dt\,dt' \langle \hat{T} H_1[\gamma_+(t)] H_1[\gamma_+(t')] \rangle \\ = \mathrm{Re}\frac{i}{2}\int dt\,dt' \int d^3p\,d^3p' \\ \times [2z_a(t,\mathbf{p})\langle \hat{T} F_\mathbf{p}^{\dagger a}[\gamma_+(t)] F_{\mathbf{p}'}^b[\gamma_+(t')]\rangle z_b^*(t',\mathbf{p}') \\ + (z_a^*(t,\mathbf{p}')\langle \hat{T} F_\mathbf{p}^a[\gamma_+(t)] F_{\mathbf{p}'}^b[\gamma_+(t')]\rangle \\ \times z_b^*(t',\mathbf{p}') + \mathrm{c.c.})], \end{aligned} \tag{26}$$

where $\hat{T}$ denotes time ordering along the Keldysh contour. The interaction picture $\gamma_+(t)$' sits on the positive (forward in time) branch of the contour. A straightforward but somewhat tedious calculation, which uses correlator time ordered along the contour

$$\begin{aligned} \langle \hat{T}[\gamma_+(t,\mathbf{k})\gamma_+^\dagger(t',\mathbf{k}')]\rangle = \delta(\mathbf{k}-\mathbf{k}')e^{-ie_\mathbf{k}(t-t')} \\ \times [\theta(t-t')f(-\beta e_\mathbf{k}) - \theta(t'-t)f(+\beta e_\mathbf{k})], \end{aligned} \tag{27}$$

with $f(x) = (1 + e^x)^{-1}$ and β an inverse temperature, gives the effective action

$$S^{(2)}[z] = \int d\omega \int d^3p \times [z_a(\omega, \mathbf{p}) G_1^{ab}(\omega, \mathbf{p}) z_b^*(\omega, \mathbf{p}) + (z_a^*(\omega, \mathbf{p}') G_2^{ab}(\omega, \mathbf{p}) z_b^*(-\omega, -\mathbf{p}) + \text{c.c.})]. \quad (28)$$

The kernels are given by

$$G_1^{ab}(\omega, \mathbf{p}) = 2\pi\Delta_0^2 \text{P.V.} \int d^3k \frac{k^a k^b}{p_F^2} \frac{2\sinh(\beta e_{\mathbf{k}})}{1 + \cosh(\beta e_{\mathbf{k}})} \times \left[\frac{\left|u_{\mathbf{k}+\frac{\mathbf{p}}{2}}\right|^2 \left|u_{\mathbf{k}-\frac{\mathbf{p}}{2}}\right|^2}{+\omega + e_{\mathbf{k}+\frac{\mathbf{p}}{2}} + e_{\mathbf{k}-\frac{\mathbf{p}}{2}}} + \frac{\left|v_{\mathbf{k}+\frac{\mathbf{p}}{2}}\right|^2 \left|v_{\mathbf{k}-\frac{\mathbf{p}}{2}}\right|^2}{-\omega + e_{\mathbf{k}+\frac{\mathbf{p}}{2}} + e_{\mathbf{k}-\frac{\mathbf{p}}{2}}} \right] \quad (29)$$

and

$$G_2^{ab}(\omega, \mathbf{p}) = -\pi\Delta_0^2 \text{P.V.} \int d^3k \frac{k^a k^b}{p_F^2} \times \frac{2\sinh(\beta e_{\mathbf{k}})}{1 + \cosh(\beta e_{\mathbf{k}})} \left(u_{\mathbf{k}+\frac{\mathbf{p}}{2}} v_{\mathbf{k}+\frac{\mathbf{p}}{2}}\right) \left(u_{\mathbf{k}-\frac{\mathbf{p}}{2}} v_{\mathbf{k}-\frac{\mathbf{p}}{2}}\right) \quad (30)$$

$$\times \left[\frac{1}{+\omega + e_{\mathbf{k}+\frac{\mathbf{p}}{2}} + e_{\mathbf{k}-\frac{\mathbf{p}}{2}}} + \frac{1}{-\omega + e_{\mathbf{k}+\frac{\mathbf{p}}{2}} + e_{\mathbf{k}-\frac{\mathbf{p}}{2}}} \right].$$

Here, we neglect terms that are exponentially small for small temperature. In order to attain a low-energy effective theory, these kernels will be (gradient) expanded in powers of ω and $\mathbf{p}$.

2.6. Gradient Expansion of G^{33}

A gradient expansion of G^{33} gives terms which are logarithmically divergent when $\beta \longrightarrow \infty$. This divergence, localized at the Fermi points $\mathbf{k} = \pm p_F \hat{\mathbf{l}}$, can be identified as

$$G_{1,\,\text{Log}}^{33}(\omega, \mathbf{p}) = \frac{4\pi^2\Delta_0^2}{3} \left[\omega^2 - \frac{1}{2} c_\perp^2 (p_x^2 + p_y^2) - c_F^2 (p_z^2) \right] \ln(\beta\Delta_0) \quad (31)$$

and

$$G_{2,\,\text{Log}}^{33}(\omega, \mathbf{p}) = \frac{\pi^2\Delta_0^2}{3} [c_\perp^2 p_\perp^2] \ln(\beta\Delta_0). \quad (32)$$

After the inverse Fourier transform, we obtain the logarithmically divergent part of the second-order effective action

$$S_{\text{Log}}^{(2)}[\mathbf{n}] = \frac{p_F^2 \ln\left(\frac{\Delta_0^2}{T^2}\right)}{24\pi^2 c_F} \int d^4x \times \left\{ \sum_{k=1,2} \left[\left(\frac{\partial n_k^3}{\partial t}\right)^2 - c_F^2 \left(\frac{\partial n_k^3}{\partial z}\right)^2 \right]^2 - c_\perp^2 [\partial_x n_2^3 - \partial_y n_2^3]^2 \right\}. \quad (33)$$

This action is a second-order perturbative version of the action

$$S_{\text{Log}}^{(2)}[\mathbf{l}] = \frac{p_F^2 \ln\left(\frac{\Delta_0^2}{T^2}\right)}{24\pi^2 c_F} \int d^4x \times \left\{ \left[\frac{\partial \mathbf{l}}{\partial t}\right]^2 - c_F^2 [\mathbf{l} \times (\nabla \times \mathbf{l})]^2 - c_\perp^2 [\mathbf{l}(\nabla \times \mathbf{l})]^2 \right\}. \quad (34)$$

Fluctuations of $\hat{\mathbf{l}}$ are not the only contribution to the logarithmically divergent part of the low-energy effective action. Another contribution comes from the component of the superfluid velocity $\mathbf{v}$, which is parallel to $\hat{\mathbf{l}}$.

2.7. Small Fluctuations of ($\hat{\mathbf{l}}\,\mathbf{v}$)

For a *uniform* stationary superfluid flow with velocity $\mathbf{v}$ and close to the Fermi surface, $p \approx p_F$, the Hamiltonian (14) becomes

$$H_0 = \frac{1}{2} \int d^3x \chi^\dagger(\mathbf{x}) \times \begin{pmatrix} +\epsilon_{\mathbf{p}+m_*\mathbf{v}} + \frac{1}{2} m_* v^2 & \Delta_0 \sigma_3 \frac{(p_\perp^* + m_* v_\perp^*)}{p_F} \\ \Delta_0 \sigma_3 \frac{(p_\perp - m_* v_\perp)}{p_F} & -\epsilon_{\mathbf{p}-m_*\mathbf{v}} - \frac{1}{2} m_* v^2 \end{pmatrix} \chi(\mathbf{x}); \quad (35)$$

compare with Eqs. (6), (7) and use a Galilean transformation. Here, $v_\perp \equiv v_x + i v_y$. We are interested in the part of the Hamiltonian (35) linear in $\mathbf{v}$, and we expand

$$\epsilon_{\mathbf{p}+m_*\mathbf{v}} = \epsilon_{\mathbf{p}} + \mathbf{p}\mathbf{v} + \mathbb{O}(v^2). \quad (36)$$

So far, $\mathbf{v}$ was constant. Now we make it space- and time-dependent, $\mathbf{v} = \mathbf{v}(t, \mathbf{x})$, and, at the same time, to keep the Hamiltonian (35) Hermitian, we make in Eq. (36) a replacement

$$\mathbf{p}\mathbf{v} \longrightarrow \frac{1}{2}\{\mathbf{p}, \mathbf{v}(t, \mathbf{x})\} = \frac{1}{2}[\mathbf{p}\mathbf{v}(t, \mathbf{x})] + \mathbf{v}(t, \mathbf{x})\mathbf{p}. \quad (37)$$

We expand the Hamiltonian (35) to the leading order in $\mathbf{v}$ using Eq. (36) and the replacement (37). In the expanded Hamiltonian, we keep only the terms where the operator $\mathbf{p}$ is applied to χ or $\chi^\dagger$. As the main contribution to the logarithmically divergent part of the effective action comes from near the Fermi points at $\mathbf{p} = \pm p_F \hat{\mathbf{l}}$, these terms are formally on the order of p_F. They are large compared to terms where the operator $\mathbf{p}$ is applied to the slowly varying velocity field $\mathbf{v}$. After these last terms are neglected, the interaction Hamiltonian becomes

$$H_1 \approx \frac{1}{2}\int d^3x \chi^\dagger(\mathbf{x})[v^a(\mathbf{x})p_a]\chi(\mathbf{x}). \quad (38)$$

This Hamiltonian is Hermitian when we take into account that $p_a\mathbf{v}(\mathbf{x})$ is negligible compared to $p_a\chi^{(\dagger)}$. With the definition (5) and the Bogolubov transformation (16), the Hamiltonian becomes

$$H_1 \approx \int d^3p[v_a^*(\mathbf{p})f_{\mathbf{p}}^a + \text{h.c.}], \quad (39)$$

where

$$f_{\mathbf{p}}^a \equiv \int d^3k k_a \times\left(u_{\mathbf{k}+\frac{\mathbf{p}}{2}}v^*_{\mathbf{k}-\frac{\mathbf{p}}{2}} - u_{\mathbf{k}-\frac{\mathbf{p}}{2}}v^*_{\mathbf{k}+\frac{\mathbf{p}}{2}}\right)\gamma_\downarrow(-\mathbf{k})\gamma_\uparrow(+\mathbf{k}). \quad (40)$$

Here, we neglect all mixed terms of the form $\gamma^\dagger\gamma$ which for small T give an exponentially small contribution to the effective action. The effective action is given by

$$S^{(2)}_{\text{Log}}[\mathbf{v}] \approx \text{Re}\frac{i}{2}\int dt dt' \int d^3p d^3p' \times 2v_a(t,\mathbf{p})\langle \hat{T} f^{\dagger a}_{\mathbf{p}}[\gamma_+(t)] f^b_{\mathbf{p}'}[\gamma_+(t')]\rangle v^*_b(t',\mathbf{p}'); \quad (41)$$

compare to Eq. (26). A straightforward calculation similar to the derivation of the effective action for small fluctuations of $\hat{\mathbf{l}}$ gives

$$S^{(2)}_{\text{Log}}(\mathbf{v}) = \frac{p_F^2 \ln(\Delta_0^2/T^2)}{24\pi^2}\int \sqrt{-g}d^4x(-g^{ab}\partial_a v_3 \partial_b v_3). \quad (42)$$

The logarithmically divergent part of the effective action (42) contains only v_3, because at the Fermi points it is only v_3 that couples to $\mathbf{p} = \pm p_F\hat{\mathbf{l}} = \pm p_F\hat{\mathbf{e}}_z$; compare with Eq. (38).

2.8. The Electromagnetic Effective Action

After identifications

$$A_0 = p_F(\mathbf{lv}), \quad \mathbf{A} = p_F\hat{\mathbf{l}}, \quad (43)$$

the sum of the two actions (34), (42) becomes

$$S^{(2)}_{\text{Log}} = \frac{\ln(\Delta_0^2/T^2)}{12\pi^2}\int \sqrt{-g}d^4x\left(-\frac{1}{4}F^{\mu\nu}F_{\mu\nu}\right), \quad (44)$$

where $F_{\mu\nu} = \partial_\mu A_\nu - \partial_\nu A_\mu$ and $g^{\mu\nu}$ is given by Eq. (20).

In the symmetric case, the metric tensor (4) does not depend on $\hat{\mathbf{l}}$. A_μ uncouples from the metric tensor and becomes an independent electromagnetic field.

3. CONCLUSION

The effective action (44) and the identifications (43) agree with the effective action and the identifications that were suggested in [2].

The effective action (44) is the generalization of the classic results of Cross [8] to arbitrary $c_F/c_\perp$. This generalization makes manifest the relativistic invariance present in the effective action.

I thank Grisha Volovik for his contribution to this work; Pawel Mazur for his informal one-audience lectures; and Diego Dalvit for his comments on an earlier draft of this manuscript.

REFERENCES

1. S. W. Hawking, Nature **248**, 30 (1974); S. W. Hawking, Phys. Rev. D **13**, 191 (1976).
2. G. E. Volovik, Phys. Rep. **351**, 195 (2001).
3. G. E. Volovik, J. Low Temp. Phys. **124**, 25 (2001).
4. U. R. Fisher and G. E. Volovik, Int. J. Mod. Phys. D **10**, 57 (2001); R. Laughlin and D. Pines, Proc. Natl. Acad. Sci. USA **97**, 28 (2000); P. O. Mazur and E. Mottola, gr-qc/0109035, Phys. Rev. Lett. (in press); P. Huhtala and G. E. Volovik, gr-qc/0111055.
5. A. Sakharov, Dokl. Akad. Nauk SSSR **177**, 70 (1967) [Sov. Phys. Dokl. **12**, 1040 (1968)].
6. W. G. Unruh, Phys. Rev. Lett. **46**, 1351 (1981); Phys. Rev. D **51**, 2827 (1995); T. Jacobson and G. E. Volovik, Phys. Rev. D **58**, 064021 (1998); L. J. Garay *et al.*, Phys. Rev. Lett. **85**, 4643 (2000); Phys. Rev. A **63**, 023611 (2001); M. Mohazzab, J. Low Temp. Phys. **121**, 659 (2000); G. Chapline, E. Hohlfield, R. B. Laughlin, and D. I. Santiago, Philos. Mag. B **81**, 235 (2001); U. Leonhardt, Nature **415**, 406 (2002).
7. S. C. Zhang and J. Hu, Science **294**, 823 (2001).
8. M. C. Cross, J. Low Temp. Phys. **21**, 525 (1975).

JETP Letters, Vol. 75, No. 6, 2002, pp. 278–281. Translated from Pis'ma v Zhurnal Éksperimental'noĭ i Teoreticheskoĭ Fiziki, Vol. 75, No. 6, 2002, pp. 328–330.

Induced Unidirectional Anisotropy and Biperiodic Stripe Domain Structures in Magnetic Films of Subcritical Thickness

G. V. Arzamastseva, F. V. Lisovskiĭ*, and E. G. Mansvetova

Institute of Radio Engineering and Electronics, Russian Academy of Sciences (Fryazino Branch), Fryazino, Moscow region, 141120 Russia

**e-mail: lisf@dataforce.net*

Received February 21, 2002

Abstract—The existence of biperiodic stripe domain structures in the vicinity of the lines of orientational phase transitions has been found experimentally in uniaxial films of magnetic garnets of subcritical thickness. It is shown that unidirectional anisotropy induced by the magnetic field, leading to a decrease in the effective rigidity of domain boundaries, is the reason for the observed effect. © *2002 MAIK "Nauka/Interperiodica".*

PACS numbers: 75.70.Kw

It is known that, in thin films of uniaxial magnets with a positive anisotropy constant K_u whose easy magnetization axis (EMA) is directed along the normal **n** to the surface (further on, *z* axis), the ground state in a certain thickness range $L_{cr}^* < L < L_{cr}^{(1)}$ (where L_{cr}^* and $L_{cr}^{(1)}$ are some critical values) corresponds to regular stripe domain structures (DSs) with periodic near-surface modulation of the profile of domain boundaries (DBs) (see [1] and also [2–4]). Branched DSs correspond to thermodynamic equilibrium at $L > L_{cr}^{(1)}$ [5–7], whereas simple (monoperiodic) stripe DSs or single-domain states correspond to thermodynamic equilibrium at $L < L_{cr}^*$. This regularity was repeatedly confirmed experimentally for films differing in structure and composition (see [8] and references therein).

An analysis of the data reported in the available theoretical works[1] shows that the critical thickness can be estimated at $L_{cr}^* \propto \sigma_w/M_0^2$, where $\sigma_w = (AK_u)^{1/2}$ is the surface energy density of domain boundaries, A is the nonuniform exchange interaction constant, and M_0 is the saturation magnetization. The tendency towards a monotonic increase in L_{cr}^* with increasing σ_w or (and) with decreasing M_0 can also be followed in experiments. In the first case, this is mainly associated with the change of the uniaxial anisotropy constant, because the values of A in the materials studied differ little from each other and equal ~10^{-6} erg/cm. Thus, the critical thickness for magnetoplumbite ($K_u = 2.2 \times 10^6$ erg/cm^3, $M_0 = 320$ G) comprises ≃10 μm, whereas $L_{cr}^* = 3$ μm for Permalloy ($K_u = 5 \times 10^4$ erg/cm^3, $M_0 = 800$ G) [3, 8].

In the presence of an external magnetic field $\mathbf{H} = H_\parallel \mathbf{e}_z + H_\perp \mathbf{e}_\perp$, where $H_\parallel$ and $H_\perp$ are the longitudinal and transverse field components with respect to the normal to the film surface, biperiodic DSs retain their stability in a certain range of variation of the strength and direction of **H**. This range corresponds to a region on the ($H_\perp$, $H_\parallel$) plane confined by a diamond-shaped curve. This region is located inside the region of existence of monoperiodic DSs. Investigations carried out with epitaxial films of magnetic $(LuBi)_3(FeMg)_5O_{12}$ garnets grown on nonmagnetic substrates of gadolinium–gallium garnet with the (111) orientation showed that regular biperiodic DSs occur inside the region of stability in three modifications. These modifications differ from each other by the type of modulation of the profile of neighboring domain boundaries, which may be in-phase modulation, out-of-phase modulation, and hybrid modulation (alternating pairs of in-phase and out-of-phase modulated boundaries) [9, 10]. In the absence of a magnetic bias field, "in-phase" biperiodic DSs correspond to the absolute energy minimum. As $H_\parallel$ increases at $H_\parallel = \text{const}$ ($|H_\parallel| < H_\parallel^{(max)}$), where $H_\parallel^{(max)}$ is the upper bound of existence of biperiodic DSs for the given field component), the following chain of first-order phase transitions occurs: in-phase DSs ⟶ hybrid structures ⟶ out-of-phase biperiodic DSs ⟶ simple monoperiodic DSs (with unmodulated DBs). The transformation to a uniformly magnetized state

[1] Because all calculations carried out up to now use the model of geometric (structureless) domain boundaries, only the results for the case $K_u/2\pi M_0^2 \gg 1$ are credible.

upon the disappearance of simple monoperiodic DSs proceeds as a second-order phase transition (or as a first-order phase transition close to a second-order one) [9, 10].

Experiments [9, 10] made by the authors showed that a critical thickness $L_{cr}^* \approx 4$ μm actually exists for films of the chosen composition at $\mathbf{H} = 0$, and only simple (monoperiodic) DSs exist in the films at $L < L_{cr}^*$. However, in studying magnetization reversal in films of subcritical thickness, it was found that biperiodic DSs of the hybrid type (with alternating pairs of in-phase and out-of-phase DBs) arise (at $|H_\parallel| > H_\parallel^{(cr)}$) in a narrow region of magnetic field variations in the vicinity of lines of the phase transition from the domain phase to a uniformly magnetized state. This fact is illustrated in Fig. 1, where the upper part of the phase diagram of a 2.5 μm-thick film is given on the ($H_\perp$, $H_\parallel$) coordinates (the lower part can be obtained by inversion with respect to the origin of the coordinates). The field $H_\parallel^{(cr)}(\phi_H)$ depends on the angle of rotation of the film around the normal to the surface ϕ_H with the third harmonics dominating, which points to the effect of cubic anisotropy. Anomalies appear in the curves of domain structure period d vs. field $H_\perp$ at a constant value of $H_\parallel > H_\parallel^{(cr)}$: instead of a monotonic decrease in the period with increasing $H_\perp$ (see, for example, [10]) typical of thick ($L > L_{cr}^*$) films, a local minimum is observed in the vicinity of the phase transition line, after which the DS period monotonically grows up to film saturation (see Fig. 2, curve for $H_\parallel = 450$ Oe). If $H_\parallel$ does not exceed the critical value (biperiodic DSs do not arise), the dependence $d(H_\perp)$ takes a standard form (curve $H_\parallel = 0$ Oe in Fig. 2). The phenomena described above for films of a chosen composition existed in the range of subcritical thicknesses from 4 down to 1.5 μm.

The reason for the effects observed is contained in the structure of the test samples. The matter is that thin (~0.1 μm) transition layers inevitably arise in films of magnetic garnets obtained by liquid-phase epitaxy at the film interfaces with the substrate and with the free space. These layers strongly differ in their parameters from those of the inner bulk (see, for example, [11, 12]). If it is suggested that one of these layers is characterized by a reduced value of the uniaxial anisotropy constant (as compared to the inner film regions), then such a layer will be magnetized first to saturation ($\mathbf{M} \parallel \mathbf{H}$) as $H_\perp$ increases, whereas domains will still exist in the major part of the film bulk. This is illustrated in Fig. 3, where the amplitude value of the z component of the magnetization vector in the layers is schematically depicted as a function of the strength of the field $H_\perp$ at $H_\parallel = 0$.[2]

[2] At $H_\parallel \neq 0$, the M_z component in the layers becomes different from zero in the magnetic saturation state; however, this does not change in essence the subsequent considerations.

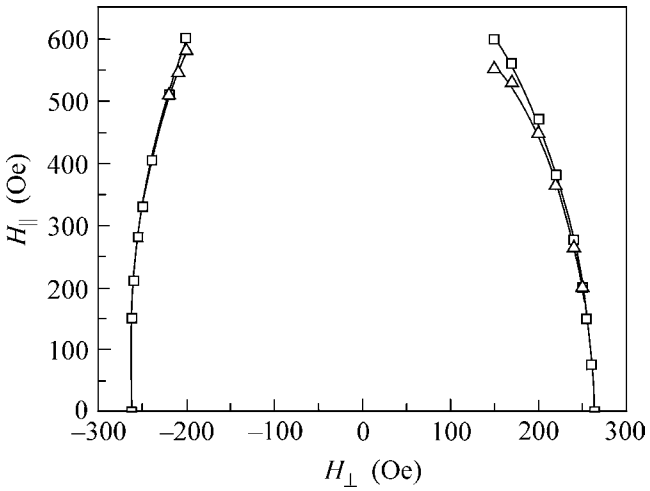

Fig. 1. Phase diagram of a $(LuBi)_3(FeMg)_5O_{12}$ film 2.5 μm thick: □, line of the loss of stability of the uniform state and △, line of the loss of stability of a monoperiodic DS with respect to the transition to a biperiodic structure.

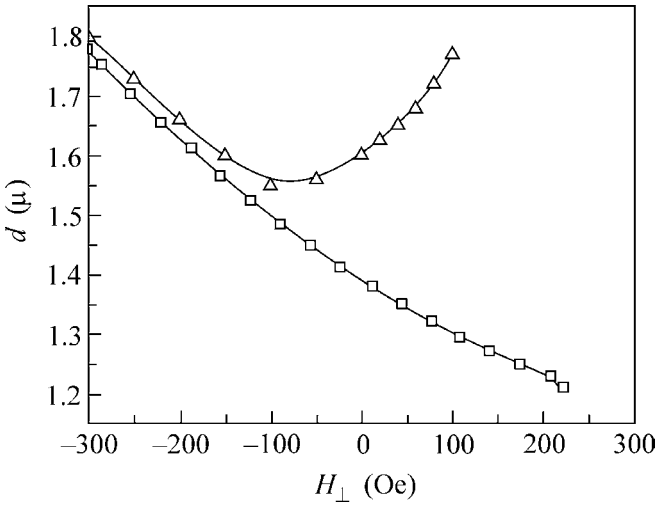

Fig. 2. Dependence of the domain structure period on the field $H_\perp$ for a $(LuBi)_3(FeMg)_5O_{12}$ film 2.5 μm thick: □, $H_\parallel = 0$ Oe and △, $H_\parallel = 450$ Oe.

Because spins on both sides of the interface between the transition layer and the film are coupled by the exchange interaction, the contribution due to uniaxial anisotropy must be taken into account in the total film energy. The energy density of uniaxial anisotropy is described by the equation $w_{ua} = -K_{ua}\cos\theta$, where K_{ua} is the unidirectional (exchange) anisotropy constant and θ is the angle between the **M** and **H** vectors [13]. Exchange interaction between the magnetic moments of the saturated layer and the spins inside the part of the film not magnetized to saturation tends to orient the latter parallel to the **H** vector, increasing the angle of devi-

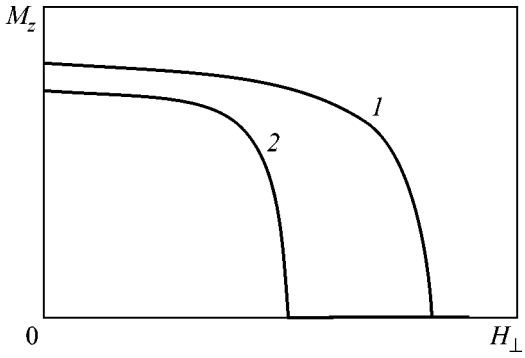

Fig. 3. Dependence of the amplitude value of the *z* component of the magnetization vector (*1*) in the film bulk and (*2*) in the transition layer on the strength of the field $H_\perp$ at $H_\parallel = 0$.

ation of spins from the normal to the surface.[3] From here it follows that the occurrence of unidirectional anisotropy induced by a magnetic field is equivalent to a decrease in the uniaxial anisotropy constant and that this effect becomes most pronounced in the vicinity of the line of the phase transition to a uniformly magnetized state, in which the amplitude of the *z* component of the magnetization vector strongly depends on $H_\perp$ (see Fig. 3). If this transition occurs at $H_\parallel \ll H_\perp$, when the **M** and $\mathbf{H}_\perp$ vectors differ little in their direction, the anisotropy energy density can be presented as

$$w_a \approx -\frac{1}{2}(K_u - K_{ua})\alpha^2 + \frac{1}{2}K_{ua}\phi^2,$$

where $\alpha \ll 1$ and $\phi \ll 1$ are the angles between the **M** vector and either the developed film surface or the $\mathbf{H}_\perp$ vector, respectively. It is evident that the uniaxial anisotropy constant in the remaining part of the film is actually renormalized when the transition layer is magnetized to saturation. This renormalization results in a decrease in the critical thickness and opens up a possibility for the occurrence of biperiodic DSs. This possibility can be realized if the following condition is fulfilled:

$$L - L_{tl} > L_{cr}^{*'},$$

where L_{tl} is the thickness of the transition layer magnetized to saturation and $L_{cr}^{*'}$ is the critical thickness with regard to the induced unidirectional anisotropy.

It was mentioned already that the biperiodic DSs observed experimentally belong to the hybrid type, which is associated with the following reasons. The studies carried out previously [9, 10] showed that DSs with out-of-phase near-surface modulation of the DB profile exist only in the case when the magnetic fields caused by this modulation do not penetrate through the film. This condition is not fulfilled in films of subcritical thickness. Moreover, it was found in the same experiments [9, 10] that the in-phase biperiodic DSs lose their stability with respect to the transformation to arrays with the out-of-phase or hybrid type of modulation at values of $H_\perp$ and $H_\parallel$ far from those corresponding to the line of the phase transition from the nonuniform state to the uniformly magnetized state. Thus, hybrid structures are the only allowed type of DSs in the case under consideration.

The effect of unidirectional anisotropy on the processes of magnetization reversal in films of the chosen composition was also observed for samples whose thickness was larger than the critical value (up to 10 μm). Nonthrough biperiodic hybrid-type DSs also arose in the uniformly magnetized state in a narrow range of magnetic bias fields in the vicinity of the line of the transition from the domain phase. This was accompanied by anomalies in the curve describing the field dependence of the DS period. These phenomena were not observed in thicker films ($L > 10$ μm), which is apparently associated with the fact that unidirectional anisotropy arising from exchange interaction with the transition layer makes a negligibly small contribution to the total energy of films as the film thickness becomes larger.

Effects related to those described above can be observed in films of nonuniform thickness not only in the vicinity of the line of the phase transition (from the domain phase to the uniformly magnetized state) but also away from it and even in the absence of a magnetic field. Strictly speaking, unidirectional anisotropy observed in the experiments described in this work also exists at any (nonsaturating) field strength; however, it manifests itself as a really observable effect only within a narrow region. Therefore, the values of the critical thickness in films with a deliberately created or random gradient of magnetic parameters (saturation magnetization, anisotropy constant, exchange constant, etc.) with respect to thickness can significantly differ from the values for uniform films. This must be taken into account when experimental results are interpreted.

The authors are grateful to L.I. Antonov for discussions of this work and useful recommendations.

This work was supported by the Russian Foundation for Basic Research, project no. 02-02-16338.

[3] The main volume of the film also exerts an effect on the spins of the transition layer through exchange interaction; however, this effect is reduced to only an increase in the strength of the field $H_\perp$ at which the magnetization vector of this layer becomes oriented parallel to the field. The saturated transition layer makes no magnetostatic effect on the main volume of the film, because it follows from the general potential theory that a uniformly charged double layer creates no field in the surrounding space.

REFERENCES

1. B. W. Roberts and C. P. Bean, Phys. Rev. **96**, 1494 (1954).
2. J. Goodenough, Phys. Rev. **102**, 356 (1956).
3. Ya. Katser, Zh. Éksp. Teor. Fiz. **46**, 1787 (1964) [Sov. Phys. JETP **19**, 1204 (1964)].
4. A. Hubert, Phys. Status Solidi **24**, 669 (1967).

5. L. D. Landau, Zh. Éksp. Teor. Fiz. **13**, 377 (1943).
6. E. M. Lifshits, Zh. Éksp. Teor. Fiz. **15**, 97 (1945).
7. I. A. Privorotskiĭ, Usp. Fiz. Nauk **108**, 41 (1972) [Sov. Phys. Usp. **15**, 555 (1972)].
8. L. S. Palatnik, L. I. Lukashenko, Yu. V. Zolotnitskiĭ, and B. A. Avramenko, Zh. Éksp. Teor. Fiz. **59**, 1177 (1970) [Sov. Phys. JETP **32**, 643 (1971)].
9. G. V. Arzamastseva, F. V. Lisovskiĭ, and E. G. Mansvetova, Pis'ma Zh. Éksp. Teor. Fiz. **67**, 701 (1998) [JETP Lett. **67**, 738 (1998)].
10. G. V. Arzamastseva, F. V. Lisovskiĭ, and E. G. Mansvetova, Zh. Éksp. Teor. Fiz. **114**, 2089 (1998) [JETP **87**, 1136 (1998)].
11. R. D. Henry and E. C. Witcomb, Mater. Res. Bull. **10**, 681 (1975).
12. F. V. Lisovskiĭ and E. G. Mansvetova, Mikroélektronika **8**, 331 (1979).
13. W. H. Meikeljohn and C. P. Bean, Phys. Rev. **102**, 1413 (1956).

Translated by A. Bagatur'yants

JETP Letters, Vol. 75, No. 6, 2002, pp. 282–291. Translated from Pis'ma v Zhurnal Éksperimental'noĭ i Teoreticheskoĭ Fiziki, Vol. 75, No. 6, 2002, pp. 332–342.

Collective Effects in the Transport Properties of Two-Dimensional Electron Systems

V. T. Dolgopolov

Institute of Solid-State Physics, Russian Academy of Sciences, Chernogolovka, Moscow region, 142432 Russia

Received January 31, 2002; in final form, February 21, 2002

Abstract—The results of the experimental study of the nontraditional manifestations of collective effects in the transport properties of two-dimensional electron systems are reported. © *2002 MAIK "Nauka/Interperiodica".*

PACS numbers: 73.21.Fg, 73.43.-f

1. STATEMENT OF THE PROBLEM

Interest in strongly correlated electron systems is due to the fact that the theoretical predictions for the systems with strong interaction are mainly based on numerical simulations with a small number of particles. Two-dimensional electron systems are highly suitable as objects for the experimental study of strongly correlated electron liquid, because the energy $E_C = e^2 n_s^{1/2}/\varepsilon$ (e and n_s are the electron charge and concentration, respectively) of interparticle interaction can be controlled experimentally. The fractional quantum Hall effect [1] and the exchange-enhanced spin gap [2] are familiar examples of the manifestation of Coulomb interaction in two-dimensional electron systems. In the absence of magnetic field, the Wigner–Seitz radius defined as $r_s = 1/a_B(\pi n_s)^{1/2}$ (a_B is the Bohr radius) reflects the ratio between the Coulomb and Fermi energies and serves as a parameter of interaction strength. Due to recent progress in semiconductor heterostructure technology, the density of charged particles in a high-mobile Fermi liquid was reduced substantially and the record values $r_s \sim 40$ were attained [3, 4]. In this review, we will only discuss the results of experiments with double quantum wells and silicon field-effect structures.

The transport properties of bilayer systems exhibit a variety of features, many of which are traditionally assigned to the one-electron manifestations and can be explained in the Hartree approximation. Consequently, discrimination between the single-particle and exchange-correlation effects should be the first step on the way to studying the bilayer electron systems. As is shown below, a detailed understanding of the single-particle properties allows one to identify a new phase that appears in a bilayer electron system at the filling factor $\nu = 2$.

Although the silicon field-effect structures are not record holders of the highest attainable r_s values (in these systems, $r_s < 9$), their two-valley electronic spectra and comparatively low extension of electron wave function in the z direction render them competitive objects for studying the exchange-correlation effects.

2. BILAYER ELECTRON SYSTEMS

2.1. Electron wave-function reconstruction induced by normal magnetic field. The appearance of a new degree of freedom in a bilayer electron system requires the introduction of a new quantum number specifying the layer the electron refers to. Formally, this number can be regarded as the projection of a fictitious spin (isospin) onto a certain axis. Under conditions of strong interlayer interaction, the new quantum number gives rise to singularities in the fractional [5–9] and integer [10, 11] quantum Hall effects, as well as to new excitation branches [12] and new quasiparticles [13–15]. The interlayer tunneling results in the symmetric–antisymmetric splitting in the electronic spectrum. The wave function of each electron is extended over both layers, so that one should speak not about layers but about electron subbands. In what follows, so-called "soft" bilayer electron systems, in which the ratio of the distance between the centroids of electron distributions in different subbands to the effective Bohr radius is $\alpha = d/a_B \gg 1$, will mainly be considered [16]. The characteristic property of such systems is that the transfer of a small amount of electrons from one subband to another greatly changes the relative positions of subbands on the energy axis. As will be demonstrated below, the normal quantizing magnetic field is capable of reconstructing the electron wave functions of such systems in the direction perpendicular to the interface [17–19].

The experiments discussed below were carried out with a 700-Å-thick parabolic quantum well grown on a semi-isolating gallium arsenide substrate. A tunnel barrier consisting of three $Al_xGa_{1-x}As$ monolayers with $x = 0.3$ was placed at the center of the well. The well

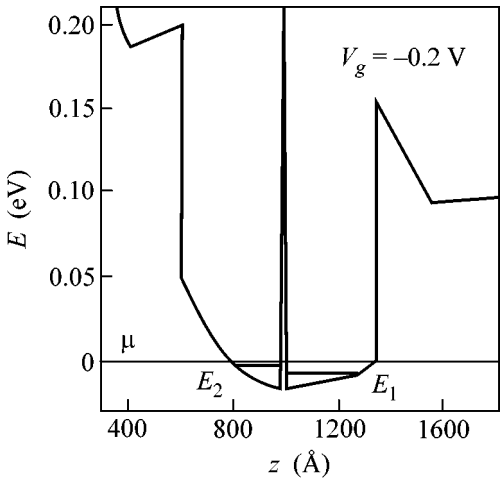

Fig. 1. Conduction band bottom as a function of the distance to the gate for an electrochemical potential difference of –0.2 eV between the gate and the two-dimensional electron layer in the quantum well. Two electron subbands are filled in the parabolic well; the energies of the corresponding subband bottoms are E_1 and E_2.

was symmetrically doped and capped with AlGaAs (600 Å) and GaAs (40 Å) layers. The uppermost layer was covered with a metallic gate, which allowed one to vary the relative populations of layers and conduct magnetocapacitance measurements. One example of the dependence of the conduction band bottom on the distance to the gate in the structure studied is shown in Fig. 1.

Experimentally, the following information could be obtained in the magnetocapacitance measurements: (i) minima, in the (B, V_g) plane, of the thermodynamic density of electron states in the layer nearest to the gate; (ii) positions, in the same plane, of the energy gaps common to the entire electron system; and (iii) activation energy in the middle of the energy gap.

Figure 2a demonstrates the obtained results. In the range from V_{th1} to V_{th2}, the system is single-layer, because all electrons are concentrated in the distant part of the well (the corresponding filling factors are denoted by ν_1). At $V_g > V_{th2}$, the electron system becomes two-layer and the points indicate the gaps common to the entire system. Accordingly, the straight lines drawn through the experimental points show a bend at $V_g = V_{th2}$. The dashed lines indicate minima determined independently for the thermodynamic density of states in the nearest-to-gate layer (ν_2 denotes the corresponding filling factor). For the gate voltages $V_{th1} < V_g < V_{th2}$, the electron concentration in the far part of the well remains virtually unchanged, as is evident from the fact that the lines for identical ν and ν_2 are parallel.

A cardinally different behavior of the points corresponding to the filling factors $\nu = 1$ and 2 and large factors $\nu > 2$ is noteworthy. Whereas for $\nu = 1$ and 2 the energy gap common to the entire bilayer system could be observed up to V_{th2}, there are no points near V_{th2} at larger filling factors, indicating the absence of a gap.

The comparison of the magnetic-field dependences of activation energy for two representative filling factors $\nu = 2$ and 4 is shown in Fig. 3. One can see from this figure that the activation energy for $\nu = 4$ is zero over a broad range of magnetic fields, where the corresponding straight line in Fig. 2 is expected to reach V_{th2}. By contrast, the activation energy for $\nu = 2$ in the vicinity of V_{th2} has a maximum. Such a gap behavior for the filling factors $\nu = 1$ and 2 is evidence for the magnetic-field-induced reconstruction of electron wave functions.

Let us first consider a situation with filling factor $\nu = 4$ for gate voltages slightly exceeding V_{th2}. In the absence of a magnetic field, electrons of two subbands are present in the system: the lower subband with the electron distribution centroid positioned in the distant part of the well and the upper subband whose electrons are nearer to the gate. After introducing the quantizing magnetic field corresponding to the filling factor $\nu = 4$, the initial electron distribution would fill more than

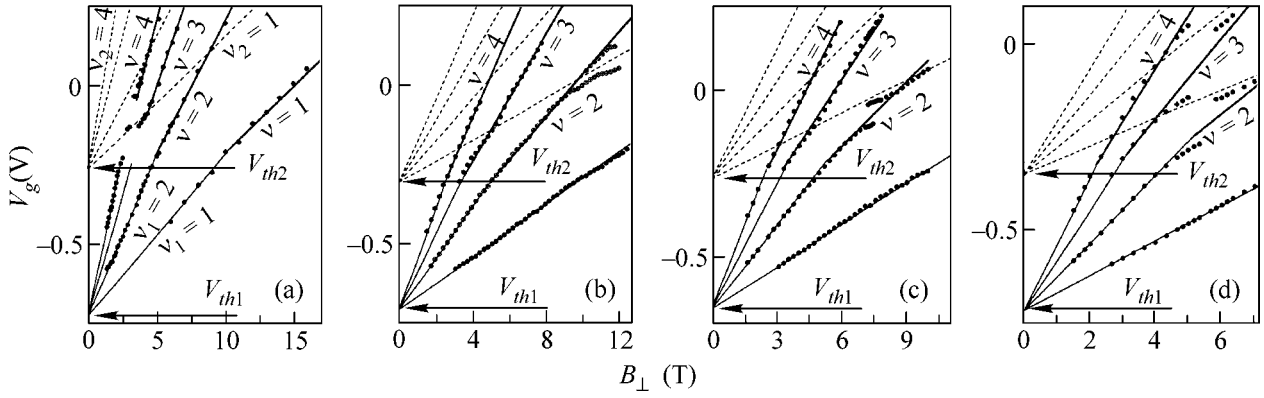

Fig. 2. (dots) Positions of the energy gap in the (V_g, B) plane for a bilayer electron system; magnetic field is (a) normal and (b, c, d) tilted, respectively, at an angle of 30°, 45°, and 60° to the plane.

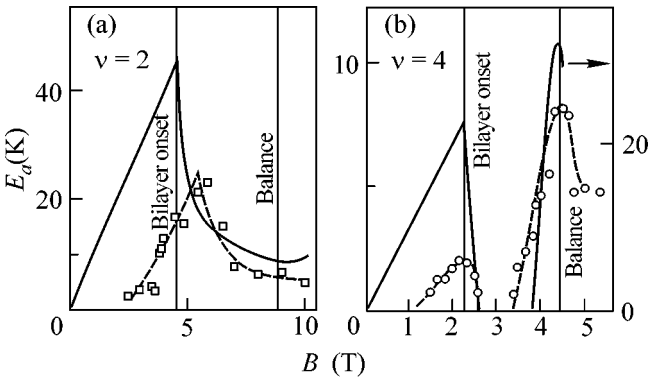

Fig. 3. Activation energy as a function of magnetic field for filling factors ν = 2 and 4. The solid lines are for the calculation, and the dashed lines are drawn through the experimental points.

three quantum levels in the distant subband and less than one level in the near subband, although the overall amount of electrons corresponds to four completely filled levels. Since the partially filled levels generally correspond to different energies, the equilibrium distribution is established by the transfer of some electrons from one subband to another. Consequently, the partially filled levels tend to be pinned to the Fermi level, so that the system will exhibit dissipative conduction even at the integer filling factor.

The above consideration is valid if two conditions are fulfilled. First, the electron system should be soft ($\alpha > 1$). This condition breaks as the balance point is approached, where both the well and the electron distribution are perfectly symmetric since $\alpha = 0$ at this point. The validity of these considerations is demonstrated in Fig. 3, where the gap calculated for ν = 4 is compared with its experimentally measured value. The qualitative agreement between the calculated and experimental values is clearly seen. The quantitative discrepancy can easily be explained by the finite width of quantum levels.

The second condition is more crucial. The off-diagonal matrix elements of the perturbation caused by the electron transfer from one subband to another must be zero. In other words, the transfer of a small amount of electrons between the subbands must not disturb the motion of other electrons in the *z* direction. This is possible only if the wave functions of the initial and final states belong to different Landau levels. This condition is met for the electron transition from the zeroth to the first Landau level (ν = 4). Otherwise (e.g., ν = 1 and 2), the wave functions undergo reconstruction in the *z* direction, and the Fermi level falls within the gap. The gap calculated for ν = 2 from these considerations is shown in Fig. 3 by the solid line. One can see from this figure that the calculated and experimental curves display qualitatively similar behavior.

It is instructive to compare the electron-density distributions in the *z* direction before and after the reconstruction induced by the quantizing magnetic field (Fig. 4). The squares of moduli of electron wave functions before the reconstruction are shown in the inset in Fig. 4. Electrons of the lower subband are mainly located in the distant part of the well, while the electron- distribution centroid in the upper subband is shifted toward the gate. The overall zero-field density

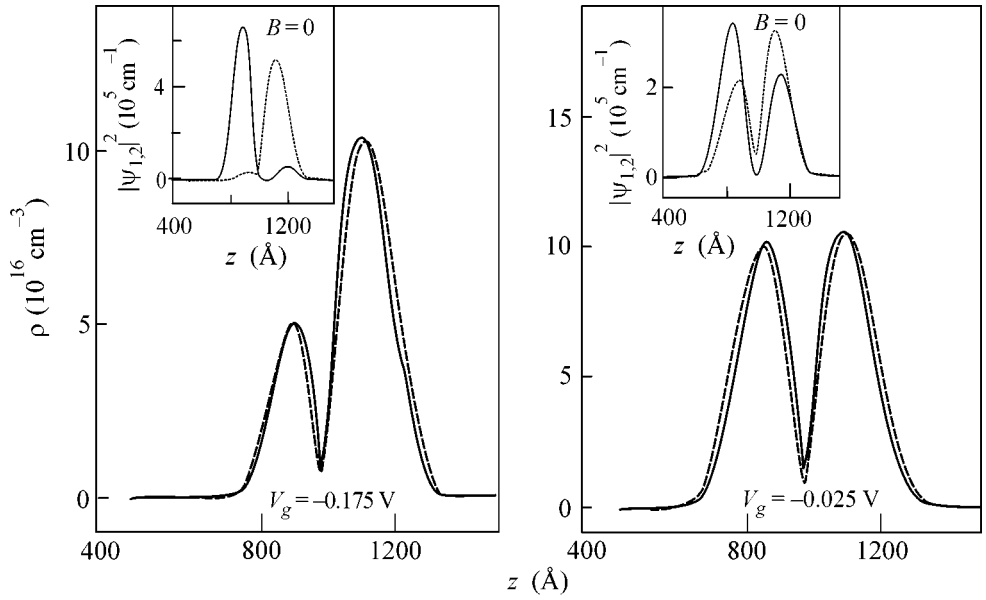

Fig. 4. Electron-density distribution in a quantum well (dashed lines) before and (solid lines) after the reconstruction of wave functions at different values of V_g. The squares of moduli of zero-field electron wave functions are shown in the insets for the two lowest subbands.

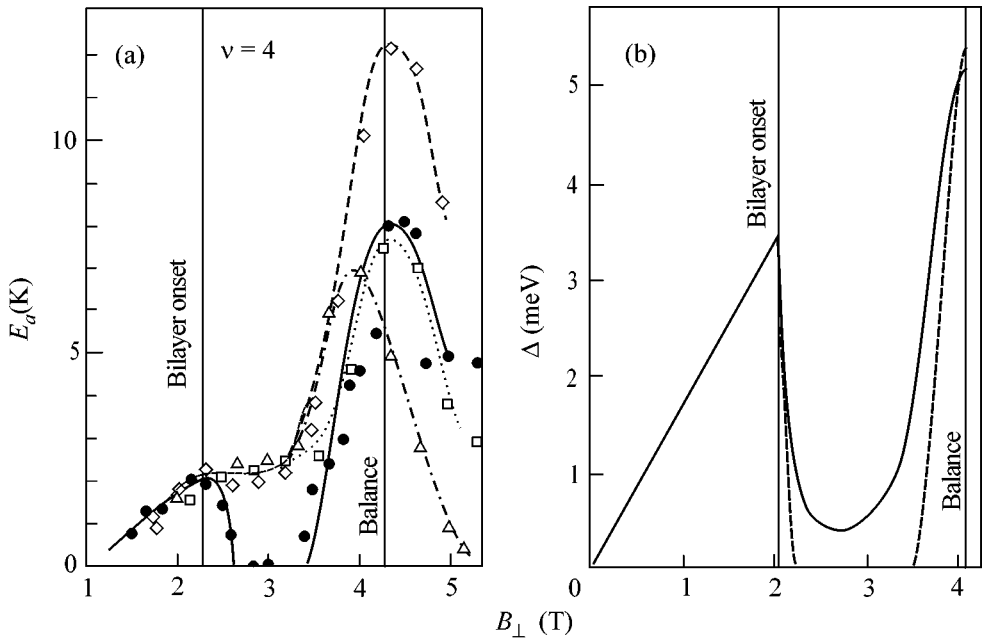

Fig. 5. (a) Experimental and (b) calculated (for tilt angles 0° and 30°) dependences of activation energy on the normal component of a magnetic field.

distribution is shown by the dashed line in the body of Fig. 4. After applying the quantizing magnetic field, only one subband with a hybrid wave function extended over both well parts becomes filled. The corresponding electron-density distribution is shown in Fig. 4 by the solid line. One can see from this figure that the wave-function reconstruction is accompanied by an insignificant deformation of electron density.

2.2. Independent experimental verification. The above considerations can easily be verified experimentally [19]. Indeed, if a parallel magnetic field is added to the quantizing normal component, the second condition will be broken for an arbitrary filling factor. Consequently, the partially filled quantum levels will not appear for overall integer filling.

Away from the balance point, the intersubband tunneling leads to the electron displacement in the *z* direction. In the presence of a parallel magnetic-field component, the *z* displacement is caused by shifting the centroid of one-electron wave function in the (*X*, *Y*) plane [20]. The shifted one-electron wave functions of different Landau levels are not mutually orthogonal, and, hence, the corresponding off-diagonal matrix elements are nonzero.

As an illustration, the magnetic-field dependence of activation energy is displayed in Fig. 5a for a fixed filling factor $\nu = 4$ and for the following angles between the direction of the magnetic field and the normal: (circles) 0°, (rhombi) 30°, (squares) 45°, and (triangles) 60°. In the range of magnetic fields where the zero-field gap is absent, a common gap opens for the two-layer system even at an angle of 30°, and it remains virtually unchanged upon further increase in the tilt angle of magnetic field. The experimental dependence can be compared with the calculation based on taking into consideration the wave-function in-plane shift caused by the tunneling in the parallel magnetic field (Fig. 5b). In this case, the calculation also agrees nicely with the experiment on a qualitative level.

The results of the experiments described above can be formulated as follows. We succeeded in identifying the single-particle effects in the spectrum of a soft bilayer electron system exposed to the quantizing magnetic field. The additional spectral features observed for the double quantum well in a tilted magnetic field should be interpreted as the manifestations of many-body effects.

2.3. Canted antiferromagnetic phase. In the quantizing magnetic field, each Landau level of a bilayer electron system has two characteristic energy scales: spin (Zeeman) and isospin (symmetric–antisymmetric) splittings, whose ratio determines the state of the system for a given filling factor. The Coulomb electron–electron interaction specifies one more characteristic energy, which ordinarily greatly exceeds both single-particle energies.

In the simplest single-particle picture, a system with the filling factor $\nu = 2$ undergoes a transition from the nonpolarized ground state to the completely spin-polarized (ferromagnetic) state as the magnetic field increases and the Zeeman energy μgB becomes equal to the symmetric–antisymmetric splitting energy Δ_{SAS}. In the presence of electron–electron interaction [15, 21–24], first, the transition region shifts to lower magnetic fields

$$\mu gB \approx \Delta_{SAS}^2/E_C, \quad \Delta_{SAS} \ll E_C, \tag{1}$$

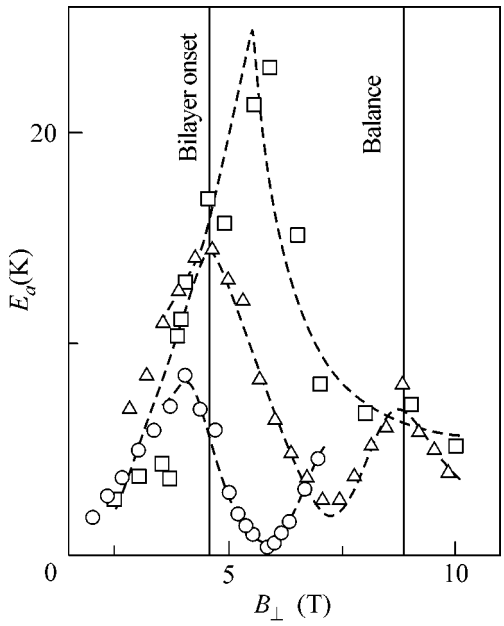

Fig. 6. Activation energy as a function of the normal component of a magnetic field for filling factor ν = 2 and tilt angles of magnetic field (□) 0°, (△) 45°, and (○) 60°.

and, second, the two lowest states of the electron system mix in the vicinity of a point defined by Eq. (1) to form a new ground state—canted antiferromagnetic phase—in a gap between the spin-nonpolarized and ferromagnetic phases. The new phase is characterized by antiferromagnetic in-plane spin correlations. In the domain of existence of the new ground state of a two-layer system, the mean electron-spin projection onto the direction of the magnetic field changes continuously from $S_z = 0$ at the boundary of the nonpolarized phase to $S_z = 1/2$ at the boundary of the ferromagnetic state.

The existence of a canted antiferromagnetic phase was also predicted for an unsymmetrical (unbalanced) two-layer system [24]. Moreover, in the presence of a disbalance induced by an external electric field one can continuously vary sample parameters such as the well profile and the energy difference between the two lower size-quantization levels. The canted antiferromagnetic phase in a tilted magnetic field was not considered theoretically, although the field tilting, clearly, should facilitate its formation.

In experimental works [25, 26], inelastic light backscattering was used to study the spin structure of long-wavelength excitations in the spectrum of symmetric double wells exposed to a normal [25] and tilted [26] magnetic field in the vicinity of filling factor ν = 2. It was found indirectly that the lowest excitation mode softens to zero energy [25], providing evidence of a transition to a new state intermediate between the spin-nonpolarized and ferromagnetic states. In addition, the temperature dependence of excitations in the new phase counts in favor of the occurrence of the Kosterlitz–Thouless transition in the canted antiferromagnetic phase.

A point at which the activation energy drops abruptly in the region where the Zeeman energy is appreciably lower than Δ_{SAS} was observed in the transport experiments [27, 28]. It should be noted that the conductivity carries information only on the charged excitations. Moreover, in the quantizing magnetic field, it provides information only on the high-momentum excitations. Because of this, the question of whether the change in the ground-state spin orientation can be detected in the conductivity measurements has remained open. It was shown in theoretical work [29] that the energy of charged excitations has a minimum in the middle of the region corresponding to the canted antiferromagnetic phase.

Experimentally, such a minimum appears in a tilted magnetic field for the filling factor ν = 2 (Fig. 2). The points corresponding to ν = 2 exhibit splitting in the vicinity of balance even for a tilt angle of 30° (Fig. 2). It is seen from Fig. 2 that the splitting center shifts to a more negative gate voltage as the tilt angle increases.

Knowing the value $\Delta_{SAS} = 1.3$ meV from the numerical calculation and measurements [30, 31] and using Eq. (1), one can estimate the Coulomb energy in the vicinity of a balance point, $E_C \sim 6$ meV. This value is smaller than $e^2/\varepsilon l = 15$ meV (l is the magnetic length), because the wave functions are smeared in the z direction. Note that the appearance of two experimental points corresponding to the maxima of activation energy in the same magnetic field (Fig. 2) is evidence of the competition between two ground states in the two-layer system considered.

The behavior of activation energy is illustrated in Fig. 6 for ν = 2 and different tilt angles of the magnetic field. At gate voltages $V_{th1} < V_g < V_{th2}$, the activation energy in the single-layer regime increases with the magnetic field, reflecting the increase in the cyclotron gap. In this region, the activation energy shows little dependence on the tilt angle of the magnetic field. In the field corresponding to the splitting point in Fig. 2, a deep minimum appears for the activation energy in a tilt magnetic field. As the tilt angle increases, then, in accordance with Eq. (1), the Zeeman energy increases and the minimum of the activation energy shifts to smaller normal magnetic-field components, where the symmetric–antisymmetric splitting is greater (Fig. 3). These results are in compliance with the predictions made in [15, 21–24, 29] and are evidence for the formation of a canted antiferromagnetic phase.

3. TWO-DIMENSIONAL ELECTRON GAS OF A SILICON FIELD-EFFECT STRUCTURE IN A PARALLEL MAGNETIC FIELD

3.1. Current status of investigations. The following features of electron gas in the most popular silicon

field-effect (100)-Si-based structures make them attractive objects for studying the exchange-correlation effects (for detail, see [2]). (i) As mentioned above, for the same electron density the wave functions in the silicon structures are more compact in the direction normal to the interface than in the GaAs/AlGaAs heterostructures; (ii) at zero magnetic field, electrons occupy two different valleys corresponding to the two minima of the conduction band at different points in the three-dimensional k space. Accordingly, the description of the electron state necessitates the introduction of an additional quantum number; in this respect, a single-layer silicon structure is equivalent to a two-layer gallium arsenide structure; (iii) finally, the ratio of the Coulomb interaction to the kinetic energy is appreciably higher in the silicon structures. Indeed, the kinetic energy decreases by virtue of the greater electron mass and the two-valley spectrum. By contrast, the potential energy increases because of the lower static dielectric constant.

Clearly, the studies of a two-dimensional electron gas in silicon field-effect structures with low electron concentration and, hence, particularly strong correlation and exchange effects hold the greatest promise. Technically, the corresponding studies are hampered for ordinary structures, because the electron density near contacts is reduced, so that, starting at a concentration of $\sim 3 \times 10^{11}$ cm^{-2}, the contacts for the two-dimensional electron gas become high-ohmic. In recent years, silicon structures with a split gate have been fabricated [32], for which this problem was solved.

The history of studying high-mobility [$\mu \sim 20000$–40000 cm^2/(V s)] silicon structures with low electron densities includes several stages. At the early stage, the prime objective of investigations consisted in attempts to prove that the dielectric phase observed at low electron densities and finite temperatures is a Wigner crystal [33]. Indeed, it was found in some works (see, e.g., [33, 34]) that the collective effects play an important part in the dielectric phase and that the characteristic length appreciably exceeds the separation between localization centers. At the same time, it was realized that this was by no means classical crystal with a long-range order, because the concentration of charged impurities at the SiO_2/Si interface in the best structures was 4×10^{10} cm^{-2}, i.e., comparable with the electron concentration in the dielectric phase ($\sim 8 \times 10^{10}$cm^{-2}).

The second stage was initiated by the discovery of the fact that conductivity increases with decreasing temperature at electron concentrations slightly exceeding the concentration typical of the transition to the dielectric state at a finite temperature [35]. The presence of a positive derivative dR/dT down to the lowest attainable temperature of ~30 mK held hope that the derivative would remain non-negative at a temperature as low as one would like and, hence, that the two-dimensional electron gas in the silicon field-effect structures would undergo a metal–insulator quantum phase transition at zero temperature [36]. The statement that the metallic phase exists at zero temperature came under criticism in some works (see, e.g., [37]). Based on the prediction that the metal–insulator quantum phase transition is absent in a two-dimensional electron system without interaction [38], doubt was cast upon the extrapolation to zero temperature following the experimentally observed law.[1] Interest in the unsolved problem on the nature of the dielectric phase observed at low electron concentrations was lost.

In a purely experimental context, the question of the existence or absence of the metal–insulator quantum phase transition in silicon structures is nowadays a matter of trust, because, to reliably answer this question, temperatures on the scale of $\exp(-G)$ are necessary, where G is the dimensionless conductance, whose typical values for the electron system are on the order of $G \sim 10^2$. Nevertheless, the region of low electron concentrations is of great interest for investigations, because a strong electron–electron interaction should reveal itself both in the absence of a magnetic field and in the presence of quantizing magnetic fields. An example can be provided by a recent indication of the possible spontaneous spin polarization in a two-dimensional system with finite electron density [39, 40].

3.2. Idea of the method. The study of the dependence of resistance on the parallel magnetic field can be used for the experimental determination of the complete-spin-polarization field B_c for a two-dimensional electron system, because the resistance is expected to be saturated at higher fields.

Let us consider the conductivity of a two-dimensional electron gas in a magnetic field parallel to the plane of the two-dimensional electron system. Assume that the electron wave function in the direction normal to the interface is compact to such an extent that one may ignore field-induced mixing of electron in-plane motion with the motion in the z direction [41]. In the absence of a magnetic field, every state with a fixed momentum is fourfold degenerate due to the spin and valley degeneracy. A strong magnetic field removes the spin degeneracy. Following [42], let us consider electron scattering (without spin flip) by charged impurities situated in the plane of the two-dimensional electron gas.

The transport relaxation time is [43]

$$\tau^{-1} = 2\pi e^4 m N_i g_v \hbar^{-3} k_F^{-2} \times \int_0^1 dx x^2 (1-x^2)^{-1/2} (x+X)^{-2}, \quad (2)$$

[1] It is worth noting that the opposite statement about the absence of a metal–insulator transition and the existence of a dielectric phase at zero temperature for an arbitrary electron concentration also rests on the extrapolation to zero temperature. However, the extrapolation in this case follows the law which is not observed experimentally at a comparatively low electron concentration of $\sim 10^{11}$cm^{-2}.

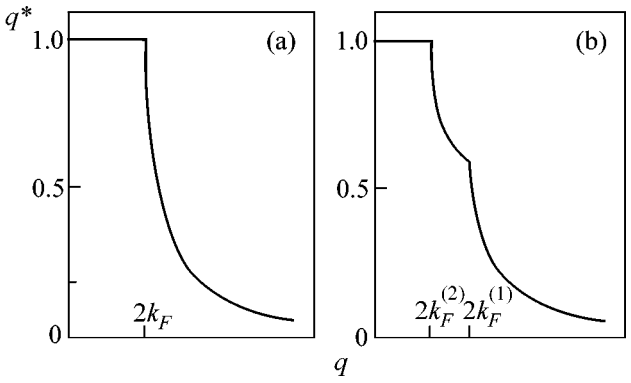

Fig. 7. Effective screening parameter as a function of momentum transfer: (a) without the magnetic field and (b) in a parallel magnetic field.

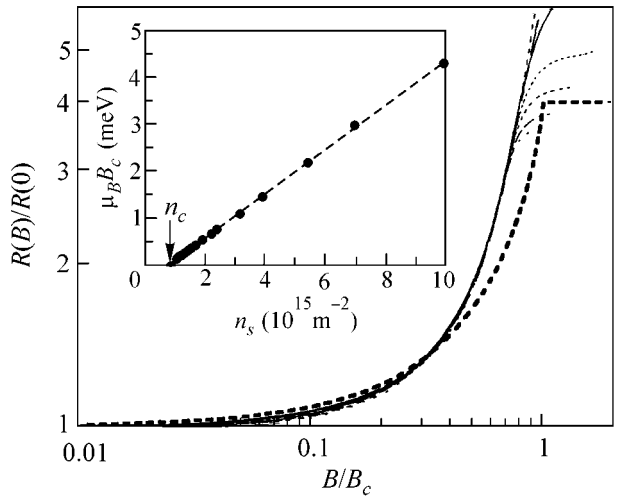

Fig. 8. Scaled plots of resistance vs. parallel magnetic field for 15 different values of electron concentrations in the range from 1.08×10^{11}cm^{-2} to 9.93×10^{11}cm^{-2}. The dashed line corresponds to the calculated dependence [42]. Inset: the complete-spin-polarization field as a function of electron density.

where e and m are the electron charge and mass, respectively, k_F is the Fermi wave vector, $g_v = 2$ stands for the valley degeneracy, N_i is the impurity concentration at the interface, $X = q_0 q^*/2k_F$, q_0 is the spin-nonpolarized Thomas–Fermi wave vector, and q^* is the effective screening parameter. In the matrix element describing the electron interaction with a screened impurity, only the Hartree term is included. It was demonstrated in a recent work [44] that the Fock's term may be important for the systems with strong interaction. In the absence of a magnetic field in the region where both calculations are valid without fitting parameters (electron density $\geq 3 \times 10^{11}$cm^{-2}), the results of work [44] coincide with the predictions of earlier work [43] with an accuracy of 20% and are consistent with the experiment with the same accuracy. Inasmuch as the contribution from the Fock's term is poorly known for the real Coulomb potential, this term is omitted in the description of the idea of the method. In Eq. (2), the screening of Coulomb potential is taken into account in the random-phase approximation. In the general case, two parallel conduction channels corresponding to electron spins aligned with the magnetic field (Fermi momentum $k_F^{(1)}$) and with the momentum antiparallel to the field ($k_F^{(2)}$) exist in a partially spin-polarized system. The relaxation time for each channel is given by Eq. (2) with the appropriate $X(x)$ function. The qualitative form of the function $q^*(q)$ in zero magnetic field is shown in Fig. 7. The abrupt drop of $q^*(q)$ at momentum $2k_F$ corresponds to the weakening of screening and leads to the Friedel oscillations.

Let us first consider high electron concentrations, $2k_F \ll q_0$. In this case, considering that the scattering occurs from the unscreened potentials, the quantity X in the majority of scattering events can be ignored compared to x in Eq. (2). In a magnetic field completely polarizing the electron system, k_F in Eq. (2) is doubled and, correspondingly, the conductivity of the electron system increases twofold. Unfortunately, this situation is practically unattainable in the silicon field-effect structures.

In the opposite limit $2k_F \ll q_0$ or $X \gg 1$, all scattering events proceed on a screened potential, and the conductivity decreases fourfold upon attaining complete spin polarization. Note that the condition $2k_F \ll q_0$ lies beyond the limits of application of the random-phase approximation. It is customarily assumed [45] that the Hubbard-type corrections allow the region of applicability of Eq. (2) to be sizably extended. Since the introduction of these corrections does not qualitatively change the results, only the simplest version of calculations will be considered below.

For an arbitrary spin polarization in a weakly disordered system, $0 < \xi < 1$ ($\xi = (n_u - n_d)/(n_u + n_d) = g^*\mu_B/2E_F$), the effective screening parameter is a two-step function, as depicted in Fig. 7. One can see from this figure that, even at $2k_F \ll q_0$, only a part of the scattering events with a momentum transfer smaller than $k_F^{(2)}$ proceeds on a well-screened potential. The fraction of such scattering processes decreases with increasing magnetic field and becomes zero in the field B_c corresponding to complete spin polarization. The scattering does not change upon further increase in the magnetic field.

Therefore, the study of the behavior of a two-dimensional electron system in a parallel magnetic field allows the complete-spin-polarization field B_c to be experimentally measured. Knowing the value of B_c and the electron concentration, as determined, e.g., from the weak-field Hall effect, one can determine the product of effective mass into the effective g factor,

$$m^* g^* = \pi \hbar n_S / \mu_B B_c. \quad (3)$$

3.3. Ferromagnetic instability. The procedure proposed above was implemented using a silicon field-effect structure in the form of a Hall bridge with a split gate [39]. The electron mobility at its maximum at a temperature of 0.1 K was equal to 30 000 $cm^2/(V\ s)$. The $R(B)$ curves obtained in these experiments were similar to the curves obtained in earlier works, but the accuracy of measuring resistance was higher because of a higher quality of the contacts with the two-dimensional layer.

The resistance saturation in a magnetic field could be observed only for electron concentrations $n_s < 2.5 \times 10^{11}$ cm^{-2}. Upon a further rise in concentration, the value of B_c exceeded the highest attainable magnetic field. The B_c values at higher concentrations were determined by the scaling procedure. According to Eq. (2), the function $R(x)/R(0)$ must be universal for different electron concentrations. Because of this, the parameter B_c was chosen so as to fit the experimental curves to the universal function $R(B/B_c)/R(0)$ (Fig. 8). One can see in Fig. 8 that the scaling is remarkably accurate for $B/B_c < 0.8$ and electron densities from 1.1×10^{11} to 10^{12} cm^{-2} and that the universal curve agrees well with the calculation in [42].

The resulting dependence of the critical field on the electron concentration is displayed in Fig. 8. To a high accuracy, this dependence proved to be linear. Its extrapolation to $B_c = 0$ gave a nonzero electron density n_c virtually coinciding with the critical concentration corresponding to the metal–insulator transition in the structure studied [46]. It would be natural to assume that the number of free electrons becomes zero at this concentration. However, the electron concentration found by measuring Hall resistance in a weak magnetic field proved to be equal to the total electron density (Fig. 9).

Thus, the extrapolation of the measured $B_c(n_s)$ dependence to the point $B_c = 0$ suggests that the spontaneous spin polarization is possible at a nonzero electron density. It should be specially emphasized, first, that this conclusion is based on an extrapolation (although only through 20% of the electron concentration). Second, the fact that the critical field disappears does not necessarily imply ferromagnetic instability. The instability could just as readily be antiferromagnetic. Free electron gas is expected to exhibit precisely this ferromagnetic instability. In the sample studied, the instability concentration proved to be the same as the concentration corresponding to the metal–insulator transition. For the other samples (see, e.g., [47]), the metal–insulator transition was observed at higher electron concentrations. It still remains unclear as to whether the ferromagnetic Fermi liquid appeared; i.e., whether the metal–insulator transition can be observed at concentrations lower than 8×10^{11} cm^{-2}.

It is instructive to compare this result with the results of independent measurements initiated by work

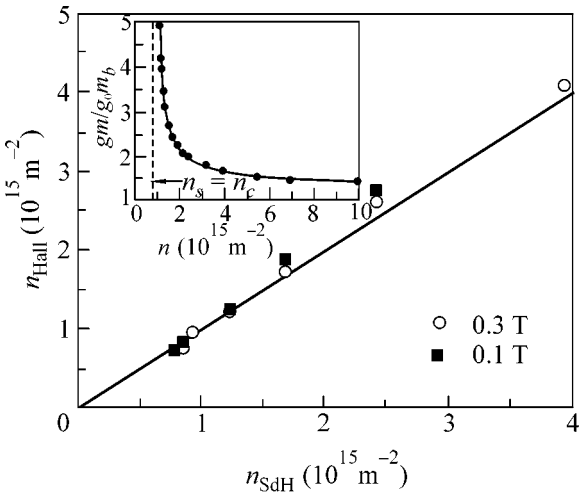

Fig. 9. Comparison of the electron density derived from the Hall effect in a weak magnetic field with the total electron concentration. Inset: the product m^*g^* as a function of electron concentration.

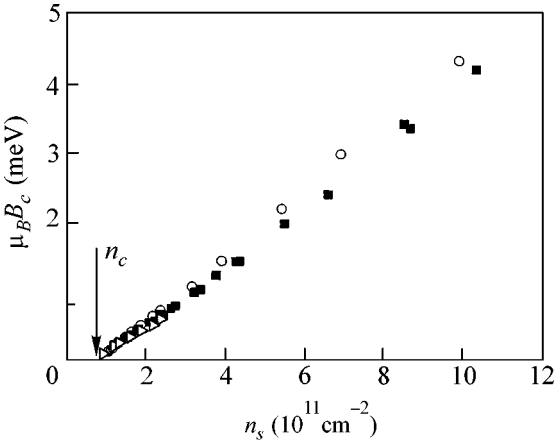

Fig. 10. Comparison of the results obtained by different experimental groups by different methods. (Circles) [39], (triangles) [40], and (squares) [48].

[39]. Such a comparison is illustrated in Fig. 10, where the results of direct measurements of B_c are presented together with the critical field calculated from Eq. (3) with the use of the measured m^*g^* product (the data [39] recalculated to m^*g^* are given in the inset in Fig. 9). One can see in Fig. 10 that the products m^*g^* obtained by different experimental groups [39, 40, 48] for different samples and by different methods proved to be identical within the experimental accuracy [49].

According to the theoretical calculations for clean two-dimensional electron systems [50], one should expect that a paramagnetic Fermi liquid undergoes transition directly to a Wigner crystal. However, the ground-state energies of a Wigner crystal and a ferromagnetic Fermi liquid proved to be close even in the

clean system. Numerical calculation [51] suggests that the disorder favors the transition of a Fermi liquid to the ferromagnetic state.

4. OUTLOOK FOR FUTURE INVESTIGATIONS

The prominent manifestations of the exchange-correlation effects demonstrated by both studied systems call for further investigations. It is necessary to reveal the conditions for the formation of a canted antiferromagnetic phase in quantum double wells with a systematically varied penetrability of the tunnel barrier and to elucidate the type of elementary charge-carrying excitations. The latter issue is of particular interest for the systems with strong disbalance, where electrons of different subbands are spatially separated in the absence of a quantizing magnetic field.

In fact, the inset in Fig. 8 represents a portion of the phase diagram in the (n_s, B) plane for the silicon field-effect structures. The challenge of the immediate future is to construct the entire phase diagram including both the region of the metal– insulator transition at nonzero temperatures and the third axis corresponding to disorder. It is clear from the above that the silicon field-effect structures with a split gate are ideal objects for studying the spin injection into a two-dimensional electron system, because its spin state in a parallel magnetic field is controlled by the electron concentration, while the electron system can be made two-dimensional both in the contact region and between the contacts.

I am grateful to A.A. Shashkin, É.V. Deviatov, V.S. Khrapai, G.É. Tsydinzhapov, A. Gold, S.V. Kravchenko, T.M. Klapwijk, A. Wixforth, F. Hastreiter, M. Hartung, K.L. Campman, and A. Gossard for authorizing the use of jointly obtained results and to J.P. Kotthaus and V.F. Gantmakher for helpful discussions. This work was supported by the Russian Foundation for Basic Research, project nos. 01-02-16424 and 00-02-17294.

REFERENCES

1. *The Quantum Hall Effect*, Ed. by R. Prange and S. Girvin (Springer-Verlag, New York, 1987; Mir, Moscow, 1989).
2. T. Ando, A. B. Fowler, and F. Stern, Rev. Mod. Phys. **54**, 437 (1982).
3. J. Yoon, C. C. Lee, D. Shahar, *et al.*, Phys. Rev. Lett. **82**, 1744 (1999).
4. A. P. Mills, Jr., A. P. Ramirez, L. N. Pfeiffer, and K. W. West, Phys. Rev. Lett. **83**, 2805 (1999).
5. T. Chakraborty and P. Pietilainen, Phys. Rev. Lett. **59**, 2784 (1987).
6. D. Yoshioka, A. H. MacDonald, and S. M. Girvin, Phys. Rev. B **39**, 1932 (1989).
7. J. P. Eisenstein, G. S. Boebinger, L. N. Pfeiffer, *et al.*, Phys. Rev. Lett. **68**, 1383 (1992).
8. Y. W. Suen, L. W. Engel, M. B. Santos, *et al.*, Phys. Rev. Lett. **68**, 1379 (1992).
9. Y. W. Suen, H. C. Manoharan, X. Ying, *et al.*, Phys. Rev. Lett. **72**, 3405 (1994).
10. S. Q. Murphy, J. P. Eisenstein, G. S. Boebinger, *et al.*, Phys. Rev. Lett. **72**, 728 (1994).
11. T. S. Lay, Y. W. Suen, H. C. Manoharan, *et al.*, Phys. Rev. B **50**, 17725 (1994).
12. I. B. Spielman, J. P. Eisenstein, L. N. Pfeiffer, and K. W. West, cond-mat/0012094.
13. M. Abalfath, L. Radzihovsky, and A. H. MacDonald, cond-mat/0110049.
14. Y. N. Joglekar and A. H. MacDonald, cond-mat/0108077.
15. L. Zheng, R. J. Radtke, and S. Das Sarma, Phys. Rev. Lett. **78**, 2453 (1997).
16. A. Gold, Z. Phys. B **95**, 341 (1994).
17. V. T. Dolgopolov, A. A. Shashkin, E. V. Deviatov, *et al.*, Phys. Rev. B **59**, 13235 (1999).
18. V. T. Dolgopolov, G. E. Tsydinzhapov, A. A. Shashkin, *et al.*, Pis'ma Zh. Éksp. Teor. Fiz. **67**, 563 (1998) [JETP Lett. **67**, 595 (1998)].
19. E. V. Deviatov, V. S. Khrapai, A. A. Shashkin, *et al.*, Pis'ma Zh. Éksp. Teor. Fiz. **71**, 724 (2000) [JETP Lett. **71**, 496 (2000)].
20. P. H. Beton, J. Wang, N. Mory, *et al.*, Phys. Rev. Lett. **75**, 1996 (1995).
21. S. Das Sarma, S. Sachdev, and L. Zheng, Phys. Rev. Lett. **79**, 917 (1997).
22. S. Das Sarma, S. Sachdev, and L. Zheng, Phys. Rev. B **58**, 4672 (1998).
23. E. Demler and S. Das Sarma, Phys. Rev. Lett. **82**, 3895 (1999).
24. L. Brey, E. Demler, and S. Das Sarma, Phys. Rev. Lett. **83**, 168 (1999).
25. V. Pellegrini *et al.*, Phys. Rev. Lett. **78**, 310 (1997).
26. V. Pellegrini *et al.*, Science **281**, 799 (1998).
27. A. Sawada, Z. F. Ezawa, H. Ohno, *et al.*, Phys. Rev. Lett. **80**, 4534 (1998).
28. V. S. Khrapai, E. V. Deviatov, A. A. Shashkin, *et al.*, Phys. Rev. Lett. **84**, 725 (2000).
29. V. Falko, S. V. Iordanski, and A. Kashuba, cond-mat/0003120.
30. G. Salis, B. Graf, K. Ensslin, *et al.*, Phys. Rev. Lett. **79**, 5106 (1997).
31. M. Hartung, A. Wixforth, K. L. Campman, and A. C. Gossard, Solid-State Electron. **40**, 113 (1996).
32. S. V. Kravchenko, D. Simonian, M. P. Sarachik, and T. M. Klapwijk, Phys. Rev. B **59**, R12740 (1999).
33. V. M. Pudalov, M. D'Iorio, S. V. Kravchenko, and J. W. Campbell, Phys. Rev. Lett. **70**, 1886 (1993).
34. A. A. Shashkin, V. T. Dolgopolov, and G. V. Kravchenko, Phys. Rev. B **49**, 14 486 (1994).
35. S. V. Kravchenko, G. V. Kravchenko, J. E. Furneaux, *et al.*, Phys. Rev. B **51**, 7038 (1995).
36. E. Abrahams, S. V. Kravchenko, and M. P. Sarachik, Rev. Mod. Phys. **73**, 251 (2001).
37. B. L. Altshuler, D. L. Maslov, and V. M. Pudalov, Physica E (Amsterdam) **9**, 209 (2001).
38. E. Abrahams, P. W. Anderson, D. C. Licciardello, and T. V. Ramakrishnan, Phys. Rev. Lett. **42**, 673 (1979).

39. A. A. Shashkin, G. V. Kravchenko, V. T. Dolgopolov, and T. M. Klapwijk, Phys. Rev. Lett. **87**, 086801 (2001); cond-mat/0007402.
40. S. A. Vitkalov, H. Zheng, K. M. Mertes, *et al.*, Phys. Rev. Lett. **87**, 086401 (2001).
41. S. Das Sarma and E. H. Hwang, Phys. Rev. Lett. **83**, 164 (1999).
42. V. T. Dolgopolov and A. Gold, Pis'ma Zh. Éksp. Teor. Fiz. **71**, 42 (2000) [JETP Lett. **71**, 27 (2000)].
43. A. Gold and V. T. Dolgopolov, Phys. Rev. B **33**, 1076 (1986).
44. Gabor Zala, B. N. Narozhny, and I. L. Aleiner, Phys. Rev. B **64**, 214204 (2001).
45. A. Gold and W. Götze, Solid State Commun. **47**, 627 (1983); Phys. Rev. B **33**, 2495 (1986).
46. A. A. Shashkin, S. V. Kravchenko, and T. M. Klapwijk, cond-mat/0009180.
47. V. M. Pudalov, G. Brunthaler, A. Prinz, and G. Bauer, cond-mat/0103087.
48. V. M. Pudalov, M. Gershenson, H. Kojima, *et al.*, cond-mat/0105081.
49. S. V. Kravchenko, A. A. Shashkin, and V. T. Dolgopolov, cond-mat/0106056.
50. B. Tanatar and D. M. Ceperley, Phys. Rev. B **39**, 5005 (1989).
51. G. Beneti, G. Caldara, and D. L. Shepelyansky, Phys. Rev. Lett. **86**, 5333 (2001).

Translated by V. Sakun

JETP Letters, Vol. 75, No. 6, 2002, pp. 292–296. Translated from Pis'ma v Zhurnal Éksperimental'noĭ i Teoreticheskoĭ Fiziki, Vol. 75, No. 6, 2002, pp. 343–347.

Aharonov–Bohm Effect for Composite Particles and Collective Excitations

A. V. Chaplik

Institute of Semiconductor Physics, Siberian Division, Russian Academy of Sciences, pr. Akademika Lavrent'eva 13, Novosibirsk, 630090 Russia

e-mail: chaplik@isp.nsc.ru

Received February 22, 2002

Abstract—The energies of neutral and charged excitons in quantum rings and the plasmon frequencies in nanotubes are analyzed as functions of a magnetic field. © *2002 MAIK "Nauka/Interperiodica".*

PACS numbers: 71.35.Ji; 73.20.Mf

The magnetointerference effect (Aharonov and Bohm, 1959) is observed in systems where charged particles move in a multiply connected region. As applied to solids, these may be quantum rings or hollow cylinders (in particular, nanotubes). Oscillation effects in the magnetization [1] and conductivity [2] of hollow cylinders are well known. In the former case, the ballistic regime of electron motion was considered, and in the latter case the regime was diffusional. For this reason, the oscillation periods in these cases differ by a factor of 2; the cooperon contribution dominates the conductivity of a dirty sample, and the carrier effective charge is $2e$, while the period of conductance oscillations in a magnetic flux is equal to $hc/2e$.

In both cases, we are dealing with the macroscopic manifestations of the properties of elementary charge-carrying excitations, i.e., electrons. However, the Aharonov–Bohm effect can also occur for neutral excitations such as excitons or collective excitations of electron plasma and for composite charged particles (trions), where the effect is characterized by the nonuniversal oscillation period. This review is devoted to the nonstandard variants of the Aharonov–Bohm effect.

1. Exciton in a one-dimensional quantum ring [3]. The Hamiltonian of the system is

$$\hat{H} = \frac{\hbar^2}{2m_nR^2}\left(-i\frac{\partial}{\partial\varphi_n}+\lambda\right)^2 + \frac{\hbar^2}{2m_pR^2}\left(-i\frac{\partial}{\partial\varphi_p}-\lambda\right)^2 - \frac{e^2}{2\varepsilon R}\left|\sin\frac{\varphi_n-\varphi_p}{2}\right|^{-1}, \quad (1)$$

where $\lambda = \Phi/\Phi_0$; Φ is the magnetic flux through the ring; Φ_0 is the magnetic-flux quantum; m_n and m_p are the effective masses of an electron and a hole, respectively; ε is the dielectric constant; and R is the ring radius.

To separate the internal motion of an exciton from its gyration as a whole in the ring, we introduce new variables

$$\varphi_c = \frac{m_n\varphi_n + m_p\varphi_p}{M}, \quad \theta = \varphi_n - \varphi_p, \quad M \equiv m_n + m_p. \quad (2)$$

The Hamiltonian (1) then takes the form

$$\hat{H} = -B\frac{\partial^2}{\partial\varphi_c^2} + \beta\left(i\frac{\partial}{\partial\theta}-\lambda\right)^2 + U_c(\theta), \quad (3)$$

where $B = \hbar^2/2MR^2$, $\beta = \hbar^2/2\mu R^2$, $\mu = m_nm_p/M$, and $U_c(\theta)$ is the Coulomb energy [last term in Eq. (1)]. The total wave function can be written as $\Psi = \exp(iJ\varphi_c + i\lambda\theta)\chi(\theta)$, where J is a certain real number and $\chi(\theta)$ satisfies the one-dimensional Schrödinger equation

$$-\beta\frac{\partial^2\chi}{\partial\theta^2} + U_c(\theta)\chi = (E - BJ^2)\chi \equiv \omega\chi. \quad (4)$$

Here, E is the total energy of an exciton and ω is its internal energy. To determine J and admissible solutions of Eq. (4), it is necessary to require that the total wave function be periodic with a period of 2π independently for φ_n and φ_p. At the same time, Eq. (4) formally has the Bloch-type solutions

$$\chi = e^{ip\theta}v(\theta); \quad -\frac{1}{2} < p \le \frac{1}{2}, \quad (5)$$

where v is a periodic function of θ with the same period 2π, because it is the period of the potential $U_c \sim |\sin\theta/2|^{-1}$. By adding 2π independently to φ_n and φ_p, one arrives at the relationships

$$J\frac{m_n}{M} + \lambda + p = N_n, \quad J\frac{m_p}{M} - \lambda - p = N_p, \quad (6)$$

where N_n and N_p are arbitrary integers. It follows from Eqs. (6) that $J = N_n + N_p$. Therefore, J is an integer as it must be for the rotational quantum number of an exciton as a whole.

As to the eigenvalues ω of Eq. (4), they, evidently, must be periodic functions of quasimomentum p: $\omega(p + 1) = \omega(p)$. Since p is related to λ by Eqs. (6), one arrives at the conclusion that the exciton binding energy in a one-dimensional ring should be a periodic function of flux with a period of Φ_0. Physically, this dependence occurs because an electron and a hole can tunnel toward one another along the ring, i.e., under the Coulomb barrier. In this trajectory, the wave function of relative motion in the exciton acquires the phase equal to $2\pi \times$ the number Φ/Φ_0 of flux quanta passed through the ring, leading to the oscillations of $\omega(\Phi)$. If the effective Bohr radius a is much less than the circle length $2\pi R$, one can use the tight binding approximation for solving Eq. (4). The result for the binding energy has the form

$$\begin{aligned}\omega_n &= E_n - \Delta_n \cos 2\pi\left(\frac{\Phi}{\Phi_0} + J\frac{m_n}{M}\right)\\ &= E_n - \Delta_n \cos 2\pi\left(\frac{\Phi}{\Phi_0} - J\frac{m_p}{M}\right), \quad \Delta_n > 0,\end{aligned} \tag{7}$$

where E_n is the nth energy level of a one-dimensional exciton and Δ_n is the tunneling amplitude on the order of $R_y^* \exp(-2\pi R/a^*)$, where R_y^* is the effective Rydberg energy.

The same tight binding approximation can be used to find the probability $\Im$ of forming an exciton as a function of the flux. Since the probability $\Im$ is determined as the integral of a wave function with coinciding arguments $\varphi_n = \varphi_p = \varphi$ with respect to φ, $\Im$ is nonzero only for $J = 0$:

$$\begin{aligned}\Im &\sim |\nu(0)|^2 \delta_{0J},\\ |\nu(0)|^2 &= \frac{1-\delta^2}{1 - 2\delta\cos 2\pi\lambda + \delta^2}; \quad \delta \equiv e^{-2\pi R/a^*}.\end{aligned} \tag{8}$$

Thus, the intensity of the exciton line also oscillates with a period of Φ_0 with changing magnetic flux. The relative depth of intensity modulation is

$$\frac{\Im_{\max}}{\Im_{\min}} = \left(\frac{1+\delta}{1-\delta}\right)^2. \tag{9}$$

2. Rings with a finite width [4]. To take into account the radial degree of freedom for particles in the finite-width ring, we use the parabolic model for the lateral potential

$$V_i(P) = \frac{m_i \Omega_i^2 (\rho_i - R)^2}{2}, \quad i = n, p. \tag{10}$$

For the existing quantum rings [5], the amplitude of radial motion is much smaller than the amplitude of azimuthal motion, for which the respective size is $2\pi R$. In this sense, the ring can be considered narrow and one can assume that the condition $\hbar\Omega_i \gg W_i$ is met, where $W_i = \hbar^2/2m_i R^2$. In this case, the problem can be solved in the adiabatic approximation known from the theory of molecules: the rotational levels are found first for fixed nuclei (in the case under consideration, for fixed radial coordinates ρ_n and ρ_p of an electron and hole), and, then, small nuclear oscillations are taken into account.

To avoid cumbersome calculations, we restrict ourselves to the case $J = 0$ (only this exciton is created in the optical transition). The magnetic-field-dependent part of the Hamiltonian has the form

$$\begin{aligned}\hat{H} = -(\tilde{W}_n + \tilde{W}_p)\left[\frac{\partial}{\partial\theta} + i\frac{\tilde{W}_n\tilde{\Phi}_n + \tilde{W}_p\tilde{\Phi}_p}{\tilde{W}_n + \tilde{W}_p}\right]^2\\ + \frac{\tilde{W}_n\tilde{W}_p(\tilde{\Phi}_n - \tilde{\Phi}_p)^2}{\tilde{W}_n + \tilde{W}_p},\end{aligned} \tag{11}$$

where $\tilde{\Phi}_n = \pi H\rho_n^2/\Phi_0$, $\tilde{W}_n = \hbar^2/2m_n\rho_n^2$, and similarly for $\tilde{\Phi}_p$ and $\tilde{W}_p$, and H is the magnetic field. After the phase transformation of the wave function

$$\Psi = \chi e^{-i\lambda\theta}, \quad \lambda(\rho_n, \rho_p) = \frac{\tilde{W}_n\tilde{\Phi}_n + \tilde{W}_p\tilde{\Phi}_p}{\tilde{W}_n + \tilde{W}_p}, \tag{12}$$

the second term in the square brackets in Eq. (11) can be removed. As a result, one arrives at the Schrödinger equation for the internal motion in the adiabatic approximation, i.e., for fixed ρ_n and ρ_p. This equation gives spectrum (7) with Δ and λ parametrically dependent on the radial coordinates. By averaging this expression over the vibrational functions of the radial motion, we obtain the damping of the Aharonov–Bohm oscillations of the exciton binding energy:

$$\omega_n = E_n - \bar{\Delta}_n \exp\left(-\frac{H^2}{H_0^2}\right)\cos 2\pi\Phi/\Phi_0, \tag{13}$$

where

$$\frac{1}{H_0^2} = \left(\frac{2\pi^2 R}{M\Phi_0}\right)^2 \hbar\left(\frac{m_p^2}{m_n\Omega_n} + \frac{m_n^2}{m_p\Omega_p}\right) \tag{14}$$

for the ground vibrational state, and $\bar{\Delta}_n$ is the tunneling amplitude averaging over the radial vibrations. Thus, oscillations in the case under consideration are damped following the Gaussian law, and the damping factor $1/H_0$ increases linearly with the ring radius.

3. Magnetoexcitons with a spatially separated electron and hole in quantum rings [5]. It was implied above that the mean radii of electron and hole orbits in a ring exciton coincide with each other. A new

magnetointerference effect arises if this condition is violated. In principle, the positions of the minima of radial potential in the ring are expected to be different for an electron and hole ($R_n \neq R_p$), because this potential includes a contribution from built-in charges, states at the interface, etc. The simplest example is provided by a charged impurity at the center of the ring. The asymmetry between the electron and hole gives rise to the radial dipole moment of the exciton and qualitatively modifies the exciton energy spectrum. The simplest system of this type consists of an electron and a hole localized at the concentric circles of radii R_n and R_p, respectively. Introducing the variables

$$\varphi_0 = \frac{a\varphi_n + b\varphi_p}{a+b}, \quad \varphi_n - \varphi_p = \theta,$$

where $a = m_n R_n^2$ and $b = m_p R_p^2$, one can again separate the internal motion of the exciton from its gyration as a whole. However, the Hamiltonian of the "center of mass" of the system depends in this case on the magnetic field:

$$\hat{H}_0 = B_0\left[-i\frac{\partial}{\partial\varphi_0} + \frac{\Delta\Phi}{\Phi_0}\right]^2, \qquad (15)$$

where $B_0 = \hbar^2/2M_0R_0^2$, $R_0 = (R_n + R_p)/2$, $M_0 = (m_nR_n^2 + m_pR_p^2)/R_0^2$, and $\Delta\Phi = \pi(R_n^2 - R_p^2)H$. The eigenvalues of $\hat{H}_0$ are the energies of exciton gyration as a whole:

$$E_0(J) = B_0\left(J + \frac{\Delta\Phi}{\Phi_0}\right)^2, \quad J = 0, \pm1, \pm2\ldots. \qquad (16)$$

This should be complemented by the energy ω of relative motion of the electron and the hole. For $R_n, R_p \gg a^*$, this energy can again be determined in the tight binding approximation. However, the main part of the magnetic-field dependence of the exciton total energy in this case (where the difference $R_n - R_p$ is not too small) can be determined by Eq. (16), which is free of the exponential smallness associated with the tunneling amplitude Δ_n [cf. Eq. (7)].

Formula (16) demonstrates that, with increasing magnetic flux $\Delta\Phi$, the role of the exciton ground state sequentially transfers from the $J = 0$ state to the states $J = -1, -2$, etc. According to the selection rule for the optical transitions between the conduction and valence bands, only the $J = 0$ exciton can emit a photon. At low temperatures, excitons first relax to their ground state and only then recombine. As the magnetic field increases, the exciton ground state acquires nonzero orbital angular momentum and, therefore, the radiative recombination becomes impossible. Thus, the above theory predicts the quenching of exciton luminescence by a magnetic field. For a ring with parameters $R_0 = 300$ Å, $|R_n - R_p| = 30$ Å, the corresponding magnetic field is approximately equal to 3 T.

4. Trions in a quantum ring [4]. The formation of a structure in which an ensemble of quantum rings was controllably populated by electrons using a field electrode was reported by Warburton *et al.* [6]. They observed the recombination radiation of systems from a neutral exciton X_0 to a fivefold negatively charged complex X^{5-}. The behavior of so-called trion $X^-(e-e-h)$ is of particular interest, because this system has a bound state both in the two-dimensional and (the more so!) one-dimensional cases: the X^- state is energetically more preferable than the separated exciton and electron.

In order to analyze the behavior of a ring trion in a magnetic field, we again introduce the variables separating the internal motion and the gyration of the system as a whole:

$$\varphi_c = \frac{m_n(\varphi_1 + \varphi_2) + m_p\varphi_p}{M_{\rm tr}},$$
$$\alpha = \frac{\varphi_1 + \varphi_2}{2} - \varphi_p, \quad \beta = \varphi_1 - \varphi_2, \qquad (17)$$

where $\varphi_{1,2}$ are the electron angular coordinates and $M_{\rm tr} = 2m_n + m_p$ is the trion total mass. The internal motion is described by the following Schrödinger equation for a particle in a two-dimensional periodic potential:

$$-\left(\frac{1}{2}W_n + W_p\right)\frac{\partial^2\chi}{\partial\alpha^2} - 2W_n\frac{\partial^2\chi}{\partial\beta^2}$$
$$+\left[U(\beta) - U\left(\alpha + \frac{\beta}{2}\right) - U\left(\alpha - \frac{\beta}{2}\right)\right]\chi = \omega\chi; \qquad (18)$$
$$U(\gamma) = \left(\frac{e^2}{2R\varepsilon}\right)|\sin\gamma/2|^{-1},$$

and ω is the trion binding energy. The trion wave function $\Psi(\varphi_c, \alpha, \beta)$ is related to the solution $\chi(\alpha, \beta)$ of Eq. (18) as

$$\Psi = \chi\exp(iJ\varphi_c + \Lambda\alpha),$$
$$\Lambda \equiv \frac{2(W_n + W_p)}{W_n + 2W_p}\frac{\Phi}{\Phi_0}. \qquad (19)$$

Imposing the conditions of periodicity in φ_1, φ_2, and φ_p on Ψ, we determine the allowed values of J and the two components p and q of quasimomentum on which the energy ω depends: J is an integer, q is a half-integer, and $p = (Jm_n/M_{\rm tr} - \Lambda)$ is an integer. The trion binding energy is periodic in the reciprocal lattice corresponding to the potential energy in Eq. (18) and, therefore,

depends periodically on Φ. In the strong-coupling approximation, one obtains

$$\omega = E_0 - 2\Delta(2\pi)\cos 2\pi\left(\frac{2m_n}{M_{\rm tr}}J + \Lambda\right) - 4\Delta(\sqrt{5}\pi)\cos\pi\left(\frac{2m_n}{M_{\rm tr}}J + \Lambda\right). \quad (20)$$

The arguments 2π and $\sqrt{5}$ of tunneling amplitudes are the distances from the initial site to the nearest neighbors in the lattice defined by the potential in Eq. (18), and E_0 is the 1D trion binding energy in a rectilinear quantum wire (i.e., the $R \longrightarrow \infty$ limit).

The essential feature of a trion is that the oscillation period of its internal energy depends on the ratio of effective masses:

$$\Delta\Phi = \Phi_0\frac{2m_n + m_p}{2(m_n + m_p)}. \quad (21)$$

As far as I know, to date this is the only example of a nonuniversal period of Aharonov–Bohm oscillations (i.e., the period that does not correspond to the charges e or $2e$, etc.). This result is qualitatively explained as follows. The magnetic-flux dependence of binding energy is determined by the phase acquired by the wave function upon tunneling of the particles along the ring. Let a trion first be at the point $\varphi = 0$ and at a certain point φ_0 after tunneling. To set out the phase incursion contributing to the internal energy, one should require that the condition $\varphi_c = \text{const}$ be met when particles pass from $\varphi = 0$ to $\varphi = \varphi_0$. The trion can tunnel in two ways: (i) $\Delta\varphi_1 = \varphi_0$, $\Delta\varphi_2 = \Delta\varphi_p - (2\pi - \varphi_0)$ and (ii) $\Delta\varphi_1 = \Delta\varphi_2 = \varphi_0$, $\Delta\varphi_p = -(2\pi - \varphi_0)$. The changes in phase $\delta\psi$ in the first and second cases are $\delta\psi_1 = (e/hc)AR \times 2\pi(m_n + m_p)/M_{\rm tr}$, where A is the vector potential on the ring, and $\delta\psi_2 = 2\delta\psi_1$, respectively. The two indicated possibilities of tunnel transition correspond to two harmonics in Eq. (20), and the period (21) follows from the above expression for $\delta\psi_2$. Clearly, only one contribution leading to Eq. (7) exists for a neutral exciton. The total trion energy depends on the magnetic flux also through the gyration contribution:

$$E_{\rm tr} = W_{\rm tr}(J - \lambda)^2 + \omega, \quad W_{\rm tr} = \frac{\hbar^2}{2M_{\rm tr}R^2}. \quad (22)$$

The shift $\Delta\nu$ of the exciton luminescence line is an observable quantity. To the leading order in $W_n/\hbar\Omega_n$, it is determined for a trion as

$$\Delta\nu = (W_{\rm tr} - W_n)\left(\frac{\Phi}{\Phi_0}\right)^2, \quad J = 0. \quad (23)$$

Since $M_{\rm tr} > m_n$, the resulting diamagnetic (i.e., spin-independent) shift is negative.

5. Plasma oscillations in nanotubes (Aharonov–Bohm effect for plasmons) [7]. Below, we consider the collective oscillations of 2D electrons at the surface of a hollow cylinder in a magnetic field parallel to its axis. The plasma modes of this system are characterized by the continuous momentum k along the cylinder axis and the discrete azimuthal quantum number $m = 0, \pm1, \pm2\ldots$. Ignoring the delay effects, one easily obtains the dispersion relation for plasmons in a nanotube in the absence of a magnetic field:

$$\omega_m^2(k) = \frac{2e^2N_L}{\mu}\left(k^2 + \frac{m^2}{a^2}\right)K_m(ka)I_m(ka). \quad (24)$$

where a is the nanotube radius, μ is the effective electron mass, N_L is the linear electron density, and I_m and K_m are the Bessel function of imaginary argument and the Mcdonald function, respectively. Formula (24) is based on the Drude expression for conductivity, which disregards spatial dispersion. A magnetic field can affect the dispersion relation for plasma oscillations only through a material equations (relationship between current and field). For this reason, under the assumption that the conductivity is classical, the longitudinal magnetic field cannot change the motion of 2D electrons at the cylinder surface, so that the conductivity [as well as the dispersion law $\omega_m(k)$] is independent of the field. The influence of the magnetic field (more precisely, of the magnetic flux Φ) arises only if the quantum effects are taken into account.

One has to calculate the polarization operator $\Pi(k, m)$ for nanotube electrons whose single-particle spectrum has the form

$$E_m(k) = \frac{(\hbar k)^2}{2\mu} + B\left(m + \frac{\Phi}{\Phi_0}\right)^2, \quad B = \frac{\hbar^2}{2\mu a^2}. \quad (25)$$

Then, by solving the Poisson equation with an induced charge density proportional to $\Pi(k, m)$, one can obtain the dispersion relation. For an azimuthally symmetric plasmon ($m = 0$), it has the form

$$1 = \frac{2e^2k^2}{\pi\hbar}K_0(ka)I_0(ka)\sum_m\frac{V_{\rm F}(m)}{\omega^2 - k^2V_{\rm F}^2(m)}, \quad (26)$$

where, $V_{\rm F}(m) = \sqrt{2/\mu[E_{\rm F} - B(m + \Phi/\Phi_0)^2}$ and the Fermi energy $E_{\rm F}(m)$ is found from the equation

$$\hbar N_L = \frac{2\sqrt{2\mu}}{\pi}\sum_m\sqrt{E_{\rm F} - B\left(m + \frac{\Phi}{\Phi_0}\right)^2}. \quad (27)$$

Summation over m is limited by the requirement that radicands be positive. An analytic (and a comparatively simple) answer can be obtained in the approximation of weak spatial dispersion, i.e., $\omega \gg kV_{\rm F}(m)$ for all admis-

sible m values. Expanding Eq. (26) in the parameter kV_F/ω and applying the Poisson summation formula, one obtains

$$\omega^2 \approx \frac{2e^2k^2N_L}{\mu}K_0(ka)I_0(ka) + \frac{3(k\bar{V}_F)^2}{2\pi^2N_La}\sum_{l=-\infty}^{+\infty} J_2\left(2\pi l\sqrt{\frac{\bar{E}_F}{B}}\right)\frac{\cos 2\pi l\Phi/\Phi_0}{l^2}. \quad (28)$$

Here, $\bar{E}_F = \mu\bar{V}_F^2/2 = \hbar^2N_L/a\mu$ is the oscillation-averaged Fermi level. Thus, the plasmon frequency oscillates with magnetic flux with a period $\Delta\Phi = \Phi_0$. Azimuthally nonuniform oscillations with $m \neq 0$ are similar to the intersubband 2D plasmons in quantum films. In essence, these oscillations are the transitions between subbands, $m' \longrightarrow m + m'$, with allowance for Coulomb effects (depolarization shift). The corresponding operator $\Pi(k, m)$ is periodic in Φ with the period Φ_0. The same is true for the frequency of intersubband plasmon. Thus, the Aharonov–Bohm effect occurs for neutral excitations corresponding to the collective degrees of freedom of a system.

Most results reported in this review were obtained in the works supported by the Russian Foundation for Basic Research, project no. 99-02-17127.

REFERENCES

1. I. O. Kulik, Pis'ma Zh. Éksp. Teor. Fiz. **11**, 407 (1970) [JETP Lett. **11**, 275 (1970)].
2. B. L. Al'tshuler, A. G. Aronov, and B. Z. Spivak, Pis'ma Zh. Éksp. Teor. Fiz. **33**, 101 (1981) [JETP Lett. **33**, 94 (1981)]; D. Yu. Sharvin and Yu. V. Sharvin, Pis'ma Zh. Éksp. Teor. Fiz. **34**, 288 (1981) [JETP Lett. **34**, 272 (1981)].
3. A. V. Chaplik, Pis'ma Zh. Éksp. Teor. Fiz. **62**, 885 (1995) [JETP Lett. **62**, 900 (1995)]; R. A. Römer and M. E. Raikh, Phys. Rev. B **62**, 7045 (2000).
4. A. V. Chaplik, Zh. Éksp. Teor. Fiz. **119**, 193 (2001) [JETP **92**, 169 (2001)].
5. S. E. Ulloa, A. O. Govorov, A. V. Kalameitsev, *et al.*, in *Proceedings of the 14th International Conference EP2DS, Prague, 2001*, p. 1037.
6. R. J. Warburton *et al.*, Nature **405**, 926 (2000).
7. A. I. Vedernikov, A. O. Govorov, and A. V. Chaplik, Zh. Éksp. Teor. Fiz. **120**, 979 (2001) [JETP **93**, 853 (2001)].

Translated by R. Tyapaev